Inaugural dissertation

for obtaining the doctoral degree of the

Combined Faculty of Mathematics, Engineering and Natural Sciences of the

Ruprecht – Karls – University

Heidelberg

Presented by

M. Sc. Vladyslav Bondarenko

Born in Makariv, Ukraine

Oral examination: 12th of August 2022

Coordination Mechanisms of Mammalian Embryo Implantation

Referees: Prof.-Jun. Dr. Steffen Lemke

Prof. Dr. Detlev Arendt

To my fellow scientists from IMBG and BIPH in Kyiv, Ukraine

ABSTRACT

A direct interaction between the extraembryonic and the uterine tissues during embryo implantation generates a unique biomechanical context for the blastocyst. However, our mechanistic understanding of the regulation of blastocyst morphogenesis during implantation is limited by the inaccessibility *in vivo* and remaining challenges to model feto-maternal interaction *ex vivo*. To overcome these limitations, I applied microfabrication and biomaterial engineering to model biomechanical cues of the murine intrauterine environment *ex vivo* with high precision and tunability. I identify that embryo-uterine adhesion and tissue geometry are critical for successful peri-implantation development. In a specific parameter range, closely resembling *in utero* conditions, the 3D geometrically patterned hydrogel supports mouse blastocysts through implantation and enables robust peri-implantation morphogenesis; promotes the development of the Reichert's membrane and all extraembryonic tissues, including giant trophoblast, which directly interacts with the uterus.

To monitor *in toto* peri-implantation embryo dynamics, the culture method was integrated with inverted view InVi-SPIM and multiview MuVi-SPIM light-sheet microscopes. I show that integrin-mediated adhesion by the mural trophectoderm provides the mechanism of trophectoderm tension release, driving the morphogenesis of the extraembryonic ectoderm and egg cylinder patterning. Moreover, the embryo-uterine adhesion enables collective trophoblast migration, dependent on Rac1. Finally, I demonstrate that the uterine tissue geometry spatially coordinates collective trophoblast migration to delineate space for egg cylinder growth. Together, this study reveals essential mechanisms of dynamic embryo-uterus interactions during peri-implantation development.

ZUZAMMENFASSUNG

Eine direkte Wechselwirkung zwischen dem extraembryonalen und dem Uterusgewebe während der Embryoimplantation erzeugt einen einzigartigen biomechanischen Kontext für die Blastozyste. Unser mechanistisches Verständnis der Regulierung der Blastozysten-Morphogenese während der Implantation ist jedoch durch die Unzugänglichkeit *in vivo* sowie durch die verbleibenden Herausforderungen bei der *ex vivo* Modellierung der feto-maternalen Interaktion begrenzt. Um diese Einschränkungen zu überwinden, habe ich Mikrofabrikation und Biomaterialtechnik verwendet, um biomechanische Signale der intra-uterinen Umgebung der Maus *ex vivo* mit beispielloser Präzision und Einstellbarkeit zu modellieren. Ich zeige, dass die Embryo-Uterus-Adhäsion und die Gewebegeometrie entscheidend für eine erfolgreiche Periimplantationsentwicklung sind. In einem bestimmten Parameterbereich, der den Uterusbedingungen sehr ähnlich ist, unterstützt das geometrisch geformte 3D-Hydrogel Maus-Blastozysten bei der Implantation und ermöglicht eine robuste Periimplantationsmorphogenese. Weiter erlaubt das geformte Gel die Entwicklung der Reichert-Membran sowie aller extraembryonalen Gewebe, einschließlich der Trophoblast-Riesenzellen, die direkt mit der Gebärmutter interagieren.

Um die Dynamik des Embryos während der gesamten Periimplantation zu studieren, haben wir außerdem die Kultivierungsmethode für Lichtblattmikroskope mit invertierter Ansicht (InVi-SPIM) und mit mehreren Ansichten (MuVi-SPIM) angepasst, als auch in diesen realisiert. Ich zeige, dass die Integrin-vermittelte Adhäsion des muralen Trophektoderms den Mechanismus zur Entspannung des Trophektoderms bildet, der die Morphogenese des extraembryonalen Ektoderms vorantreibt. Darüber hinaus ermöglicht die Embryo-Uterus-Adhäsion eine kollektive Trophoblastenmigration, die von Rac1 abhängig ist. Abschließend zeige ich, dass die Geometrie des Uterusgewebes die kollektive Trophoblastenmigration räumlich koordiniert, um Raum für das Wachstum des Eizylinders abzugrenzen. Zusammenfassend zeigt diese Studie Mechanismen auf, durch welche die dynamischen Interaktionen zwischen Embryo und Uterus eine wesentliche Rolle bei der periimplantären Entwicklung spielen.

TABLE OF CONTENTS

ABBREVIATIONS

2D – 2-Dimentional

3D – 3-Dimentional

3E-uterus – Ex vivo Engineered uterine Environment with 3D geometrically patterned hydrogels

A-P – Anterior-Posterior

a.u. – arbitrary units

AVE – Anterior Visceral Endoderm

BAC – Bacterial Artificial Chromosome

BMP – Bone Morphogenetic Protein

bp – base pairs

BSA – Bovine Serum Albumin

CAG – promoter consisting of cytomegalovirus (CMV) enhancer, chicken beta-actin gene and rabbit beta-globin gene fragments

Cas9 – CRISPR associated protein 9

cDNA – complementary DNA

CDX2 – Caudal type homeobox 2

CRISPR – Clustered Regulatory Interspaced Short Palindromic Repeat

D-V – Dorsal-Ventral

d.p.c – day post conception

DAPI – 4,6-diamidino-2-phenylindole

ddPCR – droplet digital PCR

DMEM – Dulbecco's Modified Eagle's Mediun

DMSO – Dimethyl Sulfoxide

DNA – Deoxyribonucleic Acid

DPBS – Dulbecco's Phosphate Buffered Saline

DVE – Distal Visceral Endoderm

ECM – Extracellular Matrix

EDTA – Ethylenediaminetetraacetic Acid

EGF – Epidermal Growth Factor

EGFP – Enhanced Green Fluorescent Protein

EPI – Epiblast

ESC – Embryonic Stem Cell

ExE – Extraembryonic Ectoderm

FGF4 – Fibroblast Growth Factor 4

FP – Fluorescent Protein

GATA4 – GATA binding protein 4

GATA6 – GATA binding protein 6

gDNA – genomic DNA

GT – Giant Trophoblast

H2B – Histone 2B

hCG – human Chorionic Gonadotropin

HEPES – 4-(2-hydroxyethyl)-1-piperazineethanesulfonic acid

ICM – Inner Cell Mass

IGFBP-1 – Insulin-like Growth Factor-Binding Protein 1

IHH – Indian Hedgehog protein

IVC – In Vitro Culture

KSOM – Potassium Simplex Optimization Medium

KSOM-H – KSOM with HEPES

KSOMaa – Potassium Simplex Optimization Medium with Amino Acids

KSR – Knock-out Serum Replacement

L-R – Left-Right

LDTM - Low-Defect Thiol-Michael Addition

LIF – Leukemia Inhibitor Factor

M – Molar

MEF – Mouse Embryonic Fibroblast

mRNA – messenger RNA

mTE – mural TE

mz – maternal zygotic

OCT4 – Octamer-binding transcription factor 4

PBS – Phosphate Buffered Saline

PCR – Polymerase Chain Reaction

PDMS – Polydimethylsiloxane

PEG – Poly(ethylene glycol)

pERM – phosphorylated Ezrin/Radixin/Moesin

PGK – Phosphoglycerate Kinase

PMSG – Pregnant Mare Serum Gonadotropin

PrE – Primitive Endoderm

PRL – Prolactin

pTE – polar TE

RM – Reichert's Membrane

RNA – Ribonucleic Acid

Roi – Region of interest

rpm – rounds per minute

RT – Room Temperature

s.d. – standard deviation

sgRNA – single guide RNA

SHH – Sonic Hedgehog protein

SOX2 – SRY-box containing protein 2

SPIM – Single Plane Illumination Microscopy

TAM – Tamoxifen

T7 – T7 promoter

TB – Trophoblast

TE – Trophectoderm

TF – Transcription Factor

U – Units

v/v – volume per volume

w/v– weight per volume

WT – Wild Type

YAP/TAZ – Yes-Associated Protein

ZP – Zona Pellucida

1 INTRODUCTION

1.1 Historical retrospective

Reproduction, pregnancy, and origin have always been of interest and fascination to the human mind. The medieval knowledge of female reproductive anatomy was derived mainly from the vivisection of pregnant animals, such as cows and pigs, and was believed to be similar to humans, e.g., in the *Anathomia* of Mondino de Luzzi (1270 – 1326). The first detailed drawings of the human fetus and the maternal tissues were made by Leonardo Da Vinci in his private notebook between 1510 and 1512 (Royal Collection Trust). In these drawings, the fetal positioning and the parts of the female reproductive system's vasculature were correctly depicted for the first time and with unprecedented detail. It is astonishing how his observations allowed Leonardo to conclude on the side of his notebook that "the fetus is vivified and nourished by the life and food of the mother" (Royal Collection Trust), implicating physiological feto-maternal interaction. Interestingly, his depiction of the placenta is likely also derived from another animal (probably a cow) as it resembles a cotyledonary and not a discoidal placenta in humans.

Late 19th – beginning of 20th century marks a golden age of natural history and comparative embryology. At the end of the 19th century, William Turner, in a series of comparative anatomy studies, distinguished the major placental types across the mammals and argued for both fetal and maternal origin of the placenta (Turner W., 1876). In 1889, Ambrosius Hubrecht introduced the term "trophoblast" for the tissue of fetal origin, which invades and directly interacts with the maternal environment for nutritional supply (Hubrecht AAW., 1889). Between 1889 and 1909, he expanded the comparative study with insectivores and lower primates and related the early ontogenesis of mammals to the vertebrate phylogeny (Hubrecht AAW., 1908; Pijneborg et al., 2013), which, however, is debated. In 1887, Franklin P. Mall started his collection of human embryo samples. While working at the Department of Embryology of the Carnegie Institution of Washington, he began establishing a standard staging system for human embryogenesis. Almost a hundred years of work by the successor scientists were required to establish a comprehensive atlas, known as "Carnegie Staging," which is the most detailed reference of the fetal anatomy available to date (O'Rahilly R. Müller F., 2010).

1.2 Philosophical perspective

Although addressing philosophical and ethical problems goes far beyond my thesis, long ago, they used to constitute an important incentive and precede the actual science. Here, I briefly mention some.

The phenomenon of pregnancy across the animal kingdom, including humans, leads to or is related to some interesting philosophical questions:

- What is birth?
- Is birth the act of consciousness?
- When and how does a separate physical being form?
- What does it mean to form and become an organism?
- How does the ‘multiple’ become the ‘one’ and the ‘one’ becomes the ‘multiple’?
- Why and how do we define boundaries in nature? (e.g., organism vs. environment) Do they and how do they emerge in biological systems?
- How does the communication evolve from scratch? How deterministic is it?

…

Importantly, pregnancy and birth are inherently personal and individual experiences. They might always need to be viewed as such when asking questions and seeking answers. General questions may be the wrong questions to ask, and the general answers may not exist or may never be found. This becomes puzzling and interesting from the perspective of those who cannot experience pregnancy, e.g., males and females that are unable to conceive a biological child. To what extent can the unique physiological phenomena be emulated, and should they ever be emulated? For which purpose? How will this affect their value and meaning, and would not that be more harmful than the initial purpose?

1.3 General concepts of development

Below I introduce some general intuitive concepts and terms proposed for biological systems, including development.

Organismal development is a general term encompassing multiple processes which result in emergence of an independently functional structure. The system exhibits **emergence** when a novel type of behavior is established from interaction of its components as they cannot exhibit the same behavior individually. Along with **hierarchy** and **interactivity**, **emergent behavior** is an essential property of biological systems. However, emergence is not the same as self-organization, and those processes can happen independently (De Wolf & Holvoet, 2005).

Self-organization can be defined as 'a dynamical and adaptive process where systems acquire and maintain structure themselves without external control' (De Wolf & Holvoet, 2005). 'No external control' refers to the 'absence of direction, manipulation, interference, pressures, or involvement from outside the system' (De Wolf & Holvoet, 2005). Therefore, when considering any process from the self-organization perspective, the explicit definitions of the 'inside,' 'outside,' and the input controls are essential (De Wolf & Holvoet, 2005). For a naive example, with regard to permissive but not controlling external environmental factors such as temperature, humidity, and atmospheric pressure, the development of some oviparous (egg laying) animals can be considered self-organizing. On the contrary, with regard to maternally-deposited factors, such as yolk, the self-organization of the above-mentioned system is debatable, as the maternal factors can control symmetry breaking, patterning, and morphogenesis. To resolve some confusion, self-organization can be attributed solely to the process (e.g., embryo patterning, cell fate specification) rather than the system itself.

How did the feto-maternal co-evolution lead to a mechanochemical coupling between the mother and the fetus? Can it be explained solely from a self-organization perspective? Implantation into maternal tissues challenges the universality of the self-organization properties of the mammalian embryo system and potentially restricts it to the behavior of specific tissues at a specific time in specific species. In general, understanding the relationship between self-organization and the system's boundary in viviparity will require future research and a more advanced discussion.

In relation to stimuli and the responses, self-organization is closely linked to **robustness** and **adaptability**. Robustness means the maintenance of the system's organization (trait) in response to a change or perturbation (e.g., stochastic noise, environmental change, and genetic variation) (Félix & Wagner, 2008). Different mechanisms were proposed to enable robust responses of developmental systems to perturbations, such as distributed robustness (Wagner, 2005), feedback loops in regulatory networks (Shinar & Feinberg, 2010), functional redundancy (Edelman & Gally, 2001), buffering (Whitacre & Bender, 2010), and modularity (reviewed by Kitano, 2004). Systems which are robust to some types of perturbations can be fragile to others (Edwards & Palsson, 2000; Fu et al., 2009). The stress and perturbation can also result in **adaptation** or **plasticity**, producing a different response type. Robustness and adaptability are conceptually interrelated and often co-occur.

Evolvability is an organism's capacity to generate heritable phenotypic variation (Kirschner M. & Gerhart J., 1998). In a more general sense, it can be attributed to variable systems with some sort of information transmission (e.g., dividing cells, communities, societies, etc.). Several mechanisms were proposed to deconstraint the biological systems: **weak linkage**, **exploratory behavior**, and **modularity** (Kirschner M. & Gerhart J., 1998). **Weak linkage** is very common for chains of reactions observed in signaling pathways, gene regulatory networks, and neural circuits, which means that a process's activity depends minimally on other components or processes (Kirschner M. & Gerhart J., 1998). Weak interdependence between multiple interacting components produces high tolerance and flexibility to changes, e.g., addition, removal, or modification of individual components and adjustment of interactions. It is not difficult to imagine it can also lead to robustness. **Exploratory behavior** occurs, for example, by neural crest cells migrating throughout the embryo or neurons searching for new connections. With lowered environmental constraints (requirements) for functionality, the exploratory behavior can explain the emergence of novel behaviors at little cost to the rest of the system (Kirschner M. & Gerhart J., 1998). In **modular** systems, compartments are weakly linked to other spatially or temporally distant compartments (Kirschner M. & Gerhart J., 1998). Such independence can function as a buffer against deleterious changes and, similarly, lead to more robustness and novelty.

When applied to biological systems, **symmetry-breaking** often refers to a shift in distribution of some factor or change in geometry that has implications for the

system. For example, cell motility requires breaking of uniformity in cytoskeletal network protein distributions to form front and rear, and the non-uniform spatial distribution of plasma membrane-bound proteins and organelles defines cell polarity (Mullins, 2009; Vladar et al., 2009). Similarly, spatial symmetries are present within higher-order systems, such as tissues, and embryos, and when those symmetries are broken, it can result in **patterning** (emergence of regularity) **and morphogenesis** (emergence of shape) (Rodriguez et al., 2005; Nakamura et al., 2006). Mechanistically, patterns emerge from **positional information** (Wolpert L., 1969; Driever and Nüsslein-Volhard, 1988), **reaction-diffusion processes** (Kondo & Miura 2010; Müller et al., 2012), **mechanical self-organization** (Harris et al., 1984; Palmquist et al., 2022), and **biomechanical coupling** (reviewed in Hannezo & Heisenberg, 2019; Lenne et al., 2021).

In a "French Flag Model," cells acquire a positional value which they interpret according to their distance from a boundary and a current dynamic state (Wolpert, 1969; reviewed by Kerszberg & Wolpert, 2007). The boundary produces morphogens (e.g., FGF, SHH, Wingless, BMP) – diffusible signaling molecules that can form concentration gradients and affect cell fate. The positional value can be encoded by the spatial gradient of morphogen concentrations and cell-cell interactions (Kerszberg & Wolpert, 2007). In spatial gradient models, one or more morphogens typically do not interact.

Reaction-diffusion (RD) model, introduced by A. Turing, explains how the mutual interaction of morphogens results in spontaneous pattern formation (reviewed by Kondo & Miura, 2010). According to the RD models, biological pattern formation can be explained by a combination of interacting morphogens diffused in a continuous field (Kondo & Miura, 2010). It predicts so-called "Turing patterns," nonlinear waves that are maintained by the dynamic equilibrium of the system and, depending on the interactions between molecules and their diffusion rates, can arise independently of any preexisting positional information (Kondo & Miura, 2010). Short-range positive and long-range negative feedback is frequent in the networks that form Turing patterns, e.g., in the skin patterning of fish (Nakamasu et al., 2009). RD models have helped explain the patterning of feather buds in chickens (Jung et al., 1998), hair follicles, and digits in mice (Sick et al., 2006) (see reviewed by Kondo & Miura, 2010 and Landge et al., 2020).

In the last decades, more attention has been drawn to the mechanical inputs in morphogenesis. The spatial context can determine stem-cell fate (Rompolas et al., 2013), and the spatially coordinated mechanics and cell proliferation control tissue growth and morphogenesis (Wang & Riechmann, 2007; Lecuit and le Goff, 2007). Morphogenesis can be spatially coordinated by physical interaction with the maternally-provided vitelline envelope during gastrulation movements in insects (Bailles et al., 2019; Münster et al., 2019). It has been proposed that tissue geometry can induce local curvatures that can feedback on the cellular signaling and symmetry-breaking (Shyer et al., 2015; Gjorevski; Nikolaev et al., 2022) and that the cells can 'sense' curvature by modifying the thickness of the tissue and the nuclear shape (Luciano et al., 2021).

YAP/TAZ, Wnt, Notch, and EGF signaling pathways can (either directly or indirectly) transmit extracellular mechanical inputs into a biochemical cascade of reactions and cell fate decisions (Iwasaki et al., 2000; Dupont et al., 2011; Brunet et al., 2013; Przybyla et al., 2016; Stassen et al., 2020). A specialized mechanosensitive ion channel, Piezzo, can directly sense local shear stress, confinement, and stiffness and crosstalk with the signaling pathways to initiate mechanotransduction via the influx of extracellular Ca2+ (Wu et al., 2017). The feedback mechanisms between mechanical and biochemical signals are reviewed in Hannezo & Heisenberg, 2019; Lenne et al., 2021.

When thinking of the two-component mammalian feto-maternal system, it is interesting to ask *how the intimate mechanochemical coupling between the two genetically distant organisms is established during pregnancy? Which constraints (e.g., mechanical or genetic) originate first and shape the system's behavior? How do these constraints act at different levels of the organization? How plastic are they? Which mechanisms provide evolvability and robustness of such systems?* To address those questions, it is essential to develop or apply quantitative theories and concepts that could combine evolutionary and biomechanical variables and be testable in experimental settings with genetic and environmental engineering.

1.4 Viviparity: an engine of evolutionary innovations

In **viviparity** or a live-bearing reproduction, females retain developing eggs inside their reproductive tracts and give birth to their fully developed juveniles or pre-metamorphic larvae (reviewed by D. Blackburn, 2015). Viviparity evolved independently multiple times across multiple vertebrate lineages: at least 115 times among reptiles, 13 in bony fishes, 8 in cartilaginous fishes, 8 in amphibians, and in mammals (D. Blackburn, 2015). The oldest fossil records of amniotic embryos suggest that aquatic mesosaurs and plesiosaurs were also viviparous (O'Keefe & Chiappe, 2011; Pineiro et al., 2012). By comparison, other vertebrate innovations have arisen only once or a few times, such as lactation, the amniote egg, full endothermy, and powered flight (D. Blackburn, 2015). Interestingly, in lizards viviparous and oviparous populations can be found within the same species, indicating a possibility of intraspecific bimodality in reproductive modes (Fairbairn et al., 1998).

Generally speaking, patterns of maternal-fetal nutrient exchange, such as nutritional modes and their degrees, are substantially variable for all taxonomic levels. Maternal nutritional supply (matrotrophy) evolved at a different time in relation to viviparity, indicating that historical trajectories and selective pressures through which matrotrophy and viviparity have evolved vary broadly (D. Blackburn, 2015). It remains to be determined whether the over-arching evolutionary explanations (e.g., selective advantage and environmental pressure) apply broadly across viviparous vertebrate taxa (D. Blackburn, 2015).

The common patterns of viviparity include modification of the embryonic respiratory structures and the maternal reproductive tract. The pre-existing embryonic respiratory structures have been recruited and modified during evolution for nutrient uptake in at least 21 of the 33 matrotrophic vertebrate lineages (63.6%) (D. Blackburn, 2015). In 90% of the 146 extant origins of viviparity, embryos develop within the oviduct or its uterine derivative (D. Blackburn, 2015). The frequent re-usage of the maternal oviduct or uterus by viviparous mammals indicates that some intrinsic constraints on design or pre-adaptations can be compartmentalized to these organs.

1.5 Placentation in mammals

The placenta is formed by an intimate apposition or fusion of the fetal organs to the maternal (or paternal) tissues for physiological exchange (Mossman, 1937). Placentation arose in the ancestral therian mammal approximately 130 million years ago and is one of the youngest and the most variable structures in mammals (reviewed by Griffith & Wagner, 2017). Even between closely related species, significant differences in placental patterning can be seen (Griffith & Wagner, 2017). Below, I describe three classifications of placental types based on the composition of interacting tissues, shape, and degree of invasiveness.

Choriovitelline placenta is formed by a vascularized trilaminar yolk sac, apposed to the uterine tissue (reviewed by Furukawa et al., 2014). The chorioallantoic placenta is formed from the endometrium and the trophectoderm of the embryo and is the principal placenta in mammals during the middle to late gestation (Furukawa et al., 2014).

Based on gross shape, there are four types of chorioallantoic placenta: diffuse, multicotyledonary, zonary, and discoid (Figure 1.1). The discoid placenta of primates, rodents, and lagomorphs (rabbit) is characterized by a single or double-disc, and embryo-uterine interaction is confined to a roughly circular area (Furukawa et al., 2014). The zonary placenta of carnivores shows an intimate interdigitating contact zone that forms a belt around the chorionic sac (Furukawa et al., 2014). Multicotyledonary placenta is found in ruminants (cattle, sheep) and is characterized by many spot-like placental regions of the endometrium known as caruncles whereas the intervening areas of the chorion are relatively avascular (Furukawa et al., 2014). Diffuse placenta of horses and pigs forms around the entire surface of the uterine luminal epithelium with folds and villi (Furukawa et al., 2014).

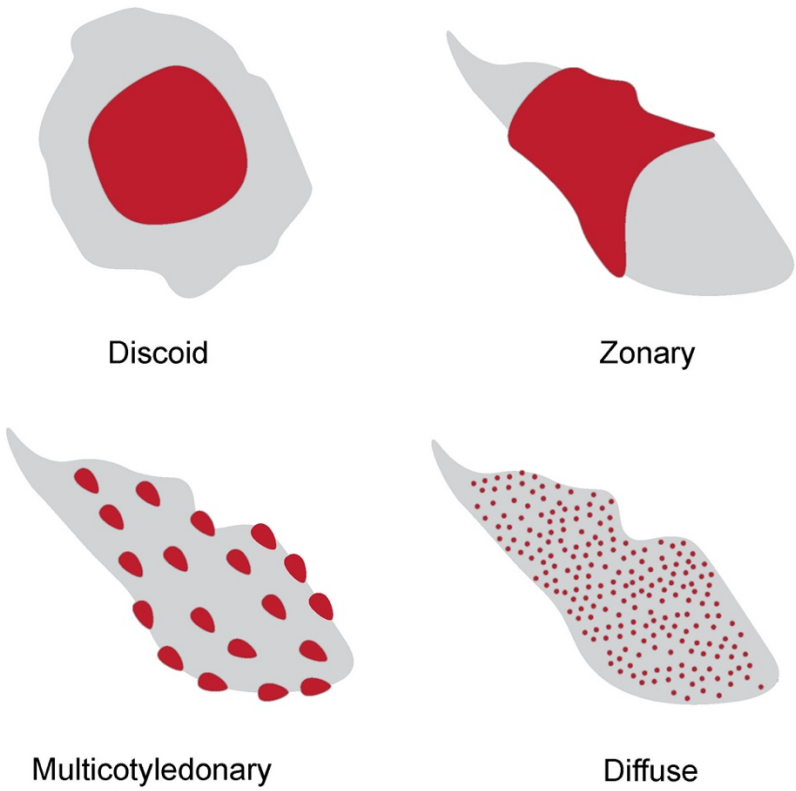

Figure 1.1 Schematic of the placental types by shape. Red, placenta; grey, uterus.

Based on the histological structure and the degree of invasion, three main types of the chorioallantoic eutherian placenta can be distinguished: epitheliochorial, endotheliochorial, and haemochorial. The epitheliochorial placenta of horses, pigs, and ruminants is the most superficial placenta without significant invasion of the uterine lining and destruction of the maternal tissues (Furukawa et al., 2014). In the endotheliochorial placental type of carnivores, the maternal uterine epithelium and the connective tissue disappear after implantation, and the trophoblast comes into direct contact with the maternal endometrium (Furukawa et al., 2014). The haemochorial placenta of humans, rabbits, rats, and mice is the most invasive, where all maternal tissue layers disappear, leading to direct contact between the trophoblast and the maternal blood. Within haemochorial placentation, three types are distinguished based on the number of trophoblast cell layers: haemomonochorial (single layer of trophoblast in human and guinea pig), haemodichorial (two layers in rabbit), haemotrichorial (three layers in rat and mouse) (Figure 1.2).

Notably, for those placental types classified from the gross tissue morphologies, the molecular and biomechanical differences between them and the mechanisms of their formation are very poorly understood, if at all.

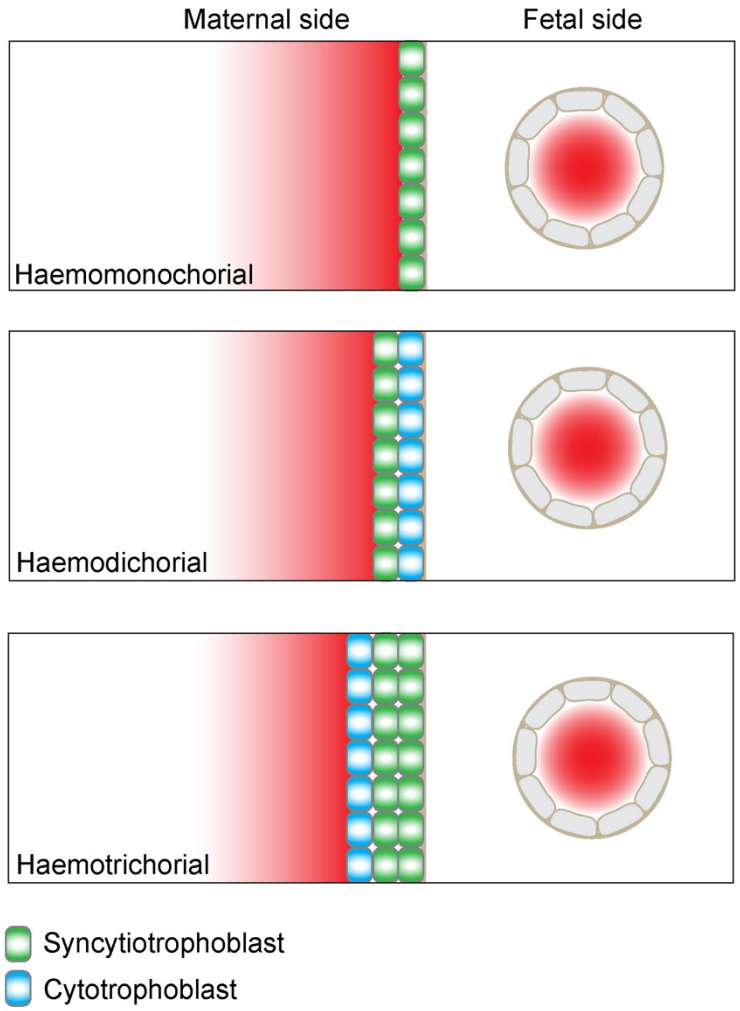

Figure 1.2 Schematic of the types of haemochorial placenta by the number of trophoblast cell layers.

The functional innovations during placental evolution could be provided by repurposing proteins already expressed in the tissue (co-option), recruiting the expression of genes normally expressed elsewhere in the organism (recruitment), and introducing novel genes to the genome of the organism, either by gene duplication, horizontal transfer, or *de novo* gene evolution (Chen et al., 2013; Griffith & Wagner, 2017). For amniotes, organs of gas, nutrient exchange, as well as endocrine organs evolved into the extraembryonic placental tissues, suggesting that the origin of a

placenta was a co-option of the already expressed genes and functions (reviewed by Griffith & Wagner, 2017). Besides, gene expression recruitment from the ancestry Müllerian canal to the uterus via transposable elements was suggested to be a major mode of functional specialization to facilitate pregnancy in therian mammals and reptiles (Lynch et al., 2015; Griffith & Wagner, 2017). Similarly, structural novelties in placental evolution have been proposed to arise from the rearrangement of existing cell types, the emergence of novel cell types (e.g., decidual stromal cells), and tissue-tissue interactions such as signaling (Griffith & Wagner, 2017).

1.6 Mammalian uterine structure

Mammalian oviduct and uterus derive from a pair of Müllerian ducts and form specialized organs to nourish embryos before birth. Estrogen and progesterone, released from the ovary, regulate biochemical changes in the oviduct, facilitating fertilization (Coy et al., 2012). Fertilization happens in the ampulla, a specialized region of the oviduct. After the egg is fertilized, it begins its journey through the rest of the oviduct toward the uterus, where its implantation and formation of the placenta occurs.

The degree of Müllerian duct fusion, complete, partial, or incomplete, is species-specific and defines three types of adult uteri based on the gross morphological characteristics: simplex, bicornuate, or duplex (reviewed by Spencer et al., 2005; Figure 1.3). Müllerian fusion is absent or limited in rodents, leading to the formation of two or ‘‘duplex’’ uteri (Spencer et al., 2005). In domestic animals, the Müllerian ducts fuse more posteriorly, which results in a long (pig) to medium-length (sheep and cow) bicornuate uterus with a short common corpus, single cervix, and vagina (Spencer et al., 2005). The Müllerian ducts of higher primates (including humans) fuse more anteriorly and form a single (‘‘simplex’’) uterus with a single cervix and vagina (Spencer et al., 2005). Anatomical variations of the female reproductive tract can even be observed within the species (Mossman, 1987; Spencer et al., 2005).

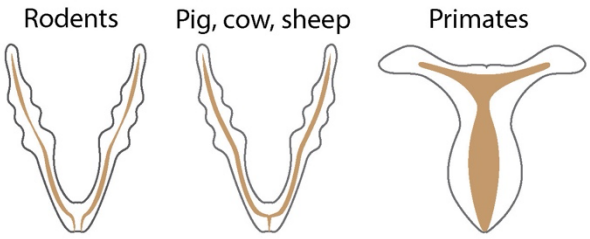

Figure 1.3 Schematic of the uteri types by the gross morphological characteristics.

Uterine tissue is comprised of a luminal epithelium, glandular epithelium, stroma, and multilayered smooth muscle tissue (Figure 1.4). The organization of glandular epithelium substantially varies among the morphological uteri types and individual species. The uterine glands of rodents do not tightly coil and branch, as is characteristic of endometria in humans and domestic cattle, and the glands are more abundant in the uteri of pigs, sheep, cattle, rabbits, and humans (Spencer et al., 2005; Figure 1.4). Interestingly, patterning of rodent glandular epithelial glands from LE occurs after birth, between P5 and P10 (Brody & Cunha, 1989). In contrast, in pigs, domestic cattle, and humans, the budding of GE is visible already upon birth (Spencer et al., 2005).

The endometrium in adult sheep and cattle is patterned into aglandular caruncles, formed by the dense stromal protuberances, covered by a LE, and glandular intercaruncular areas (Atkinson et al., 1984; Spencer et al., 2005). The intercaruncular areas of the endometrium contain many hundreds of glands in the uterine wall cross-section (Spencer et al., 2005). Interestingly, the superficial implantation of domestic cattle happens only inside the caruncular areas (Spencer et al., 2005). The mechanisms of endometrial patterning and morphogenesis, which spatiotemporally determine embryo implantation, remain largely unknown.

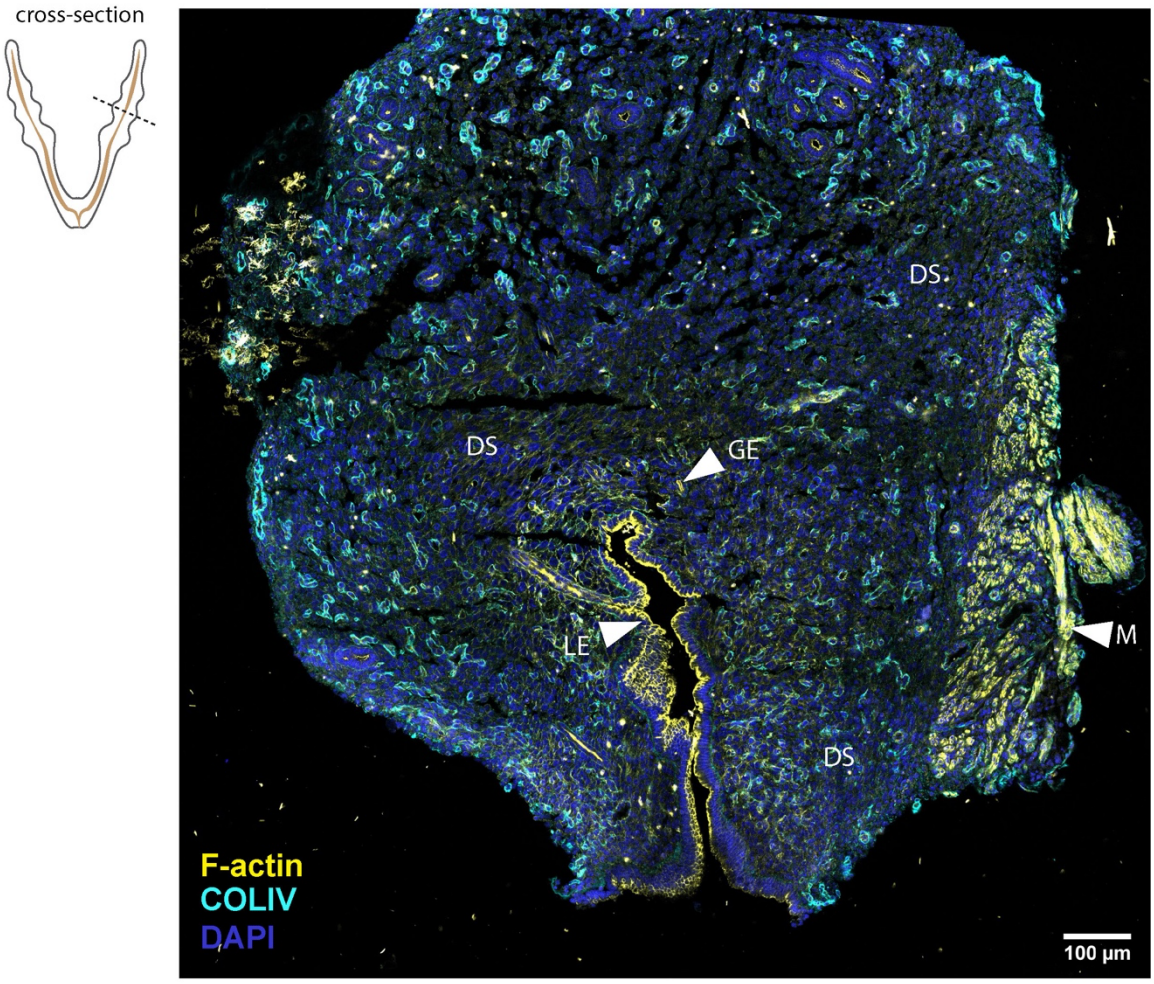

Figure 1.4 Immunofluorescence image of the representative E4.5 mouse uterus cross-section, stained for F-actin (yellow), Collagen IV (COLIV, cyan), and nuclei (DNA, blue). DS, decidual stroma; GE, glandular epithelium; LE, luminal epithelium; M, muscle tissue. Scale bar, 100 µm.

Transcriptomic studies suggest that decidual stroma emerged in therian mammals and formed a distinct cell type from endometrial stroma (reviewed by Wagner et al., 2014). The 'decidualization' of uterine stroma is essential for successful pregnancy. In a decidual reaction, spontaneously, or in response to fetal or artificial stimuli, the fibroblast-like mesenchymal stromal cells differentiate into epithelioid-like decidual cells (reviewed by Okada et al., 2018). Tissue thickening, proliferation, glycogen and fluid accumulation characterize differentiated decidua (Wagner et al., 2014). In humans, progesterone and protein kinase A (PKA) – mediated signaling are important to initiate decidual reaction (Wagner et al., 2014). Biochemical signals, produced by the decidual stroma, have been also described. The major secretory

products of decidual stromal cells include PRL and IGFBP-1, two proteins that have been used as markers of decidualization (Okada et al., 2018). In the decidual–placental interface, those proteins have been suggested to stimulate trophoblast growth and invasion, to prevent immune rejection, and to promote angiogenesis (Okada et al., 2018).

Uterine smooth muscles generate contractions autonomously as well as during pregnancy and birth. In duplex uteri of rodents, uterine contractility has been implicated in embryos positioning along the uterus (Flores et al., 2020).

1.7 Mammalian embryo development

Mammalian development begins with a fertilized zygote surrounded by a glycoprotein-rich Zona Pellucida (ZP). Totipotent blastomeres are formed by subsequent rounds of cleavages (cell divisions without significant cell growth). The emergence of the cavity between blastomeres marks a hollow spherical blastocyst stage.

The modes of blastocyst formation, its size, and morphology are strikingly variable across mammals. The blastocyst is unilaminar in studied marsupials (dunnart, opossum, and wallaby). It is formed by the adhesion of the blastomeres to the inner surface of ZP and subsequent proliferation and spreading along the ZP (Selwood et al., 1992). Marsupial blastocysts form pluriblast (pluripotent lineage analogous to eutherian inner cell mass), hypoblast (extraembryonic lineage analogous to eutherian primitive endoderm), and trophoblast (extraembryonic lineage which interacts with the maternal environment). Variation among the studied species can be noticed in the degree of embryo polarity and patterning dynamics (reviewed by Frankenberg et al., 2016).

The blastomeres of eutherians adhere to each other rather than to ZP, and a cavity is formed by pumping fluid in the intercellular space. Cavitation can begin as early as at the four and 16-cell stages, resulting in unilaminar blastocyst as in elephant shrew and tenrec (Frankenberg et al., 2016), reminiscent of marsupial blastocyst morphology. In most other eutherian species, a compact morula is formed prior to cavitation.

Inner Cell Mass (ICM) forms in eutherian mammals and becomes enveloped by the trophoblast. The timing and molecular mechanisms of lineage commitment within morula and ICM are substantially variable between the species; see review by (Niakan et al., 2012; Frankenberg et al., 2016; Rossant & Tam, 2022). Moreover, gestational time and the time of implantation also exhibit significant variation (Stern, 2004; pp 280-281).

Correlations between cavity formation, blastocyst size, and implantation mode in mammals are particularly intriguing. Rodents and primates undergo slight blastocyst expansion, whereas lagomorphs expand their blastocysts approximately 40-fold before implantation by day 6 (Alliston & Pardee, 1973; Warner et al., 2003). Strikingly, the bovine conceptus grows more than 1000-fold during 10-day elongation (Maddox-Hyttel, 2003; Frankenberg et al., 2016). In pigs, elongation is even more dramatic as the conceptus can reach more than 1.5 m in length during a short gestational window (Geisert et al., 1982; Frankenberg et al., 2016). Understanding the exact role of such blastocyst expansion will require experimental proof, but it seems to correlate with the rate of trophoblast invasiveness. As was introduced in the previous chapter, the rodent and human trophoblast are highly invasive. Such invasion leads to the formation of the haemochorial placenta, devoid of the maternal interface and with direct contact between blood and trophoblast. Placentation of pigs and cows is superficial (endotheliochorial), where maternal tissues are left almost intact. In that perspective, lagomorphs could be seen as ‘intermediate’ with haemochorial placentation but a less invasive phenotype than humans and rodents. Interesting questions are, *how do the implantation timing and the mode of feto-maternal interaction relate to the embryo growth and morphogenesis? What are the constraints imposed by the maternal tissue on the embryo and vice versa, and how do they cross-talk?*

1.8 Mouse embryo development before implantation

In mice, fertilization of the zygote and subsequent cleavages produce eight totipotent blastomeres. Subsequently, the mouse embryo undergoes compaction and forms a morula. Concurrent with compaction, cell polarization takes place. The first lineage segregation between the extra-embryonic trophectoderm (TE) and the Inner Cell Mass (ICM) is determined by the neighboring cell-cell contacts and the cell polarity

(Korotkevich et al., 2017). The acquisition of polarity results in nuclear Yap localization and CDX2 expression, which is required for TE lineage specification (Strumpf et al., 2005; Nishioka et al., 2009). The TE specification and commitment become irreversible by the late 32-cell stage. In contrast, ICM can still form TE up until the 64-cell stage by moving outside the rest of ICM or by Hippo signaling inactivation (Posfai et al., 2017). CDX2 (TE marker), OCT3/4, and Nanog (ICM markers) mutually inhibit each other during ICM/TE patterning (Niwa et al., 2005).

Between embryonic day (E) 3.25 and E4.5, ICM patterns and then segregates into primitive endoderm (PrE) and epiblast (EPI). At E3.5, PrE and EPI markers (GATA6 and Nanog, respectively) are expressed in a random “salt and pepper” pattern (Chazaud et al., 2006). EPI/PrE specification depends on a differential response to FGF (Yamanaka et al., 2010; Ohnishi et al., 2014; Kang et al., 2017). Mechanical cell surface fluctuations have been shown to regulate the sorting of EPI and PrE up until E4.5 (Yanagida et al., 2022). PrE, along with the TE, forms an inverted yolk sac placenta. PrE can also contribute to the endodermal gut (Nowotschin et al., 2019).

At E4.5, TE differentiates into EPI-attaching polar TE (pTE) and EPI-distant mural TE (mTE), which adheres to the uterine wall and initiates implantation. Compared to pTE, mTE decreases CDX2 expression, which might be regulated by the YAP-TEAD pathway and the uterine factors secreted in response to estrogen (Suzuki et al., 2022). It has been shown that $Fgfr1^{-/-}$ embryos fail to downregulate CDX2 in mTE, and that the differentiation of $Fgfr1^{-/-}$ trophoblast stem cells is impaired, indicating that FGF signaling is also involved in mTE differentiation from pTE (Kurowski et al., 2019).

1.9 Mouse embryo development during implantation

Implantation, by establishing a physical interaction between the extraembryonic tissues and the maternal uterine tissues, marks a critical developmental stage. In mice, TE tension release enables pTE cells to invaginate by apical constriction (Christodoulou et al., 2019; Ichikawa et al., 2022). Invaginated pTE forms the extraembryonic ectoderm (ExE) tissue. mTE differentiates into giant trophoblast (GT), while EPI and ExE proliferate and elongate to form an “egg cylinder.” The extraembryonic lineages neighboring the EPI, ExE, and visceral endoderm (VE)

derived from PrE play a key role in embryonic growth, patterning, and body-axis formation via mechanochemical signaling (Brennan J. et al., 2001; Rodriguez et al., 2005). Successful ExE/EPI patterning has been shown to facilitate the growth and morphogenesis of the neighboring epiblast by establishing BMP and FGF signaling landscapes (Di-Gregorio et al., 2007). Basal Reichert's membrane (RM) outlines the residual blastocyst cavity between the egg cylinder and the GT and continues into the basal membrane between EPI and PrE (Figure 1.5).

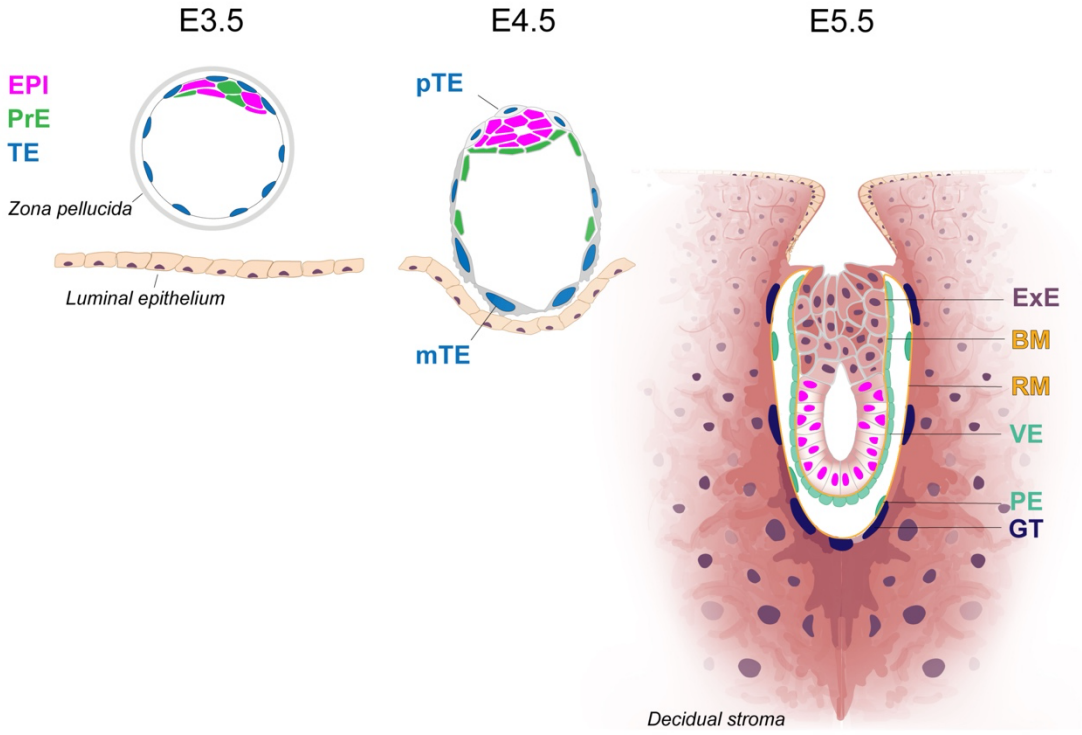

Figure 1.5 Mouse embryo development between E3.5 and E5.5. EPI (magenta), epiblast; PrE (green), primitive endoderm; TE (blue), Trophectoderm; pTE, polar TE; mTE, mural TE; ExE, extraembryonic ectoderm; BM, basal membrane; RM, Reichert's membrane; VE, visceral endoderm; PE, parietal endoderm; GT, giant trophoblast.

1.10 Embryo-uterine interaction during implantation in mice

Physical attachment between mTE and luminal epithelium starts at approximately E4.5 when the embryo is out of ZP. Several membrane-bound molecules that could mediate the initial phase of attachment have been found. Integrin alpha 7 subunit is considered to mediate embryo attachment to laminin *in vitro* and *in vivo* (Klaffky et al., 2001, 2005), lectins (Poirier et al., 1992), trophinin and tastin (Fukuda et al., 1995), perlecan (Carson et al., 1993) are present in TE. Other factors suggested to be involved in embryo-uterine interaction are Cripto (Gershon et al., 2018), osteoponin (Johnson et al., 2003), and EGF (Raab et al., 1996).

Uterine response to implantation is governed by female hormones estrogen and progesterone, acting on stroma and epithelium. Progesterone directly induces uterine Ihh expression in LE, and deletion of Ihh results in implantation failure (Lee et al., 2006). Another important factor, LIF, is expressed at the implantation sites and its uterine deletion also leads to implantation failure (Stewart et al., 1992; Song et al., 2000). *In vitro*, TB cells exhibit extensive phagocytotic activity (Rassoulzadegan et al., 2000). Upon recognition of LE, they extensively protrude between epithelial cells and eliminate them by entosis (engulfment) (Li et al., 2015).

The expression of BMP2 becomes upregulated in the proliferative and hypertrophic decidual stroma around the implanted embryo (Ying et al., 2000). Ablation of BMP2 leads to infertility due to a complete lack of decidual reaction (Lee et al., 2007). Hand2, Hoxa10, and Hoxa11 are other TF essential for decidual reaction in the stroma (see reviewed by Cha et al., 2012).

Uterine tissue geometry changes upon implantation. In particular, it is known that the mouse uterine tissues acquire elongated crypt geometry around the implanting embryo (Enders et al., 1980; Wewer et al., 1986; Yuan et al., 2016), suggesting embryo confinement.

1.11 Bottom-up approaches for studying implantation

Biomaterial engineering and microfabrication provide powerful tools for *ex vivo* modeling of the native 3D environment (Lutolf and Hubbell, 2005; Vianello and Lutolf, 2019; Bondarenko et al., 2022). Chemically-defined matrices, such as those based on

poly(ethylene glycol) (PEG), provide tunability, robustness, and reproducibility for state-of-the-art mechanobiological studies (Seliktar, 2012; Caliari and Burdick, 2016; Gjorevski et al., 2016; Qazi et al., 2022; Bondarenko et al., 2022).

Ex vivo culture of peri-implantation mouse embryos has been developed in 2D (Bedzhov et al., 2014) as well as in 3D (Govindasamy et al., 2021; Ichikawa et al., 2022). However, the 2D culture does not support in utero-like morphogenesis as the embryos adhere to the 2D surface, disrupting RM integrity. Similarly, the 3D culture so far has required artificial removal of the mTE to enable invagination and formation of the ExE (Ichikawa et al., 2022). Our previous study suggested the role of embryo-uterus interaction in tension release *in utero*. However, testing for the exact mechanism required an *ex vivo* system that recapitulates embryo-uterus interaction.

The 3D biomimetic system of the blastocyst co-culture with bEnd5 cell line has been introduced, which identified the PDGF signaling involvement in the trophoblast-epithelial attachment (Govindasamy et al., 2021). However, the same study did not address the functional role of embryo-uterine interaction in early embryo patterning and morphogenesis.

Therefore, development of the whole mouse embryo with embryonic and extraembryonic tissues through peri-implantation remains to be understood and achieved *ex vivo*.

1.12 Live imaging approaches

Studying tissue-scale and single-cell dynamics requires live imaging. Selective Plane Illumination Microscopy (SPIM) provides high image acquisition speed and low light doses suitable for long-term live imaging of light-sensitive samples, such as mouse embryos (Strnad et al., 2016; Power & Huisken, 2017). Previously, we and others successfully combined SPIM with pre-implantation (Strnad et al., 2016) and post-implantation (Ichikawa et al., 2014; McDole et al., 2018) mouse embryo culture for long-term live imaging. This allowed us to address tissue interaction mechanisms during peri-implantation EPI patterning (Ichikawa et al., 2022). However, the combination of SPIM imaging and microenvironmental engineering has not been implemented yet to study embryo-uterine interaction.

2 AIMS AND STRATEGY

The central goal of my Ph.D. study is to understand tissue coordination mechanisms during embryo implantation. Studying such processes requires experimental access, dynamic recording, and quantitative theoretical analysis. In my Ph.D., I aimed to establish such methods and, by using them, derive mechanistic knowledge of embryogenesis.

Implantation of the embryo leads to key changes in embryo morphology and environmental context. First, I established a new peri-implantation embryo culture method, where I applied bottom-up engineering to recapitulate uterine tissue properties. *Ex vivo* engineered uterine environment (3E-uterus) with geometrically patterned hydrogels supported mouse blastocysts through implantation and robust peri-implantation morphogenesis; promoted the development of the Reichert's membrane and all extraembryonic tissues, including giant trophoblast, which directly interacts with the uterus. Preservation of the giant trophoblast is a unique aspect of this method, which allowed me to find that the adhesion and geometry of the uterine environment are the most critical factors for peri-implantation embryogenesis in mice.

To further understand how adhesion and geometry control development, I aimed to access peri-implantation embryo dynamics. Thus, we complemented 3E-uterus with *in toto* live embryo imaging using the inverted and multi-view light-sheet microscopy techniques, as well as the computational image analysis. This allowed detection of changes in trophectoderm cell shape and tissue dynamics, embryo growth, and migration of the trophoblast. Live imaging and theoretical modeling showed that the trophoblast adhesion releases tension exerted upon the trophectoderm, resulting in invagination of the extra-embryonic ectoderm and the formation of the egg cylinder. Next, I show that to accommodate egg cylinder formation, trophoblast cells undergo Rac1-dependent collective migration upon implantation, displacing Reichert's membrane and generating space. I prove the coordination between trophoblast migration and embryo growth by experimentally manipulating the geometry of the engineered uterus and the trophoblast migration. In summary, this work provides new tools for studying embryo implantation and a new comprehensive tissue coordination model of peri-implantation development.

3 METHODS AND MATERIALS

Methods details were adapted from Bondarenko et al. 2022.

3.1 Molecular biology

3.1.1 Genomic DNA extraction

Genomic DNA was extracted from mouse tail or ear clip biopsies. The tissues pieces were digested in 400 µL by 0.5 mg/ml proteinase K (Merck, Cat No. P2308) in a buffer containing 1% SDS (sodium dodecyl sulphate, Serva, Cat No. 20767), 50mM Tris-HCl pH 8.0 (Thermo Fisher Scientific, Cat No. AM9855G), 100 mM NaCl, 100 mM EDTA pH 8.0 (Invitrogen, Cat No. 15575020). Enzymatic digestion was performed overnight at 56^{o}C with 450 rpm agitation using a thermo mixer (Thermomixer comfort, Eppendorf). Equal volume of 2-propanol was added and samples were centrifuged for 10 min at 14,000 rpm (Eppendorf, 5417R). After a wash with 70% ethanol, the DNA pellet was air-dried under the hood at room temperature, and dissolved in 125 µL of water.

For ddPCR, genomic DNA was extracted using standard phenol:chloroform:isoamyl alcohol (25:24:1) (Carl Roth, Cat No. A156.1) extraction method. Briefly, one volume of phenol:chloroform:isoamyl alcohol was added to the sample, centrifuged, and the aqueous phase was aspirated. gDNA was precipitated with one volume of 2-propanol and 1/10 volume 3M Sodium Acetate (pH5.2). DNA pellet was washed twice with 70% ethanol, air-dried under the hood at room temperature, and dissolved in ddH20.

3.1.2 Genomic DNA amplification

Polymerase Chain Reaction (PCR) was used to amplify DNA (Thermo Fisher Scientific, EP0401, F-530; Takara, RR01). Primers were designed using primer3 and primer-BLAST (Ye et al., 2012) software (https://bioinfo.ut.ee/primer3-0.4.0/primer3/). For mouse genotyping procedures see Appendix 1, primers and PCR product sizes.

3.1.3 Single embryo genotyping

Individual embryos were mouth pipetted into 200 µl PCR tubes containing 10 µl of lysis solution of 200 µg/ml Proteinase K in Taq polymerase buffer (Thermo Fischer Scientific, B38). The lysis reaction was carried out for 1 h at 55°C, followed by 10 min at 96°C. The resulting genomic DNA was mixed with relevant primers (Appendix 1) for determination of genotype via PCR.

3.1.4 Droplet digital PCR

Droplet digital PCR was used to estimate copy numbers of Brainbow constructs after the targeted genome integration. Primers and fluorescent probes against Brainbow constructs were designed with primer3 and primer-BLAST (Ye et al., 2012) software (https://bioinfo.ut.ee/primer3-0.4.0/primer3/) (see Appendix 2). Annealing temperature was estimated with OligoCalc (http://biotools.nubic.northwestern.edu/OligoCalc.html) using 300 nM primer concentration and 50 nM salt concentration. gDNA concentration was measured using Qubit dsDNA HS assay (Thermo Fisher Cat No. Q33231). gDNA was digested with Mse-I (NEB) overnight at 37 ^{o}C. The ddPCR reactions were prepared according to the manufacturer's instructions (Biorad, 10031906) using digital PCR supermix for probes (Biorad, Cat No. 186-3023) and consumables (Biorad, #1863005, #1864008, #1863009) for QX200 Droplet Digital PCR System. Results were processed using QuantaSoft software (Biorad), copy number was estimated by normalization to the control probe signal in Rpp30 and Col1a1 loci.

3.1.5 Molecular cloning

Plasmids were cloned using standard cloning procedures or Gibson assembly. Oligonucleotides in concentration of 2 pmol/µl were annealed in a buffer containing 10 mM Tris-HCl, pH 8.0 (Thermo Fisher Scientific, Cat No. AM9855G), 50 mM NaCl, 1 mM EDTA (Invitrogen, Cat No. 15575020) under slow cooling from 95 ^{o}C to the room

temperature. DNA ligation was set up following manufacturer's instructions (NEB, M0202). Plasmids were transformed using standard heat-shock method into chemically-competent DH5 alpha *E.Coli* cells. BACs were transformed using standard heat-shock method into 10b *E.Coli* cells. Colony screening was performed using One Taq polymerase kit (M0480, NEB).

Brainbow constructs, Nucbow, Mitbow, and Palmbow, were obtained from J. Livet (Loulier et al., 2014). Nucleus-tagged iRFP was introduced under the CAG promoter of Mitbow, Palmbow, and Nucbow constructs. FRT-flanked Neomycin gene was inserted after the fluorophores in the Palmbow construct. To prevent cross-reactivity with other recombination sites, the alternative Lox1-M2, 5171, 66 sites were introduced into Mitbow (Figure 3.1).

To insert Brainbow construct cassette into the Col1a1 locus (Beard et al., 2006), homologous arms were amplified from mouse gDNA using Phusion high-fidelity polymerase (F-530) and cloned into a modified pBeloBAC11 vector (pBeloBACnMCS-DTA). Sph-I restriction site was replaced with Mlu-I restriction site. Nucbow, Mitbow, and Palmbow constructs were assembled as an array into pBeloBACnMCS-DTA-Col1a1-MluI construct. The resulting plasmid (pBB08_pBeloBACnMCS-DTA-Col1a1-MluI(Nucbow-Mitbow-Palmbow, Appendix 3) was isolated using QIAGEN Large-Construct Kit (Cat No. 12462).

Tamoxifen-inducible Cre (ERT2-CRE) was inserted into pR26 plasmid (#127372) for expression under endogenous R26 promoter. Puromicin gene was provided under PGK promoter (pR26_CRE_ERT2_Puro, Appendix 4).

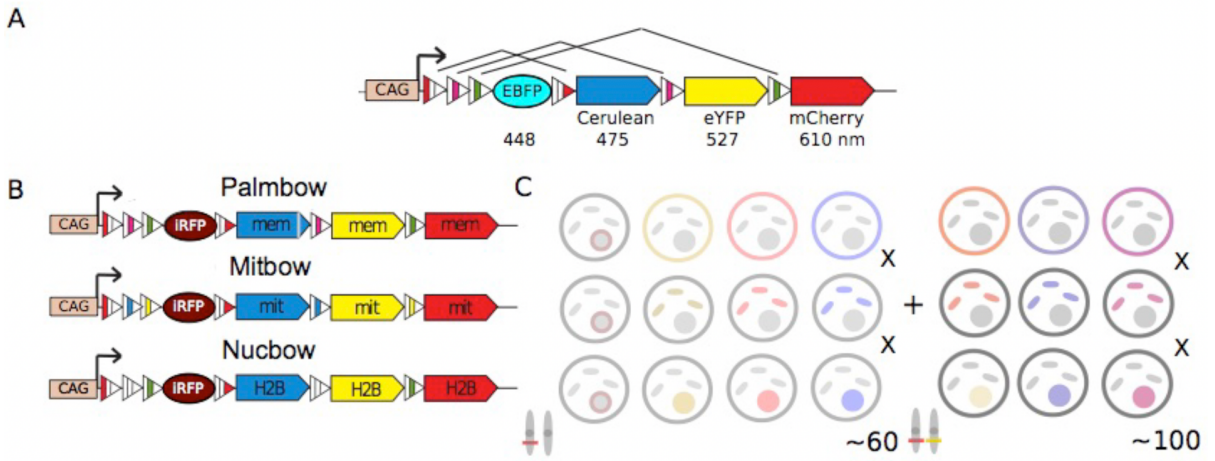

Figure 3.1. A. Scheme of the original Brainbow construct (Loulier et al., 2014). Potential Cre-recombination events between identical lox sites (rectangles) are marked with connecting black lines. Emission maxima of the corresponding fluorophores are indicated in numbers. B. Transgenic constructs with FPs, targeted to the plasma membrane (Palmbow), mitochondria (Mitbow), and nucleus (Nucbow). C. Corresponding cell labelling patterns in case of single-copy hemizygous genomic insertion of each construct (left) and examples of additional hues available for multi-copy heterozygous insertions (right).

3.1.6 Targeted genome integration

sgRNA to target Col1a1 (5'-GAGCCAGCATGCTATCGTCC-3') and ROSA26 (5'-GACTCCAGTCTTTCTAGAAGA-3') loci were designed using chop-chop (https://chopchop.cbu.uib.no) and cloned separately into px330A-1x6 vectors (#58770), expressing Cas9 and sgRNAs under U6 promoter. First round of electroporation provided transient expression of Cas9 and anti-Col1a1 sgRNA to incorporate pBB08_pBeloBACnMCS-DTA-Col1a1-MluI(Nucbow-Mitbow-Palmbow) plasmid into mouse Col1a1 locus. The second round of electroporation provided transient expression of Cas9 and anti-R26 sgRNA to incorporate ERT2-CRE into mouse ROSA26 locus. Genome integration was validated by Ramona Bloehs using Southern blot assay.

3.2 Cell biology

3.2.1 Embryonic stem cell culture, electroporation

Mouse embryonic stem cell (ESCs) line R1 was used for transgenesis. Prior to ESC culture, inactivated mouse embryonic fibroblasts (MEFs) were unfrozen and plated. MEFs were cultured in the medium, based on DMEM (Gibco, Cat No. 41965), supplemented with 10% heat-inactivated Fetal Bovine Serum (PAA, A15-080), 2mM glutamine (Gibco, Cat No. 25030), and 50 U/ml PenStrep (Gibco, Cat No. 15070).
For ESC culture, MEF medium was exchanged to a freshy prepared ESC medium, based on DMEM (Gibco, Cat No. 41965), supplemented with 20% heat-inactivated Fetal Bovine Serum (PAA, A15-080), 1X non-essential amino acids (Gibco, Cat No. 11140), 1X nucleosides (Millipore, Cat No. ES-008-D), 2 mM glutamine (Millipore, K0282-BC), 100 µM beta-mecaptoethanol (), 50 U/ml PenStrep (Gibco, Cat No. 15070), 10U/L LIF (Gibco, Cat No. 3275SB), 25 mM HEPES pH 7.3 (Sigma, Cat No. H-0887). ESCs were plated at the density 1-3x10^6 cells per 60 mm dish. ESC medium was exchanged daily, upon confluence, cells were split and replated to the initial density.

ESC electroporation of a total 4 µg circular plasmid DNA was performed by Ramona Bloehs with Human Stem Cell Nucleofector Kit 2 (Lonza, Cat No. VPH-5022), program A-023. Selection with Geneticin (G418 Sulfate, Cat No. 10131035) started 36-48 hours after electroporation. Positive clones were expanded and evaluated for fluorescence by live imaging.

3.2.2 Endometrial organoid derivation and culture

The protocol was adapted from (Boretto et al., 2017). Female mouse estrous cycle staging was determined as described (Caligioni et al., 2009). 2-3 B6C3F1 female mice in estrus stage were used per experiment. Dissected uterine horns were cut longitudinally to expose endometrium and washed tree times in ice-cold DPBS (Gibco, Cat No. 14190144). Endometrium was cut out from the muscle tissue with surgical

scalpel (Harvard Apparatus, Cat No. 72-8374) and minced into small pieces using surgical scissors (Science Tools, Cat No. 15006-09). Endometrium pieces were washed three times with ice-cold DPBS in a 50 ml tube on ice by allowing tissue pieces to settle by gravity. Tissue dissociation was performed in 30mM EDTA supplemented with Y-27632 (Stemcell, Cat No. 72304) on ice. Tissue pieces was centrifuged at 85g for 2 min at +4^{o}C, washed and resuspended in DPBS supplemented with 0.1% BSA using a pre-wet serological pipette. Suspension was shaken by hand to facilitate release of uterine epithelial crypts. The supernatant was gently aspirated and filtered through a 70 µm cell strainer (pluriSelect, Cat No. 43-50070) on ice. The procedure was repeated, eluate fractions were collected, examined under the microscope for enrichment with uterine crypt fragments. The fractions were centrifuged at 110g for 5 min at +4^{o}C and the pellets were resuspended in 70% Matrigel (Corning, 356230, lot. 7345012) (thawed on ice) and gently resuspended multiple times for homogeneity. 30 µl domes were made on the pre-warmed 48-well plates and left to solidify for 10 min, after which the dish was flipped to facilitate even distribution of the organoids. Upon Matrigel solidification, organoids were cultured in a WRN conditional organoid culture medium (supplied by M. Lutolf lab, EPFL), supplemented with B27 (Life Technologies, Cat No. 17504044), N2 (Life Technologies, Cat No. 17502048), ITS-X (Gibco, Cat No. 51500-056), 100 µM Nicotinamide (Sigma Aldrich, Cat No. N0636), 500 µg Primocin (InvivoGen, Cat No. ant-pm-05), 200 ng/µl EGF (R&D Systems Cat No. 2028-EG-200), 50 ng/µl FGF10 (Peprotech Cat No. 100-26), A83-01 (Merck, Cat No. SML0788), and, during the first few days, 10 µM Y-27632 (Stemcell, Cat No. 72304). Organoids were dissociated with TrypLE, supplemented with 10 µM Y-27632 and 1mM N-acetylcysteine (Merch, Cat No. A7250).

3.3 Mouse embryology

3.3.1 Recovery, manipulation, and culture of pre-implantation stage embryos

Female estrous cycle synchronization was used to increase the natural mating efficiency (Whitten M. K., 1957). The embryonic day 0.5 (E0.5) was defined as noon on the day when a vaginal plug was detected. Pre-implantation mouse embryos were flushed from the uteri of the plugged females with 37 °C KSOMaa with HEPES (Zenith Biotech, ZEHP-050, 50 ml) using a syringe equipped with a cannula (Acufirm, 1400 LL 23). Embryos were handled using an aspirator tube (Sigma, A5177), connected to a glass pipette pulled from a glass microliter pipette (Blaubrand intraMark, 708744). Procedures were performed under a stereomicroscope (Zeiss, StreREO Discovery.V8) equipped with a thermal plate (Tokai Hit) at 37°C (Behringer et al., 2014).

3.3.2 Recovery and manipulation of peri-implantation stage embryos

Peri-implantation embryos were dissected from uteri using no 5. Dumont fine forceps (Dumont, 11254-20) in DMEM (Gibco, Cat No. 11880028) supplemented with 15% heat-inactivated FBS (PAA, Cat No. A15-080), 2 mM GlutaMAX (Gibco, Cat No. 35050061), and 10 mM HEPES (Sigma, Cat No. H0887), as described (Nagy et al., 2003).

3.3.3 Peri-implantation embryo culture

In vitro culture medium 1 and 2 (IVC1 and IVC2, respectively) (Bedzhov et al., 2014) were prepared from Advanced DMEM/F12 (Gibco, Cat No. 12634010), supplemented with 20% heat-inactivated FBS (Biosera, Cat No. FB1001S) and 30% KSR (Gibco, Cat No. 10828010), respectively. 1X Glutamax (gibco, Cat No. 02595), 1X ITS-X (gibco, Cat No. 51500-056), penicillin (25 units/ml)/streptomycin (25 µg/ml) (gibco Cat No. 15070-063), 8 nM beta-estradiol (Sigma, E8875-250MG), 200 ng/ml Progesterone

(Sigma P0130-25MG), 25 μM N-acetylcysteine were added. The mix was filtered through 0.22 μm filter (Merck, Cat No. SLGVV255F), aliquoted, stored at +4^{o}C, and used within two weeks.

After recovery at noon on embryonic day 3.5 (E3.5), embryos were serially transferred to IVC1 microdrops in a culture dish covered with mineral oil (Sigma, Cat No. M8410-1L). The time of embryo culture was counted from the time of embryo recovery (D0 = E3.5). In approximately one hour after recovery, embryos were shortly treated in Tyrode's solution (Sigma, Cat No. T1788) to remove *Zona pellucida*, washed repeatedly (Behringer et al., 2014), and left in a culture dish with IVC1 medium for at least an hour inside the incubator. Embryos were routinely cultured inside the incubator with a humidified atmosphere with 5% CO2 at 37^{o}C (Thermo Scientific, Heracell 240i).

3.3.3.1 2D embryo culture

On day 0 (E3.5 recovery), zona-free embryos were placed inside inner wells of a pre-warmed glass-bottom μ-Slide Angiogenesis dish (ibidi, Cat No. 81506), filled with 45 μl IVC1 medium. Upon embryo attachment, the medium was gently aspirated and exchanged to IVC1, and to IVC2 in 48 h (day 2).

3.3.3.2 3D hydrogel-embedded embryo culture

LDTM PEG hydrogel components were mixed on ice. 15 μl of the mix was added to an inner well of a pre-warmed μ-Slide Angiogenesis dish, and embryos were carefully transferred and mixed inside the hydrogel (2-3 embryos per drop). To prevent embryos from adhering to glass or reaching gel surface, the dish was flipped regularly during gel solidification inside the incubator. 35 μL of pre-warmed IVC1 medium were then added to each well. The medium was exchanged shortly to IVC1 and then again to IVC1 in 24 h (Day 1) and to IVC2 in 48h (Day 2).

3.3.3.3 Peri-implantation embryo culture in 3E-uterus

Hydrogels with microfabricated crypts (see “Fabrication of topographically patterned hydrogels”) were equilibrated in 3 ml of IVC1 medium in the incubator for at least 12 h prior to 3E-uterus embryo culture. ZP-free embryos were carefully positioned inside microfabricated hydrogel crypts in a downward mTE orientation with a fused tip of a thin glass pipette. The medium was exchanged to IVC1 in 24 h (Day 1) and to IVC2 in 48h (Day 2).

3.3.4 Pharmacological treatments

Embryos were recovered at E3.5 (D0) and manipulated according to the 3E-uterus protocol. Embryos from the same litter were split into two isolated TruLive3D dish compartments for parallel treatment and control live imaging. Live imaging started at 30 h counted from the time of embryo recovery. A single mTomato channel was illuminated with a 561 nm laser every 20 min during all live imaging intervals. At 36 h, IVC1 medium in one compartment was exchanged to IVC1 medium supplemented with 100 μM NSC23766 and in another compartment to IVC1 medium supplemented with an equal amount of H2O (control). At least three rounds of medium exchange were performed with a several-minute incubation time in between to equilibrate the hydrogel in both treatment and control conditions. Imaging restarted at 37 h until 48 h. Between 48 and 49 h, the medium was similarly exchanged to IVC2 for both the treatment and the control conditions. Live imaging restarted at 49 h and continued until 72 h, after which embryos were fixed and immunostained. Image voxel size: 0.208×0.208×1.000 μm^3 along the X, Y, and Z axes, respectively.

3.3.5 Uterine tissue sectioning

Pregnant mouse uteri were dissected and handled in KSOM with HEPES. To reduce non-physiological uterine contraction due to the release from connecting tissues, uteri were transferred to pre-warmed 0.5 M MgCl2 solution. Uteri were cut into pieces corresponding to the embryo implantation sites, as visually judged by their swollen and opaque appearance under the stereomicroscope. Tissue pieces were immediately

fixed in 4% PFA in PBS overnight at 4°C, followed by an overnight wash in PBS at 4°C, and subsequent overnight washes in 12% Sucrose, 15% Sucrose, and 18% Sucrose at 4°C until further use within two weeks. The tissue pieces were dried with KIMTECH paper (Kimberly-Clark) and mixed with M-1 Embedding Matrix for cryosectioning (ThermoScientific, Cat No. 1310TS). Tissue pieces were mounted and orientated in M-1 Embedding Matrix in Tissue-Tek cryomold (Sakura) and frozen at -80°C.

Cryosectioning was performed with Leica CM3050S cryotome at -16°C, to produce sections of 15-20 µm thickness using low profile microtome blades (Accu-Edge, Sakura). Tissue sections were dried at room temperature, washed in PBST, and permeabilized for 15 min using 0.5% Triton X-100 in PBS. Immunostaining was performed as described below.

3.4 Mouse animal work

3.4.1 Husbandry

All animal work was performed in the Laboratory Animal Resources (LAR) at the European Molecular Biology Laboratory (EMBL) with permission from the Institutional Animal Care and Use Committee (IACUC) overseeing the operation (IACUC number TH11 00 11). LAR is operated according to the Federation of European Laboratory Animal Science Associations (FELASA) guidelines and recommendations. All mice were housed in IVC cages in pathogen-free conditions with 12-12 hours light-dark cycle and used for experiments at the age of 8 to 35 weeks.

3.4.2. Strains

The following mouse lines were used in this study: a F1 hybrid strain between C57BL/6 and C3H (B6C3F1) as wild-type (WT), Cdx2-GFP (Mcdole and Zheng, 2012), mTmG (Muzumdar et al., 2007), H2B-GFP (Hadjantonakis and Papaioannou, 2004), Lifeact-GFP (Riedl et al., 2010), GFP-Myh9 (Zhang et al., 2012), ZO1-GFP (Foote et al., 2013). $Rac1^{flox/flox}$ conditional allele (Walmsley et al., 2003) was crossed with ZP3-Cre line (Lewandoski et al., 1997) to generate $Rac1^{+/-}$ animals. To obtain zygotic $Rac1^{-/-}$ embryos, $Rac1^{+/-}$ females were crossed with $Rac1^{+/-}$ males.

3.5 Engineering and microfabrication

Hydrogel components were synthesized by Saba Rezakhani from M. Lutolf's lab at EPFL. Fabrication of stamps for topographical patterning of the hydrogels was performed by Mikhail Nikolaev from M. Lutolf's lab at EPFL. Fabrication of topographical patterned hydrogels was performed in collaboration with Mikhail Nikolaev from M. Lutolf's lab at EPFL. Design and fabrication of MuVi-SPIM sample mounting components were performed in collaboration with Dimitri Kromm from J. Ellenberg's lab at EMBL. This section is adapted from (Bondarenko et al., 2022), where co-authors contributed to writing some of the method descriptions.

3.5.1 Hydrogel preparation

LDTM hydrogels were formed by Michael type addition of PEG-PEP precursors onto 8-arm PEG-VS. To make hydrogel networks of desired final PEG content, proper volumes of 10% (w/v) 8-arm PEG-VS in TEA and 10% (w/v) PEG-PEP in water were mixed in molar stoichiometric ratio of VS/SH=0.8. For conditions containing RGD adhesion peptide (Ac-GRCGRGDSPG-NH2, mol wt 1002.04 g/mol), different volumes of RGD were added to the mix before addition of the PEG-PEP precursor, and the molar ratio of VS/TH was adjusted as VS/(TH-RGD)=0.8. For example, to make 100 µL of LDTM hydrogels of 2.**2**5% (w/v), taking into account RGD concentration, 8.8 µL of 8-arm PEG-VS, 10 µL of TEA buffer, 65 µL of distilled water and 16.20 µL of PEG-PEP were mixed on ice.

3.5.2 Fabrication of stamps for topographical patterning of the hydrogels

The models designed in Autodesk Inventor were printed using conventional soft-lithography methods established at the Center of Micronanotechnology (CMi, EPFL) (Nikolaev et al., 2020).

3.5.3 Fabrication of sample mounting components for MuVi-SPIM

The master molds featuring an inverted design of a tube holder and a cup were produced in teflon using custom microfabrication methods established at EMBL Mechanical Workshop. For a tube holder and a cup preparation out of PDMS, elastomer and a curing agent (Sylgard 184, Dow Corning) were mixed at a 10:1 ratio (w/w). After degassing in a vacuum chamber, the mixtures were baked at 60 °C in the oven overnight.

3.5.4 Fabrication of topographically patterned hydrogels

To prevent hydrogel adhesion, elastomeric stamps containing the desired geometries were coated with bovine serum albumin in PBS (1% w/v in PBS; Thermo Fisher Scientific) for overnight. Before use stamps were washed once with distilled water and dried under the hood. For hydrogel casting, PDMS ring holders were placed on the bottom of the 3.5 cm dish and UV sterilized prior use. A drop of liquid hydrogel precursor (see Hydrogel Preparation) was made in the center of the ring spacer and a stamp with microtopography was placed atop. After 30-40 min polymerization in the incubator (37 C) stamps were removed and hydrogels covered with PBS. Hydrogels were used either the same day or stored for about one week.

3.5.5 Evaluation of 3E-uterus efficiency

Efficiency was quantified as a percentage of successfully developed embryos among all embryos at day 3 of 3E-uterus. 3E-uterus embryo were classified as successfully developed if three criteria were met (Figure 4.4. A):
I. Egg cylinder formation, defined as EPI tissue located within a VE layer with the basal membrane in between.
II. Alignment of the egg cylinder axis with the crypt axis. The embryos with an evident upward egg cylinder orientation were excluded from quantifications due to an experimental error of embryo positioning (corresponding to less than 5% of samples).
III. Formation of the Reichert's membrane, determined as a basal membrane underneath TB which, at the top of the egg cylinder, was required to continue into the basal membrane between EPI and VE.
To directly assess the criteria I-III, the simultaneous immunostaining against OCT3/4, GATA4, Collagen IV, or pan-Laminin, and nuclei (DAPI), was performed each time. For evaluation of 3E-uterus efficiency, three independent experiments were performed, among which 46% of embryos (12 of 26) met all the above-mentioned criteria.

Efficiencies for crypt diameter evaluation (Figure 4.4B) were calculated as follows:

80 µm crypt diameter: 0/4, 0/5, and 1/8 (the number of successfully developed embryos divided by the total number of embryos); three independent experiments.
100 µm: 0/3, 2/9, and 2/8; three independent experiments.
120 µm: 1/3, 1/5, and 2/5; three independent experiments.
140 µm: 3/8, 2/5, 1/3, 2/7, 1/4; five independent experiments.
160 µm: 2/4, 0/5, 1/5; two independent experiments.

Efficiencies for the hydrogel stiffness evaluation (Figure 4.5B, C) were calculated as follows:

1.5% PEG-PEP content: 3/8, 3/8, and 2/8 (the number of successfully developed embryos divided by the total number of embryos); three independent experiments.
1.75%: 3/9, 5/8, 2/7, and 4/8; four independent experiments.
2%: 2/7, 3/6, and 4/6; three independent experiments.

2.25%: 0/6, 6/13, and 1/5; three independent experiments.

2.5%: 1/6, 2/7, and 4/17; three independent experiments.

2.75%: 1/9, 5/15, and 1/9; three independent experiments.

6%: 1/6, 0/7; two independent experiments.

7%: 1/11, 0/5; two independent experiments.

3.6 Microscopy

3.6.1 Immunofluorescence preparation and staining

Recovered embryos were fixed with 4% paraformaldehyde (Electron microscopy sciences, 19208) in PBS for 15 minutes at room temperature. For *ex vivo* cultured embryos, the hydrogel with embryos was gently dissected and fixed with 4% paraformaldehyde for 30 minutes at room temperature with gentle agitation. For immunostaining of active integrin and di-phosphorylated myosin regulatory light chain (ppMRLC), fixation was performed in 1% PFA in PBS supplemented with MgCl2. The samples were subsequently washed in PBST buffer (0.1% Tween-20 in PBS; Sigma, 85113), *ex vivo* cultured embryos were carefully dissected from the hydrogel at this step. Permeabilization was performed with 0.5% Triton X-100 (Sigma, Cat No. T8787) in PBS for 30 minutes at room temperature with gentle agitation. After several washes in the wash buffer (2.5% BSA (Sigma, Cat No. A9647) in PBST), embryos were incubated in the blocking buffer (5% BSA in PBST) overnight at 4°C. Embryos were stained with primary antibodies diluted in the blocking buffer overnight at 4°C. After washes, embryos were incubated with secondary antibodies diluted in the wash buffer for 2 hours at room temperature with gentle agitation. Staining with Rhodamine Phalloidin (Invitrogen, Cat No. R415) diluted at 1:500 was performed together with secondary antibodies. Subsequently, embryos were washed in PBST with DAPI (Invitrogen, D3571) at 5 µg/mL and mounted in PBST.

Primary antibodies against Gata4 biotinylated (R&D systems, Cat No. AF2606), Sox2 (Cell Signaling, Cat No. 23064), TFAP2C (Cell Signaling, Cat No. 2320), CDX2 (Biogenex Laboratories, Cat No. MU392AUC), PARD6B (Santa Cruz Biotechnology, Cat No. sc-67393), pan-Laminin (Novus Biologicals, Cat No. NB300-144SS), Collagen IV (Millipore, Cat No. AB756P), Fibronectin (Proteintech, Cat No. 15613-1-AP), ITGB1 (Millipore, Cat No. MAB1997), GFP (chromotek, Cat No. gb2AF488) were diluted at 1:200. Primary antibodies against active ITGB1 (12G10) (Santa Cruz Biotechnology, Cat No. sc-59827), ZO1 (Invitrogen, Cat No. 33-9100), di-phosphorylated myosin regulatory light chain (ppMRLC) (Cell Signaling, Cat No. 3674), phosphorylated ERM (pERM) (Cell Signaling, Cat No. 3726) were diluted at 1:100. Primary antibodies

against Oct3/4 (Santa Cruz Biotechnology, Cat No. sc-5279) and KRT8 (Troma-1-C, Cat No. AB531826) were diluted at 1:50.

The following secondary antibodies were used at 1:400: donkey anti-goat IgG Alexa Fluor 488 (ThermoFisher, Cat No. A11055), donkey anti-rat IgG Alexa Fluor 488 (ThermoFisher, Cat No. A21208), donkey anti-mouse IgG Alexa Fluor 488 (ThermoFisher, Cat No. A21202), donkey anti-rabbit IgG Alexa Fluor Plus 546 (Invitrogen, Cat No. A10040), donkey anti-goat IgG Alexa Fluor Plus 555 (Invitrogen, Cat No. A21432), donkey anti-mouse IgG Cy5 AffiniPure (Jackson ImmunoResearch, Cat No. 715-175-150), donkey anti-rabbit IgG 647 (ThermoFisher, Cat No. A31573).

3.6.2 Confocal microscopy

Confocal imaging was performed on Zeiss LSM 780 Confocal Inverted Microscope with LD C-Apochromat 40×/1.1 W Corr objective, using Zen 2012 LSM Black software and LSM 880 Airyscan Confocal Inverted Microscope with a C-Apochromat 40x/1.2 NA water immersion objective, using Zen 2.3 SP1 Black software v14.0.0.0. Nuclear immunostaining of OCT3/4, GATA4, and TFAP2C were imaged by LSM780 or LSM880 confocal mode with 1 µm Z spacing. Alternatively, immunostainings of embryos and tissue sections were imaged with Airyscan Optimal or Superresolution modes with optimal Z spacing, calculated based on the used imaging settings. The following lasers were used: diode 405 nm, argon multi-line 458/488/514 nm, HeNe 561 nm and 633 nm. Raw Airyscan images were processed by ZEN 2.3 SP1 Black software v14.0.0.0 or v14.0.12.201.

3.6.3 Inverted Selective Plane Illumination Microcopy (InVi-SPIM)

Array of micro-cavities was fabricated inside the PEG hydrogel-filled TruLive3D dishes using custom PDMS stamp, containing a single row of micro-cavities (see “Fabrication of stamps for topographical patterning of the hydrogels”). The dish bottom was covered with 35 µL of the LDTM PEG hydrogel mix; the PDMS stamp was carefully placed parallel to the side of the future detection objective. After hydrogel solidification for 30-

40 min in the incubator, 200-300 µL of PBS was added atop and the stamp was pulled out with forceps. For equilibration, several washes with IVC1 medium were performed before embryo culture. Embryos were carefully implanted into crypts in a downward mTE orientation, IVC1 medium was added up to 115 µL, and covered with 250 µL mineral oil to prevent evaporation during live imaging. IVC medium was exchanged as described (see "Peri-implantation embryo culture"). Live imaging was performed under 5% CO2 and 19.5% O2 atmospheric conditions at 37 °C inside the environmentally-controlled imaging chamber (Strnad et al., 2016). InVi-SPIM was equipped with Nikon 25x/1.1NA water immersion detective objective, Nikon 10x/0.3 NA water immersion illumination objective, and CMOS camera (Hamamatsu, ORCA Flash4.0 V2). Voxel size: 0.104×0.104×1.000 µm3 along the X, Y and Z axes, respectively. The following lasers and filters were used: 488 nm and BP525/50, 561 nm and LP561. Exposure time was set to 50 ms. Imaging was performed with line-scan mode in LuxControl (Luxendo).

3.6.4 Multi-View Selective Plane Illumination Microcopy (MuVi-SPIM)

3.6.4.1 Custom sample holder assembly and embryo mounting

We developed a new engineering approach to precisely position the embryo within the hydrogel microenvironment. Our design prevented the embryo from exchanging liquid with the rest of the imaging chamber, providing sterility and efficient usage of the culture medium.

The sample holder encompasses two transparent and gas permeable FEP tubes. The outer tube ($\varnothing_{inner}$ = 1.7 mm, $\varnothing_{outer}$ = 1.8 mm) contains the medium and is held and sealed by PDMS-filled capillary from the bottom and by the cup from the top. The inner tube ($\varnothing_{inner}$ = 1.05 mm, $\varnothing_{outer}$ = 1.15 mm) is supported by the tube holder made of PDMS. Molds for the tube holder and the cup were made in teflon using custom microfabrication. For PDMS preparation, elastomer and a curing agent (Sylgard 184, Dow Corning) were mixed at a 10:1 ratio (w/w). After degassing in a vacuum chamber, molds were baked in the 60 °C oven overnight.

A single-embryo cavity was cast inside the PEG hydrogel-precursor filled inner FEP tube using a custom single-embryo shaped PDMS stamp. IVC medium was exchanged several times inside the outer tube to equilibrate the hydrogel. The embryo was carefully mounted with a glass pipette from the opening of the outer tube, closed with a cup, and immediately placed in the incubator. IVC medium was exchanged twice per day.

3.6.4.2. Microscope and imaging settings

The microscope was equipped with Olympus 2 mm WD 20x/1.0 NA water immersion detective objectives, Nikon 3.5 mm WD 10x/0.3 NA water immersion illumination objectives, and CMOS camera (Hamamatsu, ORCA flash4 V2), Nikon TI-E 1× tube lens. Voxel size: 0.295×0.295×1.000 μm3 along the X, Y, and Z axes, respectively; image size: 302.08×604.15×150-250 μm. The following lasers and filters were used: 488 nm and BP525/50, 561 nm and LP561. Dual light-sheet was used in line-scan mode with a slit width of 40 px. Exposure was set to 30 msec. To support long-term embryo viability, we implemented atmospheric and temperature regulation of the MuVi-SPIM imaging chamber. Live imaging was performed under 5% CO2 and 19.5% O2 atmospheric conditions at 37 °C inside the environmentally-controlled imaging chamber.

3.7 Data processing and analysis

Cell membrane and nuclei segmentation were performed in collaboration with A. Wolny, A. Kreshuk's group at EMBL. The 3D volumes of the cell nuclei data acquired with the confocal microscope, and the cell plasma membrane data acquired with the light-sheet microscope were segmented using PlantSeg, a generic pipeline for volumetric segmentation (Wolny et al., 2020). The pipeline consists of two steps. In the first step, a convolutional neural network (CNN) predicts the boundaries of the objects (either cells or nuclei). In the second step, a region adjacency graph is constructed based on the CNN output, and the final segmentation is provided by partitioning of the graph (Beier et al., 2017; Funke et al., 2019; Wolf et al., 2019). The network training and the used segmentation algorithms are described below.

3.7.1 SPIM image processing

The volumes acquired with the left and right cameras were fused using Luxendo Image Processor (v2.4.1.). For further quantification and analysis, image drift was corrected in Fiji with BigDataProcessor2 plug-in (Tischer et al., 2021).

3.7.2 Cell membrane segmentation

The data volumes were acquired with MuVi-SPIM (see "Multi-View Selective Plane Illumination Microcopy (MuVi-SPIM)"). A dedicated 3D UNet was trained to predict the foreground membrane mask, which was used for the final cell segmentation with PlantSeg's 'GASP' agglomeration algorithm. The ground truth for the network training was bootstrapped by initially segmenting the stacks with pre-trained PlantSeg models ('confocal_unet_bce_dice_ds2x'), followed by manual correction of the erroneous cells with Paintera. In total, four annotated stacks were used for training and one for validating the network. Both nuclei and membrane UNets were trained using Adam optimizer (Kingma and Ba, 2014) with $\beta1=0.9$, $\beta2=0.999$, L2 penalty of 0.00001, and initial learning rate $\epsilon=0.0002$. Networks were trained until convergence for 100K

iterations, using the PyTorch framework (Paszke et al., 2019). The models with the best score on the validation set were selected.

3.7.3 Nuclei segmentation

The 3D data volumes were acquired with either LSM780 or LSM880 in a confocal mode with a voxel size of 0.207×0.207×1 μm^3 or 0.23.23×0.23×1 μm^3, for X, Y, and Z dimensions, respectively. The channels corresponding to anti-OCT3/4, anti-GATA4, and anti-CDX2 immunostainings were used.

A 3D UNet (Çiçek et al., 2016) was trained with a multi-task objective: predicting the binary nuclei mask in the first output channel and predicting the nuclei boundaries/outlines in the second output channel. The boundary predictions were then used to recover the individual nuclei using PlantSeg's 'MutexWS' partitioning algorithm. The nuclei foreground prediction is used in post-processing for removing spurious instances in the background.

Model training was performed iteratively with an increasing amount of ground truth data. Starting from four initial ground truth data volumes, manually annotated using the Paintera software (https://github.com/saalfeldlab/paintera), in each iteration we trained the network, performed the segmentation, and manually proofread the results in order to increase the training set and accuracy. In total, 22 training and 13 validation data volumes were used for the final model training. The size of the training volumes ranged from [117, 703, 377] to [162, 1052, 1840] voxels in X, Y, and Z dimensions.

3.7.4 Basal membrane segmentation

Segmentation of the basal membrane (BM) between EPI and PrE from the RM was performed with the segmentation editor (https://imagej.net/plugins/segmentation-editor) in Fiji based on anti-Collagen IV or anti-pan-Laminin immunostaining data. 2D Rois with the BM data signal were converted into continuous contours using a custom Python script.

3.7.5 Evaluation of embryo development by cell numbers

Cell counts for E4.5-E6.0 in utero embryos were obtained from the previous study (Ichikawa et al., 2022). Cells for E3.5 *in utero* embryos were counted based on GATA4 and SOX2 immunostaining. Linear regression analysis for embryo staging was performed as described (Ichikawa et al., 2022). For successfully developed 3E-uterus embryos, epiblast (EPI) cells were defined based on the nuclear OCT3/4 expression. Cells with nuclear GATA4 expression overlying epiblast cells were defined as visceral endoderm (VE); cells overlying ExE were not included in this analysis. OCT3/4 and GATA4 channels were individually used for automatic EPI and VE nuclei segmentation (see “Nuclei segmentation”). To provide maximal quantification accuracy, nuclei segmentation results were used either for automated cell counting after manual correction or for manual cell counting in Imaris.

3.7.6 Cell tracking

ICY (de Chaumont et al., 2012) was used for cell tracking. In brief, individual cells on the mural TE side of the H2B-GFP expressing embryos were tracked in 3D over 18-24 hours of imaging, starting from 30 hours post E3.5 recovery.

3.7.7 Image quantification

Dimension measurements and cell counting were performed with Imaris v9.2.1 (Bitplane). Fiji (Berg et al., 2019; Schindelin et al., 2012) was used for kymograph analysis, basal membrane segmentation, contact angle quantification, volume measurements, and fluorescence intensity quantification for plasma membrane proteins. Ilastik (Berg et al., 2019) was used for CDX2-GFP nuclear signal segmentation. In the figure legends, “N” corresponds to a number of replicates, “n” to number of samples within a replicate, unless otherwise stated.

3.7.7.1 Fluorescence intensity quantification for plasma membrane proteins

Identical imaging settings were applied for the samples in Figure 4.16 to enable comparison. The fluorescence signal of ZO1, PARD6B, and pERM was measured in Fiji using a line tool, 5 pixels in width, drawn along the cell's perimeter. Signal intensity values along the cell perimeter were exported for analysis and visualization in R. The signal was normalized to the average nuclear DAPI signal within the same Z plane.

3.7.7.2. Quantification of the contact angle at the embryo-hydrogel Interface

Image volumes were manually transformed with BigDataProcessor2 Fiji plugin for vertical crypt alignment along the y-axis. Images were XZ-resliced followed by 180^{o} radial reslice about the center of the line of symmetry. Microwell surface was identified based on the background hydrogel fluorescence. Fiji's Ange tool with a handle length of 15-20 µm was used to quantify the angle (θ) between the crypt surface and the cell membrane on the mural and polar TE sides. θ values were quantified on the left and right sides of the image every 30^{o}. The θ values were averaged value across the crypt circumference.

3.7.7.3 Polar TE cell shape quantification

Polar TE cell length and the width were manually measured with Imaris based on the overlay of the cell membrane segmentation output and the raw signal. The dimensions were measured for 15-20 polar TE cells per embryo every hour of live imaging.

3.7.7.4 Quantification of ExE internalization

The image volumes were drift-corrected and down-sampled 2x in all dimensions. CDX2-GFP nuclear signal was segmented with Ilastik. The displacement of the center of mass was tracked along the crypt axis (y-axis).

3.7.7.5 Embryo length quantification

Embryo length was quantified in 3D as a distance between the outermost giant trophoblast nucleus and the outermost nucleus of the polar TE/ExE along the crypt axis (Figure 3H).

3.7.7.6 Kymograph analysis

To quantify mural TE and EPI displacements, a kymograph was drawn parallel to the crypt axis and the edge of the membrane signal was tracked. Per each embryo, the values were averaged across three lines per Z-slice in three different Z locations.

3.7.7.7 Middle axis estimation and length computation

Was performed by J. Hugger from V. Ullman's group. Briefly, the binary 3D segmentation of the basal membrane (BM) between EPI and PrE was used for analysis. First, the Euclidean Distance Transform (DT) was applied to the 3D segmentation to construct a directed graph in which the nodes are the non-zero valued pixels of the DT. The edges of the graph were assigned with weights that represent the difference between the global maximum of the DT values and the DT value of the target node. The shortest path in the weighted graph was then computed between two nodes that correspond to manually annotated points on the specimen's surface that mark its extreme poles (Dijkstra, 1959). The nodes on the shortest path were used to fit an open cubic B-spline (Schoenberg, 1969) curve that approximates the middle axis. Finally, the integration over the spline was performed in order to obtain the arc-length of the egg cylinder.

4 RESULTS

Some results descriptions, figures, and figure legends were adapted from Bondarenko et al., 2022.

4.1 Establishing a new system for peri-implantation mouse embryo culture by uterine engineering and live imaging

Here, I tested several *ex vivo* approaches for supporting peri-implantation mouse embryo development.

4.1.1 2D and 3D embryo culture

First, I cultured intact mouse blastocysts in a 2D environment (Bedzhov et al., 2014). When grown on a glass surface, E.3.5 embryos underwent collapse of the blastocoel cavity and TB expansion during the second day of *ex vivo* culture (Figure 4.1A). Notably, RM integrity was not maintained after 58 h (Figure 4.1B), and EPI and PrE appeared on the embryo's surface (Figure 4.1B, yellow arrow). As a result, the egg cylinder did not form inside RM, in contradiction to how it occurs *in utero*.

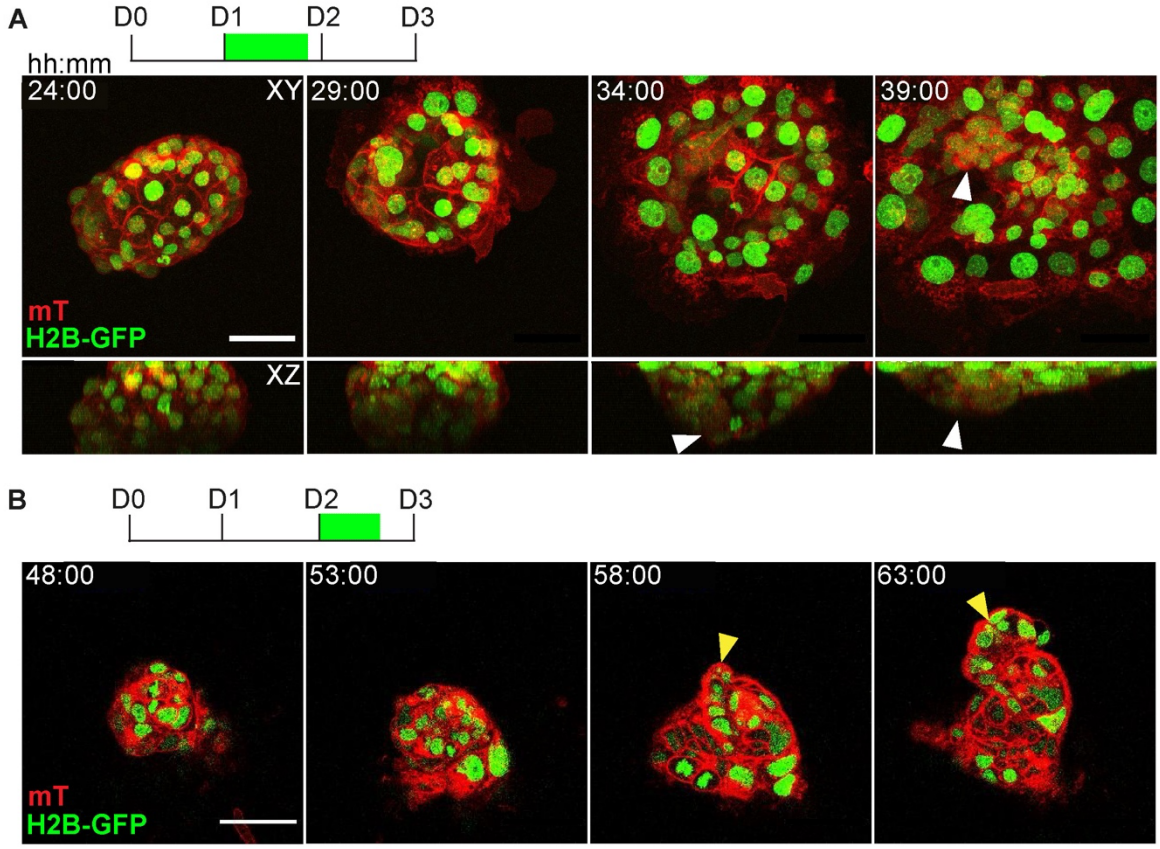

Figure 4.1. Representative time-lapse images of the H2B-GFP;mTmG embryo growing on a 2D glass surface. A, projection images along Z (top) and Y (bottom) axes. B, single-plane images. GFP (green), mTomato (red). White and yellow arrows mark blastocoel collapse and EPI outgrowth, respectively. n = 4. Scale bars, 50 μm (E, right). t =00:00, hours: minutes after recovery at E3.5.

Since the 2D environment disrupted development, I hypothesized that the 3D environment provided by the uterine ECM could improve embryo culture. To mimic ECM and provide isotropic physicochemical properties, I used chemically-synthesized biocompatible LDTM PEG (Rezakhani et al., 2020). LDTM PEG was functionalized with adhesion cues, RGD (Arg-Gly-Asp), and cross-linked via matrix metalloprotease (MMP)-cleavable peptides. This composition is further referred to as 'hydrogel'.

I used a similar approach to culture intact ZP-free E3.5 blastocysts but instead embedded them into the hydrogel drops. I then compared embryo morphology and the numbers of EPI cells per embryo between hydrogel-embedded *ex vivo* culture for up to three days and *in utero* development during the stages when the egg cylinder is formed (E5.0 – E5.25) (Figure 4.2A). The cultured embryos grew smaller and had impaired morphology (Figure 4.2B). After three days, embryos did not form elongated egg cylinders and had significantly fewer EPI cells (Figure 4.2C). These results indicate that the isotropic 3D environment blocks or significantly delays embryo growth, following previous findings in the laboratory using Matrigel/Collagen-embedded culture of the intact E4.0 – 4.5 embryos (Ichikawa et al., 2022).

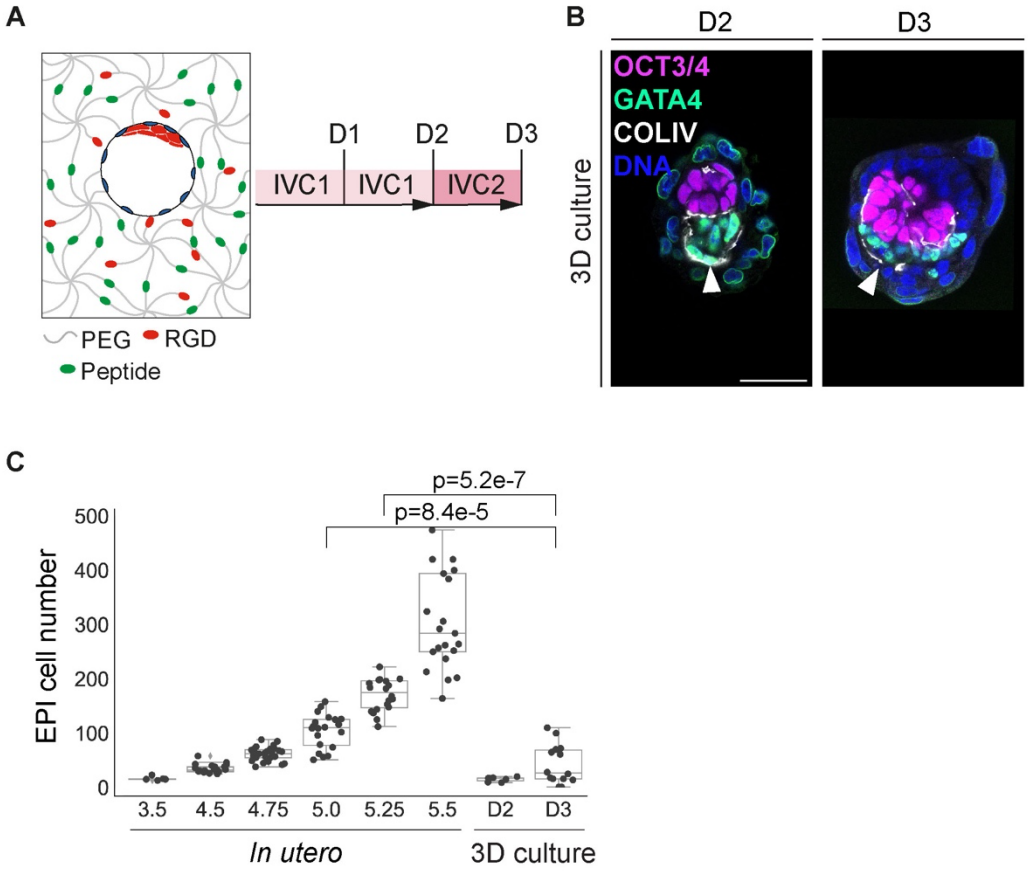

Figure 4.2. A, schematic of the experiment (see "3D hydrogel-embedded embryo culture"). The hydrogel is comprised of 8-arm Poly(ethylene glycol) (PEG, gray) molecules, connected via the metalloprotease-cleavable peptides (Peptide, green) and cross-linked with RGD (Arg-Gly-Asp, red). IVC1 and ICV2 stand for "In Vitro Culture" medium 1 and 2, respectively. Inner cell mass (ICM), red; trophectoderm (TE), blue. B, representative immunofluorescence images of the embryos embedded and cultured 3D inside hydrogel drops until day 2 (D2) and day 3 (D3), stained for OCT3/4 (magenta), GATA4 (green), and nuclei (DNA, blue). n = 7 (D2) and n = 10 (D3). C, comparison of the epiblast (EPI) cell numbers between the embryos developed *in utero* until E3.5 – E5.5 (Ichikawa et al., 2022) and the hydrogel-embedded embryos. Scale bars, 50 μm

I interpreted these results as questioning our initial assumption that the implantation occurs in the isotropic environment. Thus, I further characterized ECM deposition at the embryo implantation sites of the pregnant uteri between E4.75 and E5.25. Enrichment of all main ECM components, including fibronectin, collagen IV, and laminin, was detected around the implanted embryos (Figure 4.3A). However, the

basal membrane between the endometrium and the uterine stroma formed a crypt shape around the implanting embryo, elongated along the mesometrial/anti-mesometrial (M/AM) axis (n = 34 embryos in total) (Figure 4.3B-C). This observation was highly reproducible and also noticed in many previous studies (Burckhard, 1901; Farrar & Carson, 1992; Enders et al., 1980; Yuan et al., 2016). However, such tissue geometry's role and functional relevance have not been tested directly in the experimental setting. To address the mechanism and functional relevance of ECM tissue geometry and other biomechanical uterine tissue properties in peri-implantation development, I aimed to reconstitute them *ex vivo*.

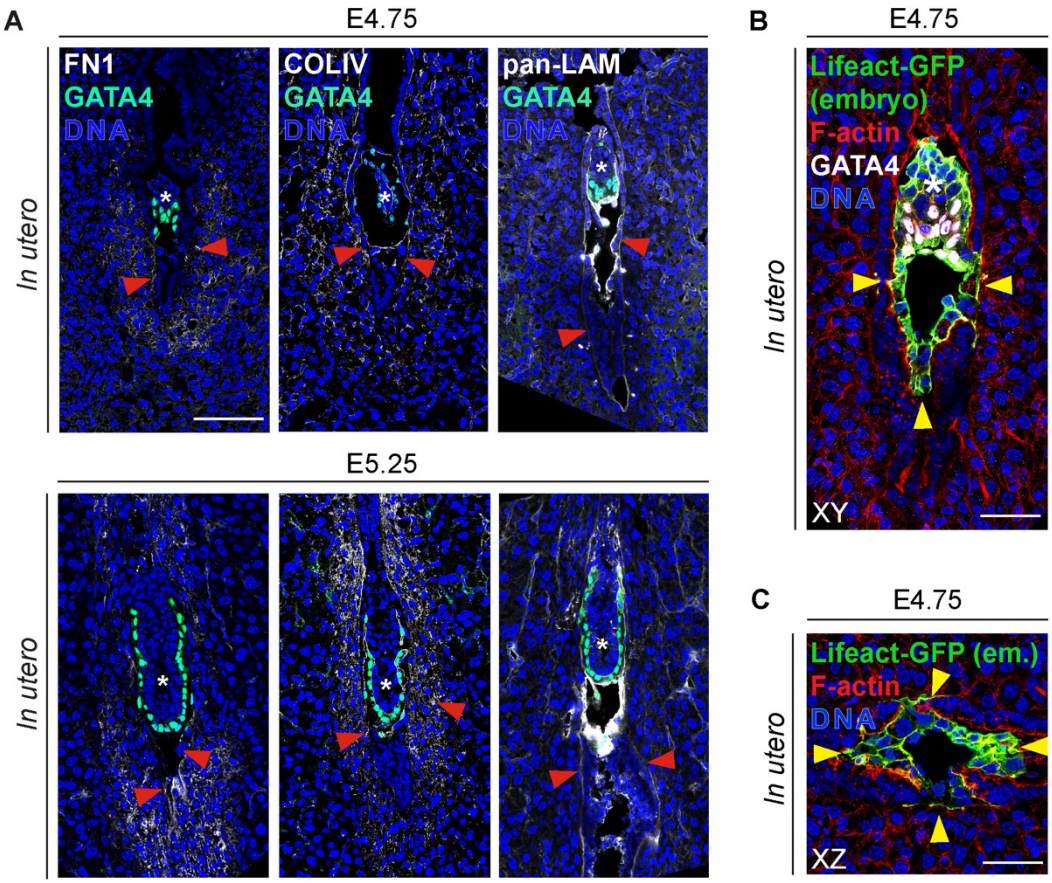

Figure 4.3. A, Immunofluorescence images of the representative E4.75 (top) and E5.25 (bottom) uteri cross-sections, stained for Fibronectin (FN1, white), Collagen IV (COLIV, white), and Laminin (LAM, white) (from left to right), GATA4 (green), and nuclei (DNA, blue). n = 20, N = 7 and n = 14, N = 5 for *in utero* E4.75 and E5.25, respectively. B, immunofluorescence image of E4.75 uterine cross-section from F1 female mated with Lifeact-GFP male; C, transverse uterine tissue section. Simultaneous staining for GFP (green), F-actin (red), GATA4 (white), nuclei (DNA, blue). White asterisks mark implanted embryos; red and yellow arrowheads point at the uterine basal membrane and the embryo perimeter within the crypt, respectively. Sectioning thickness, 20 μm. Scale bars, 50 μm.

4.1.2 Engineering *Ex vivo* uterine Environment with biomimetic hydrogel topography (3E-uterus)

In collaboration with M. Nikolaev from the Lutolf lab at EPFL, we used high-precision microfabrication strategies for a topographical 3D modification of the hydrogel surface (Gjorevsky, Nikolaev, Brown, et al., 2022). *Ex vivo* E3.5 blastocyst culture efficiency depended on the crypt dimensions, as judged by the embryo morphology criteria (Figure 4.4A, B). Embryos developed with an average of 30% efficiency in 120 – 140 μm diameter range of cylindrical crypts. (Figure 4.4B). The crypt diameter gradient was introduced to account for the blastocyst size variability (Figure 4.5A). Compared to Collagen I and conventional PEG matrices, embryo development was most efficient using the Low-Defect Thiol-Michael Addition (LDTM) PEG, in line with its high efficiency for organoid development (Rezakhani et al., 2020).

The synthetic LDTM PEG matrix allowed testing of other parameters, such as stiffness, which is linearly proportional to the PEG precursor content (Figure 4.5B, inset). I applied PEG precursor content between 1.5% and 7%, corresponding to a nearly 10-fold range of the shear moduli (Figure 4.5B). The highest efficiency of embryo culture was for 1.5-2 % PEG, corresponding to 100-300 Pa shear modulus (Figure 4.5B, C). Interestingly, this stiffness range is comparable to the stiffness of the E5.5 mouse decidua (Govindasamy et al., 2021).

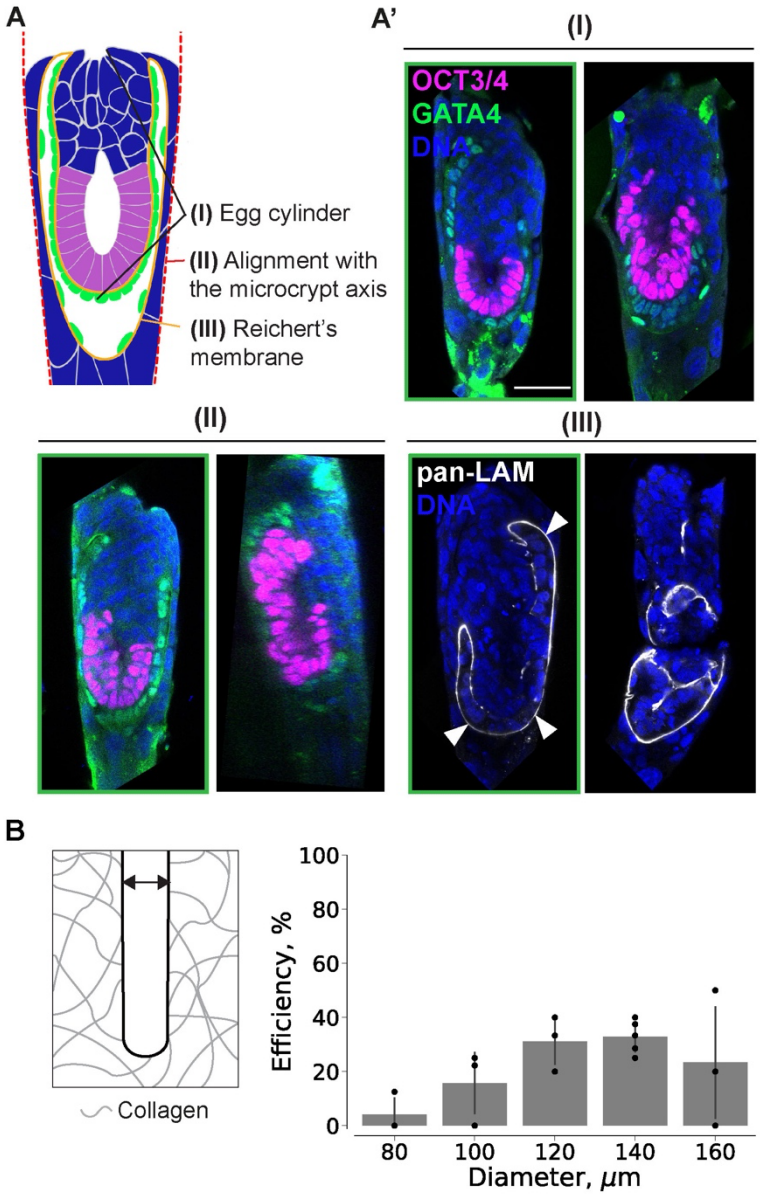

Figure 4.4. A, schematic of the embryo morphology criteria (I-III), based on which efficiency of the *ex vivo* culture is evaluated. A', representative immunofluorescence images of the embryos after 3E-uterus culture for 3 days. Immunostaining for OCT3/4 (magenta), GATA4 (green), Laminin (LAM, white), and nuclei (DNA, blue). The embryos that form egg cylinder (I), show the egg cylinder axis in line with the crypt axis (II), and form Reichert's membrane (III), are considered to be successfully developed (outlined in green). B, barplots, showing average 3E-uterus efficiency for culture inside cylindrical crypts with different diameters. n = 1/17, N = 3 (80 μm); n = 4/20, N = 3 (100 μm); n = 4/13, N = 3 (120 μm); n = 9/27), N = 3 (140 μm); n = 3/14, N = 3 (160 μm). Dots correspond to efficiency values in experimental replicates (N), whiskers indicate standard deviations. See Methods "Evaluation of 3E-uterus efficiency".

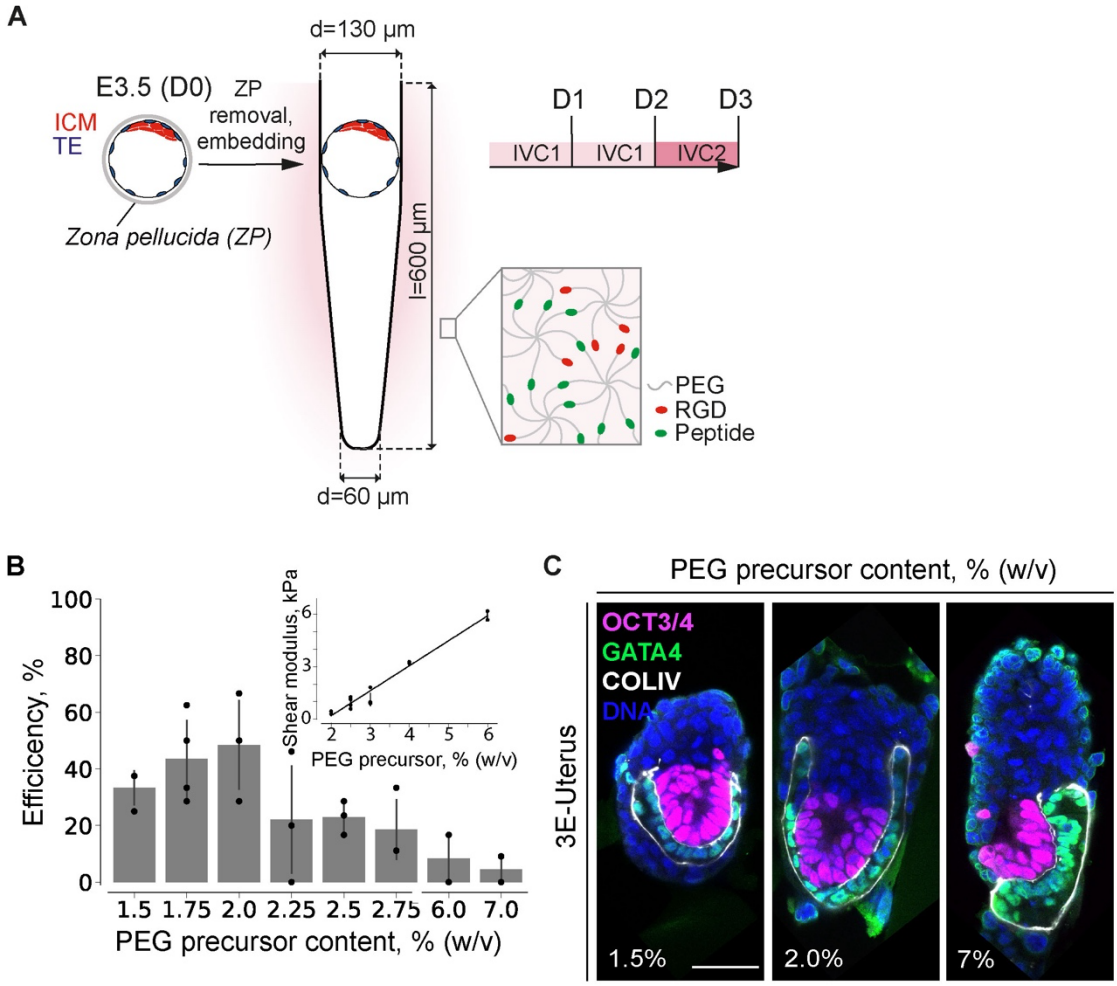

Figure 4.5 A, schematic for peri-implantation embryo culture using biomimetic hydrogel topography. B, Barplots showing 3E-uterus efficiency at day 3 at various PEG precursor contents. n = 25, N = 3 (1.5%); n = 33, N = 4 (1.75%); n = 19, N = 3 (2%); n = 24, N = 3 (2.25%); n = 33, N = 3 (2.5%); n = 32, N = 3 (2.75%); n = 21, N = 3 (6%); n = 17, N = 2 (7%). Dots correspond to efficiency values for experimental replicates (N), whiskers indicate standard deviations. Inset, rheological measurement showing linear relationship between the PEG precursor content (%, w/v) and the Shear modulus (kPa). C, representative immunofluorescence images of the 3E-uterus embryos from day 3 (D3) grown in 1.5%, 2%, 2.5%, and 7% PEG precursor concentrations (from left to right), stained for OCT3/4 (magenta), GATA4 (green), Collagen IV (COLIV, white), and nuclei (DNA, blue).

To quantitatively evaluate egg cylinder growth, I compared the numbers of EPI and VE cells, based on automatic nuclei segmentation, during three days of 3E-uterus embryo culture and E3.5 – E5.5 *in utero* embryo development. Cell proliferation progressed during *ex vivo* embryo culture (Figure 4.6A), showing no significant

difference in the number of EPI cells between 3E-uterus embryos successfully developed until day 3 and the embryos developed *in utero* until E5.25 (Figure 4.6B). Morphology of the 3E-uterus embryos at day 3 closely resembled morphology of the *in utero* embryos at E5.25, confirming that 3E-uterus supports egg cylinder formation (Figure 4.6C, D).

I also introduced additional measurements to evaluate egg cylinder size. Based on the 3D segmentation of the basal membrane underneath PrE spanning EPI and ExE, with the help of J. Hugger from V. Ullman group, I computed the length, diameter, and length-to-diameter ratio of the egg cylinder (Figure 4.6E). Although 3E-uterus embryos are significantly shorter than their counterparts developed *in utero*, the difference in the diameter and the length-to-diameter ratio was insignificant, indicating that, on average, *in utero* egg cylinder proportions are maintained *ex vivo*. I then matched the developmental timescales of 3E-uterus and *in utero* embryo development (Figure 4.6F). Collectively, this quantitative analysis shows that 3E-uterus reproduces *in utero* E5.25 egg cylinder morphology with an average of 46% efficiency by day 3.

Laminin-rich Reichert's membrane, continuously connected to the basal membrane of the egg cylinder, formed in 77% of the 3E-uterus embryos (n = 20 of 26 embryos, three independent replicates pooled) (Figure 4.7A). In these embryos, the inner side of the RM contained GATA4-positive cells, corresponding to PE. On the outer side of the RM, TB cells, marked by the expression of TFAP2C and KRT8 (Jaquemar et al., 2003; Latos et al., 2015), surrounded the egg cylinder structure. Giant trophoblast (GT) cells with exceptionally large – sometimes multiple – nuclei were predominantly located at the embryo apex, both *in utero* and *ex vivo* (Figure 4.7A). Altogether, these results indicate that 3E-uterus supports early morphogenesis of embryonic and extraembryonic tissues, closely recapitulating *in utero* peri-implantation embryo development.

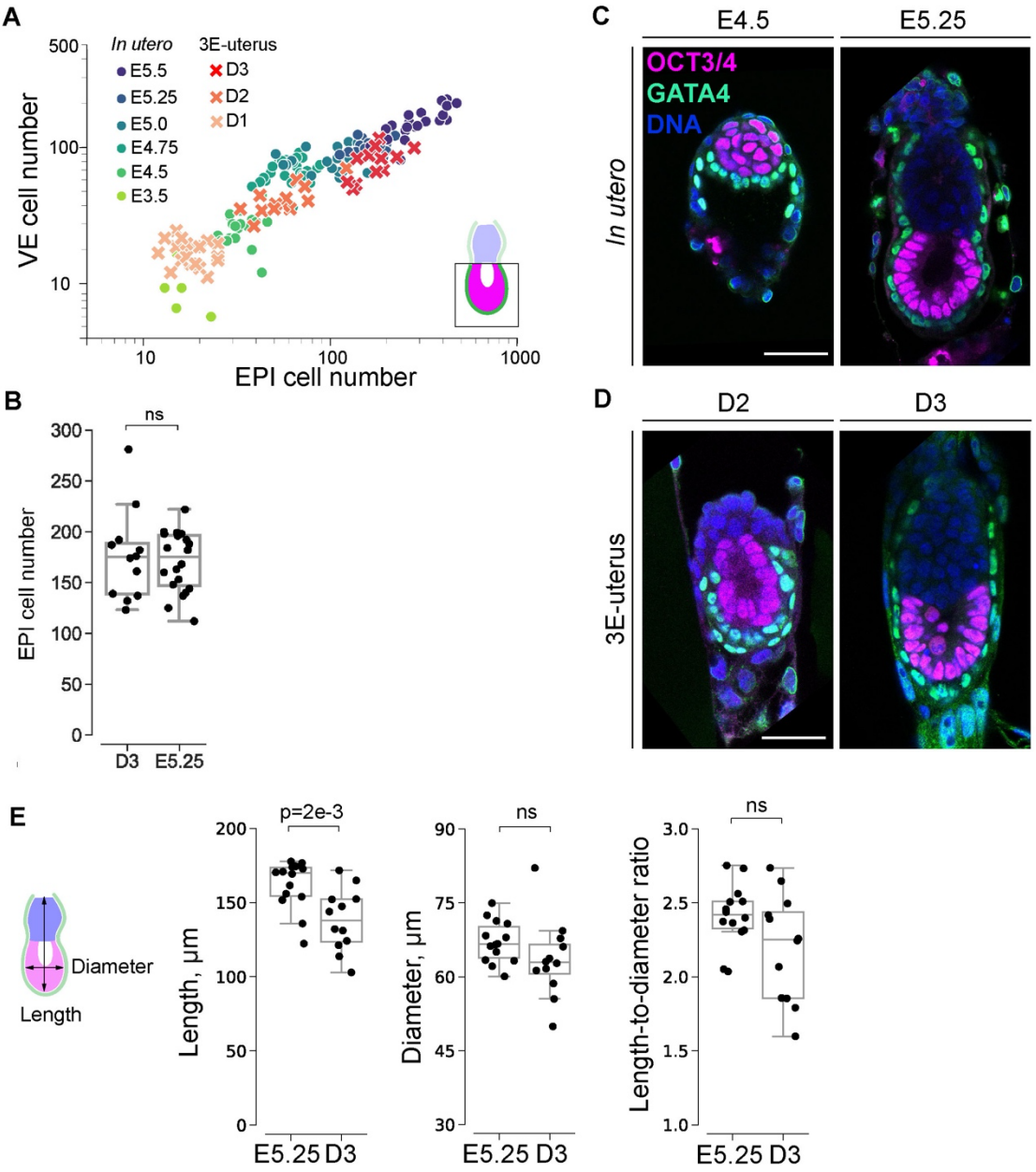
A
In utero
3E-uterus
E5.5
E5.25
E5.0
E4.75
E4.5
E3.5
D3
D2
D1
VE cell number
EPI cell number
B
ns
EPI cell number
D3
E5.25
C
E4.5
E5.25
OCT3/4
GATA4
DNA
In utero
D
D2
D3
3E-uterus
E
Diameter
Length
p=2e-3
ns
ns
Length, µm
Diameter, µm
Length-to-diameter ratio
E5.25 D3
F
In utero
E3.5
E4.5
E5.25 E5.5
D0
D1
D2
D3
3E-uterus

Figure 4.6 A, scatterplot showing numbers of epiblast (EPI) cells (x-axis) vs numbers of visceral endoderm (VE) cells (y-axis) that cover EPI in the embryos developed *in utero* until E5.5 (E3.5 – E5.5) and the embryos developed by 3E-uterus until day 3 (D1 – 3). n = 5 (E3.5), n = 21 (E4.5), 28 (E4.75), 20 (E5.0), 20 (E5.25), 21 (E5.5), data from (Ichikawa et al., 2022); n = 20, 2 replicates pooled (D1), n = 13 out of 28, 3 replicates pooled (D2), n = 12 out of 26, 3 replicates pooled (D3). X/Y scale, log 10. Bottom right, the scheme of the quantified embryo region, EPI (magenta), VE (green). B, boxplots showing the numbers of epiblast cells in 3E-uterus embryos from day 3 (D3) and embryos developed *in utero* until E5.25 (n = 12 and 17, respectively). P-value was calculated using Mann-Whitney U test. C, representative immunofluorescence images of the embryos developed *in utero* until E4.5 and E5.25, simultaneously stained for OCT3/4 (magenta), GATA4 (green), and nuclei (DAPI, blue). n = 6 (E4.5), 17 (E.5.25). D, representative immunofluorescence images of the 3E-uterus embryos from day 2 and 3, simultaneously stained for OCT3/4 (magenta), GATA4 (green), and nuclei (DAPI, blue). E, from left to right, boxplots showing egg cylinder's length, diameter, and the length-to-diameter ratio between embryos developed *in utero* until E5.25 and 3E-uterus embryos from day 3 (D3). n = 14, N = 3; n = 12, N = 3, respectively. Data points, shown as black dots, correspond to individual embryos, midline marks the median, boxes indicate interquartile range. P-values were calculated using Student's t-test and the Mann-Whitney U test. F, cell number-based correspondence between *in utero* and 3E-uterus embryo development.

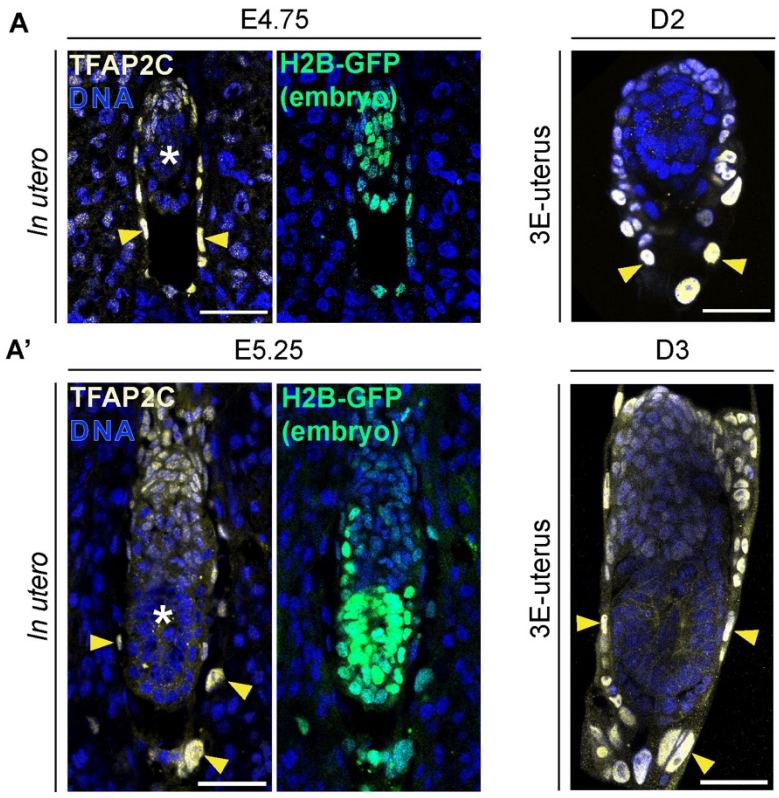

Figure 4.7 A, left, representative immunofluorescence image of the E4.75 uterus cross-section from the pregnant F1 female mated with the H2B-GFP male. Simultaneous immunostaining for TFAP2C (yellow), GFP (green), and nuclei (DNA, blue). n = 4, N = 2. Right, immunostaining of the 3E-uterus embryo from day 2 (D2). n = 15, N = 2. A', left, representative immunofluorescence image of the E5.25 uterus cross-section from the F1 female mated with the H2B-GFP male. Simultaneous immunostaining for TFAP2C (yellow), GFP (green), and nuclei (DNA, blue). n = 8, N = 2. Right, immunostaining of the 3E-uterus embryo from day 3 (D3). n = 10, N = 2.

4.1.3 Uterine matrix geometry and adhesion to it are necessary for embryogenesis

The advantage of synthetic matrices is that they allow decoupling of different parameters and testing them independently. My experimental results and *in utero* observations indicate that uterine ECM geometry is necessary for development. However, it remains possible that the geometry alone is sufficient, and the ECM does not have a mechanistic relevance. To decouple geometry and adhesion, I cultured embryos side-by-side in the crypts made of hydrogel with RGD, without RGD, and with

the same geometry. Interestingly, the developmental efficiency significantly dropped without RGD (Figure 4.8A, B): the embryos did not develop an egg cylinder, except for one experiment in which a single outlier embryo formed an egg-cylinder-like structure inside RM (Figure 4.8B). These results suggest that integrin-mediated adhesion and uterine geometry are both necessary for peri-implantation mouse development. Indeed, the integrin beta 1 (ITGB1) subunit and its active form are enriched at the basal as well as the apical sides of the mTE/TB cells that directly interact with the uterine wall *in utero* (Figure 4.8C; Sutherland, 1993; Govindasamy et al., 2021), whereas in E3.5 blastocysts ITGB1 is still located basally (Figure 4.8D; Kim et al., 2022).

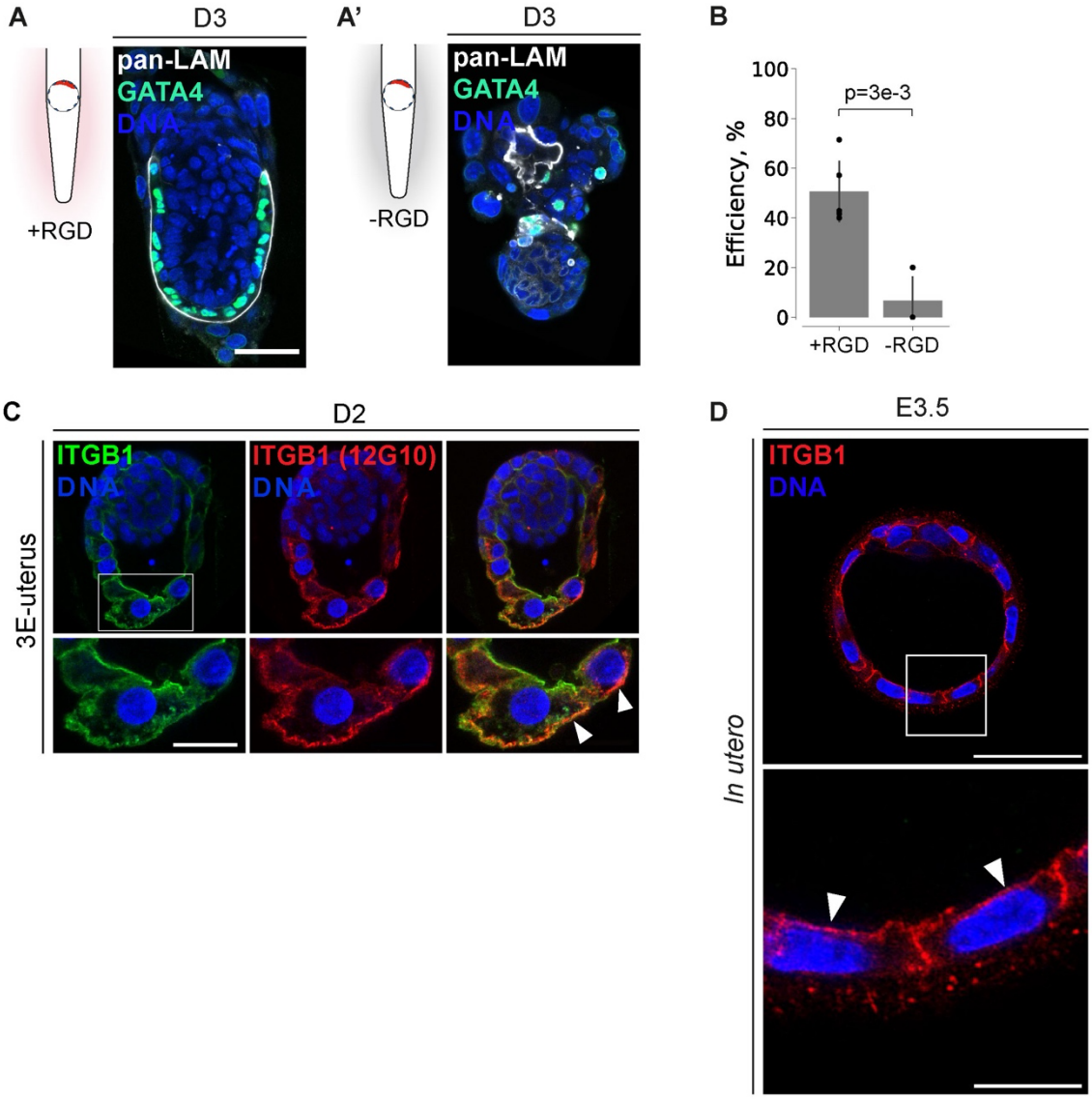

Figure 4.8. A, representative immunofluorescence image of the embryo cultured in the crypts made of PEG with RGD for 3 days and stained for pan-Laminin (pan-LAM, white), GATA4 (green), and nuclei (DNA, blue); n = 12, N = 2. A', representative immunofluorescence image of the embryo cultured in the crypts made of PEG without RGD for 3 days and stained for pan-Laminin (pan-LAM, white), GATA4 (green), and nuclei (DNA, blue); n = 10, N = 2. B, barplots showing 3E-uterus developmental efficiency with and without RGD; n = 34 from N = 5 in total; n = 25 from N = 3 in total, respectively. Dots correspond to efficiency values in experimental replicates (N), whiskers indicate standard deviations. P-values were calculated using Student's t-test. C, representative immunofluorescence image of the embryos cultured in the crypts made of PEG with RGD for 2 days, simultaneously stained for total integrin beta 1 (ITGB1, green), active ITGB1 (12G10, red), and nuclei (DNA, blue). n = 7. From left to right, total ITGB1, active ITGB1, composite image channels. Bottom, 2x zoom. D, representative immunofluorescence image of the blastocyst-stage embryo (E3.5), simultaneously stained for integrin beta 1 (ITGB1, red), and nuclei (DAPI, blue). n = 5. Bottom, 4x zoom. Arrowheads point to the basal integrin localization in TE.

4.1.4 Live imaging *in toto* peri-implantation embryo morphogenesis

To monitor *in toto* dynamics of the developing peri-implantation embryo at the single-cell resolution, we integrated 3E-uterus with the multi-view light-sheet microscopy (MuVi-SPIM) (Krzic et al., 2012) (Figure 4.9A). MuVi-SPIM addresses the imaging depth limitation and anisotropic sampling by recording the specimen from several angles (Krzic et al., 2012). The second opposing illumination and detection lens pair and simultaneous recording increase the acquisition time by four and reduce the illumination light dosage by two compared to single-view light-sheet systems (Power & Huisken, 2017; Kromm et al., 2016), making it ideal for volumetric live imaging of the samples such as gastrulating mouse embryos (McDole et al., 2018). To support long-term embryo viability, together with D. Kromm, we implemented atmospheric and temperature regulation of the MuVi-SPIM imaging chamber (Figure 4.9A). We also developed a new engineering approach to precisely position the embryo within the hydrogel microenvironment (Figure 4.9B). Our design prevented the embryo from exchanging liquid with the rest of the imaging chamber, providing sterility and efficient usage of the culture medium.

According to the *in utero*-matched 3E-uterus time scale, the morphological transition of E4.25 blastocyst to E4.75 peri-implantation embryo is predicted between day 1 and mid-day 2 (Figure 4.6F). I performed live imaging of H2B-GFP;mTmG

(Hadjantonakis & Papaioannou, 2004; Muzumdar et al., 2007) transgenic embryos with GFP and mTomato channels every 15 min for 24 h starting from 32 h (Figure 4.9C) and with an overlapping time interval of 6 h, between day 2 and day 3 of 3E-uterus every 20 min (Figure 4.9D). Proamniotic lumen rosettes formed in the proliferating EPI (Figure 4.9D, yellow arrows), indicating early EPI/ExE egg cylinder patterning (Christodoulou et al., 2018; Ichikawa et al., 2022). The egg cylinder elongated along the M/AM axis at the rate of 5.52 μm/h, and the tip of the egg cylinder moved 4.62 μm /h (Figure 4.9D, 4.10A). EPI cell lineage tracks gave an estimated cell-cycle length of 8:38 hh: min (Figure 4.10B), and on average, EPI tissue volume increased 1.78x over 8 hours (Figure 4.10C). The imaging conditions did not significantly affect the embryo morphology, as judged by the quantitative evaluation of the numbers of EPI and VE cells in embryos after the live imaging (Figure 4.11A, B).

Altogether, the combined approach of hydrogel microengineering and multi-view light-sheet imaging enables studying the dynamics of embryonic and extraembryonic tissues of the whole embryo at the single-cell resolution. With these tools established, I next aimed to address the mechanisms of peri-implantation embryo development.

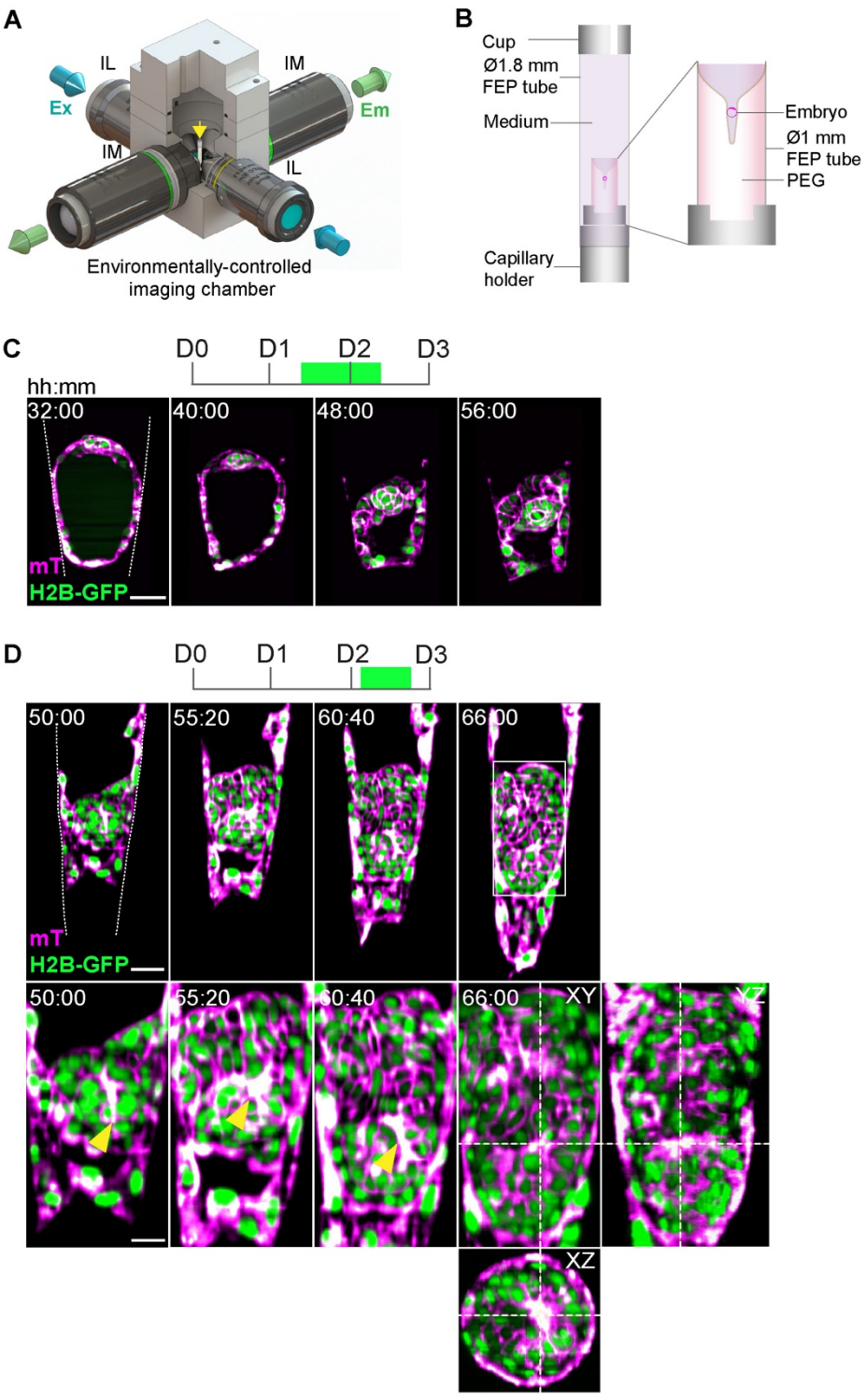
A
IL
IM
Ex
Em
IM
IL
Environmentally-controlled
imaging chamber
B
Cup
Ø1.8 mm
FEP tube
Medium
Capillary
holder
Embryo
Ø1 mm
FEP tube
PEG
C
D0
D1
D2
D3
hh:mm
32:00
40:00
48:00
56:00
mT
H2B-GFP
D
D0
D1
D2
D3
50:00
55:20
60:40
66:00
mT
H2B-GFP
50:00
55:20
60:40
66:00
XY
YZ
XZ

Figure 4.9. A, schematic of the MuVi-SPIM set-up with two low-NA illumination objective lenses (IL), two high-NA imaging objective lenses (IM), and the environmentally-controlled imaging chamber with the sample holder (yellow arrow). B, Schematic of the sample holder. The outer FEP tube (∅1.8 mm, l=25 mm) is mounted on top of the sealed glass capillary and filled with IVC medium. The inner FEP tube (∅1mm, l=3mm) contains the crypt and is supported by the PDMS holder at the bottom. The embryo is mounted from the top. The outer FEP tube is closed with the PDMS cup with ∅0.6 mm opening for the gas exchange. C, representative time-lapse images of the H2B-GFP;mTmG developing embryo. N = 2. D, Representative single-plane time-lapse images of the H2B-GFP;mTmG developing embryo. N = 3. Bottom, 2x zoom into the epiblast region. Right, YZ and XZ image sections, showing 3D resolution. GFP (green), mTomato (magenta). The crypt surface is outlined. Yellow arrow marks the proamniotic rosette.

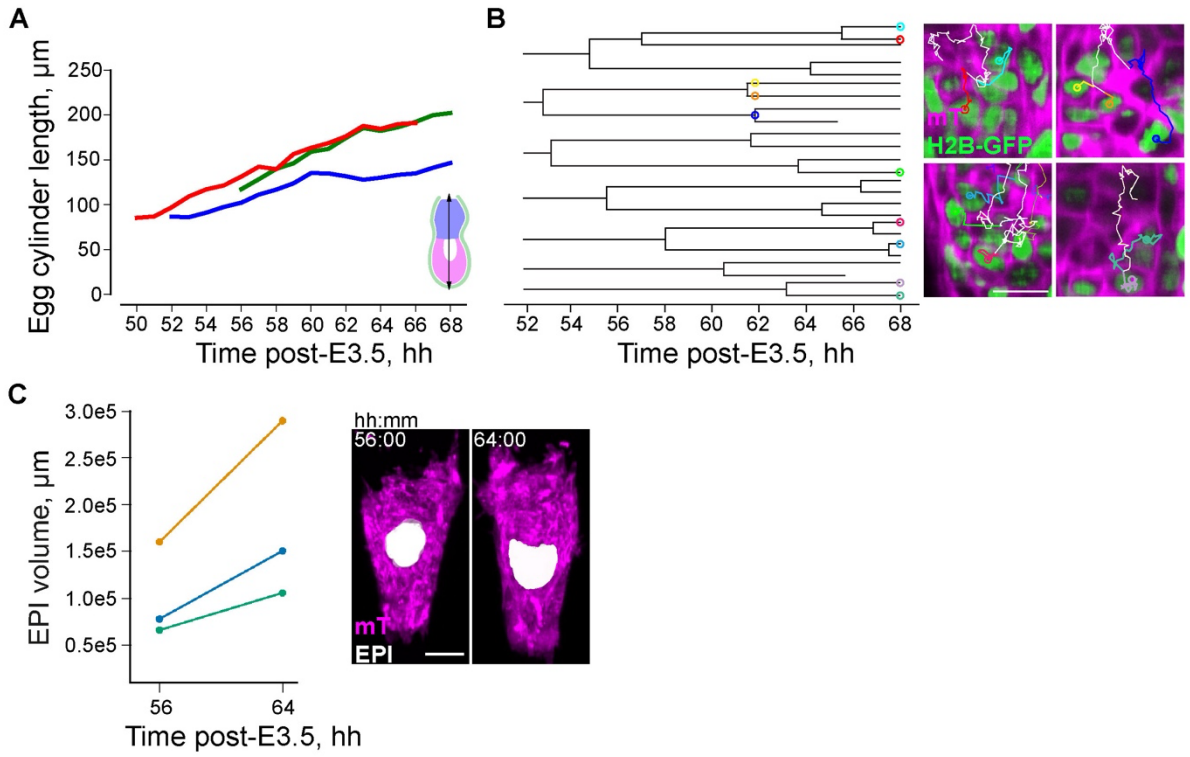

Figure 4.10 A, egg cylinder length dynamics between 50 h and 68 h after recovery at E3.5. Colors correspond to independent experiments. N = 3. B, epiblast cell lineage dendrograms. Right, corresponding cells marked as dots with different colors overlaying the dendrograms and the image slices; cell lineage tracks are depicted as a 2D overlay. C, epiblast volume increase between 56 h and 64 h post-E3.5. Colors correspond to different embryos. Right, 3D image of the developing embryo with segmented EPI volume; mTomato (magenta), EPI segmentation (white). N = 3. Scale bars, 50 µm, 25 µm (C, bottom), 20 µm (E, right). t =00:00, hours: minutes after recovery at E3.5.

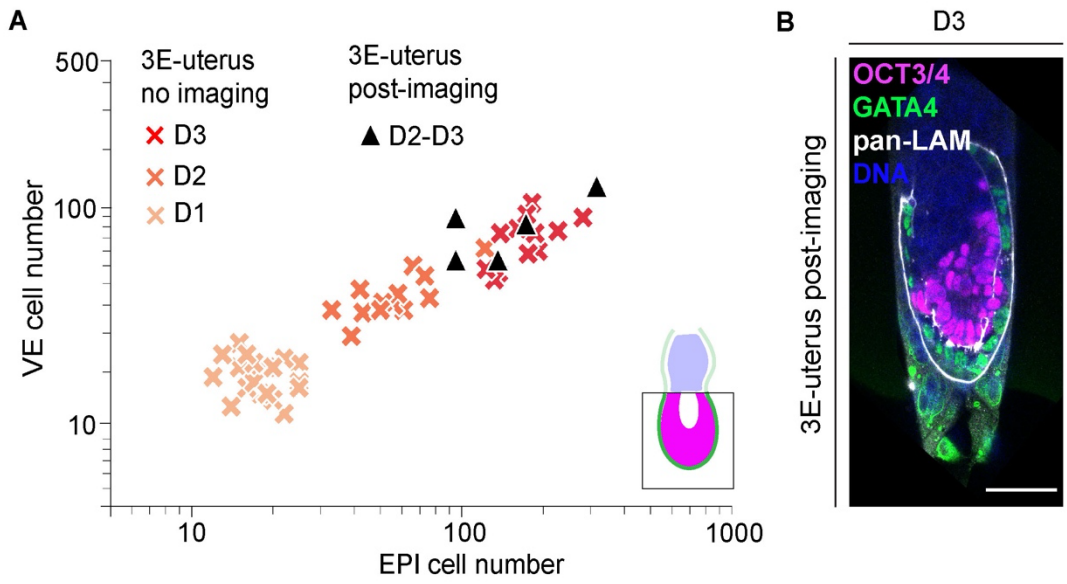

Figure 4.11 A, scatterplot showing the numbers of epiblast (EPI) cells (x-axis) vs the numbers of visceral endoderm (VE) cells (y-axis) that cover EPI in the 3E-uterus embryos developed in the incubator for three days (D1-D3, no imaging), and 3E-uterus embryos developed in the incubator, but then live imaged with MuVi-SPIM for 20 – 24 hours up to day 3 (D3, after imaging). n = 12, pooled from N = 3 (D3, no imaging), n = 5, pooled from N = 5 (D3, after imaging). The groups of imaged and not imaged D3 embryos did not significantly differ in terms of EPI (P = 0.69) and VE (P=0.37) cell numbers. P-values were calculated using t-test. XY scale, log 10. B, representative immunofluorescence image of the day 3 embryo after live imaging with MuVi-SPIM. Staining for OCT3/4 (magenta), GATA4 (green), pan-Laminin (pan-LAM, white), and nuclei (DNA, blue). Scale bars, 50 μm.

4.2 The mechanism of coordination between embryonic, extraembryonic, and uterine tissues upon implantation

4.2.1 Adhesion-mediated embryo-uterine reaction triggers extraembryonic ectoderm formation and embryo patterning

Using established live imaging, I then analyzed TE cell dynamics during egg cylinder formation. Live imaging CDX2-GFP;mTmG (McDole & Zheng, 2012) transgenic embryos between day 2 and day 3 marked an invagination of the pTE cells with nuclear GPF (Figure 4.12A, B), accompanied by a linear increase of their cell number over time (Figure 4.12C). The quantification of the pTE width-to-height cell aspect ratio indicated that pTE cells undergo apical constriction (Figure 4.12D).

Apical constriction requires the release of tension acting on TE, which can be achieved *ex vivo* via ablation of mTE (Ichikawa et al., 2022; Bedzhov et al., 2014). However, it remains unclear how the TE tension can be released *in utero* with intact mTE.

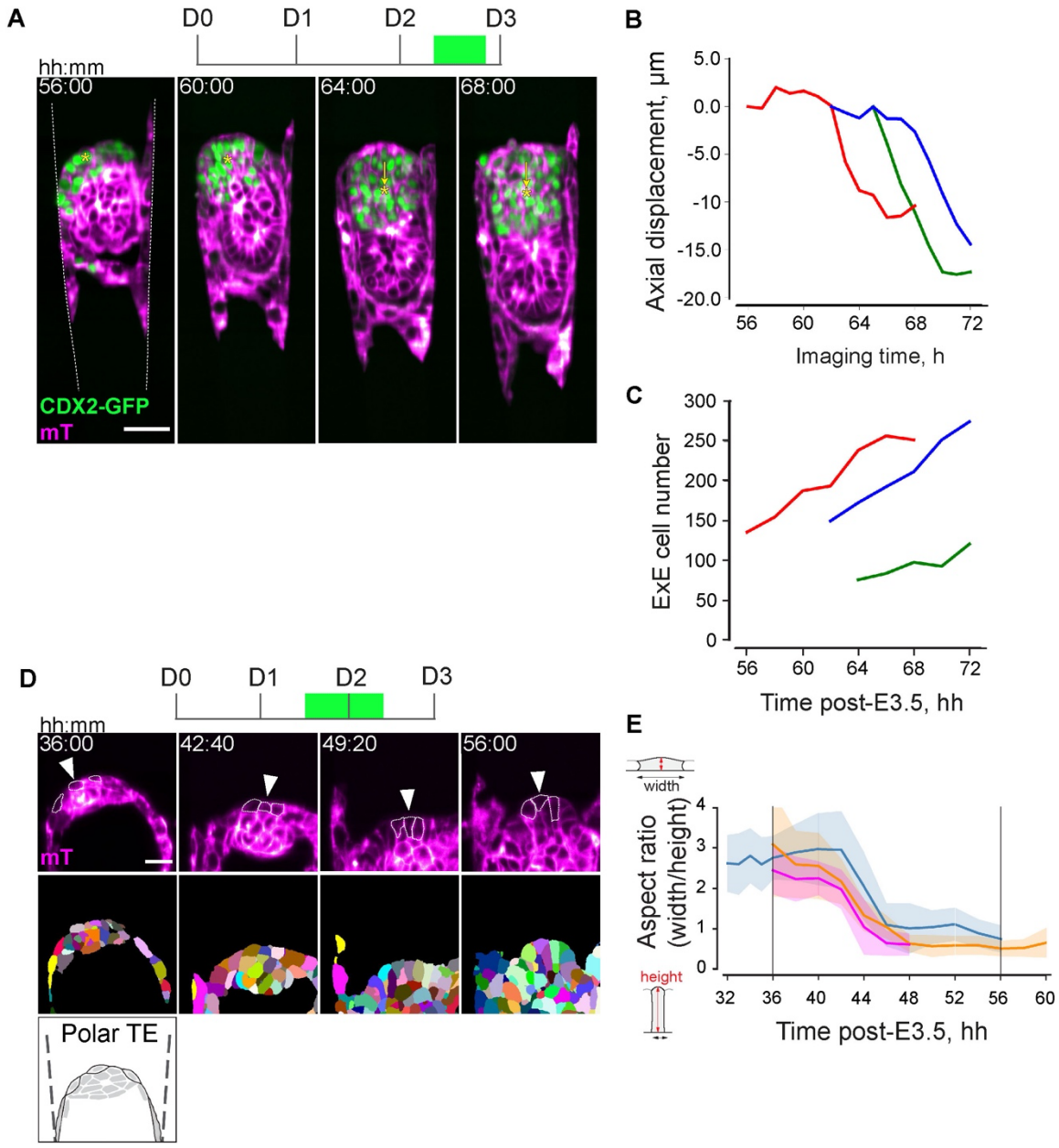

Figure 4.12. A, representative single-plane time-lapse images of the CDX2-GFP;mTmG developing embryo; GFP (green), mTomato (magenta). Yellow asterisk and an arrow mark the center of mass of the ExE and its displacement, respectively. B, displacement of the ExE center of mass along the Y-axis during live imaging. C, Quantification of the ExE cell numbers during live imaging. Colors correspond to different embryos. D, top, representative single-plane time-lapse images of the pTE of mTmG developing embryo; mTomato (magenta). Bottom, corresponding images of the 3D cell membrane segmentation. Exemplar pTE cells are marked with arrowheads, cell perimeter is outlined. E, dynamics of the width-to-height aspect ratio of the pTE cells. Colors correspond to independent experiments. Average values across 15-20 cells per time point (solid line) and standard deviations (shaded area) are shown; N = 3 for all panels.

Observing mTE dynamics, we noted distinct changes in the position and contact angle of the embryo in relation to the 3E-uterus surface (Figure 4.13A). In addition to my findings on the enrichment of apical integrins in TB cells (Figure 4.8C) this prompted to hypothesize that an active adaptation of embryo-uterus adhesion may explain the observed evolution of the embryo and cell shape as described by the physics of a droplet wetting process.

In collaboration with R. Belousov in A. Erzberger's group at EMBL, we developed a model a fluid droplet, which represents the whole embryo, in a confined conical frustum shape (Figure 4.13B). The droplet has different interfacial tensions with the substrate γ_{Δ} and the medium γ_{ME}, and is subject to a Laplace pressure ΔP that acts as a Lagrange multiplier to the droplet volume V (Bondarenko et al., 2022). This model predicts a relationship between the interfacial tensions, contact points, and contact angles between the droplet (embryo) and the substrate (uterus), given the volume of a droplet (embryo) measured from live imaging (Figure 4.13C) (Bondarenko et al., 2022).

Experimental measurement of the contact angle between the embryo and the 3E-uterus surface showed a remarkable agreement with the predicted values for increasing adhesion (Figure 4.13D-F) (Bondarenko et al., 2022). This suggests that the tissue-level shape dynamics resulting from embryo implantation can be biophysically understood as an active wetting process (Bondarenko et al., 2022). This model further predicts that failure to adhere to the uterus should lead to a near-spherical embryo shapes (Figure 4.13D), which does not contradict embryo failure phenotype in the hydrogel without RGD modification (see Figure 4.8A) (Bondarenko et al., 2022).

Collectively, these findings show that the embryo-uterus tissue-level interaction upon implantation can be biophysically described as a droplet-wetting process and that this embryo-uterus interaction releases tension acting on the TE, enabling ExE formation (Bondarenko et al., 2022).

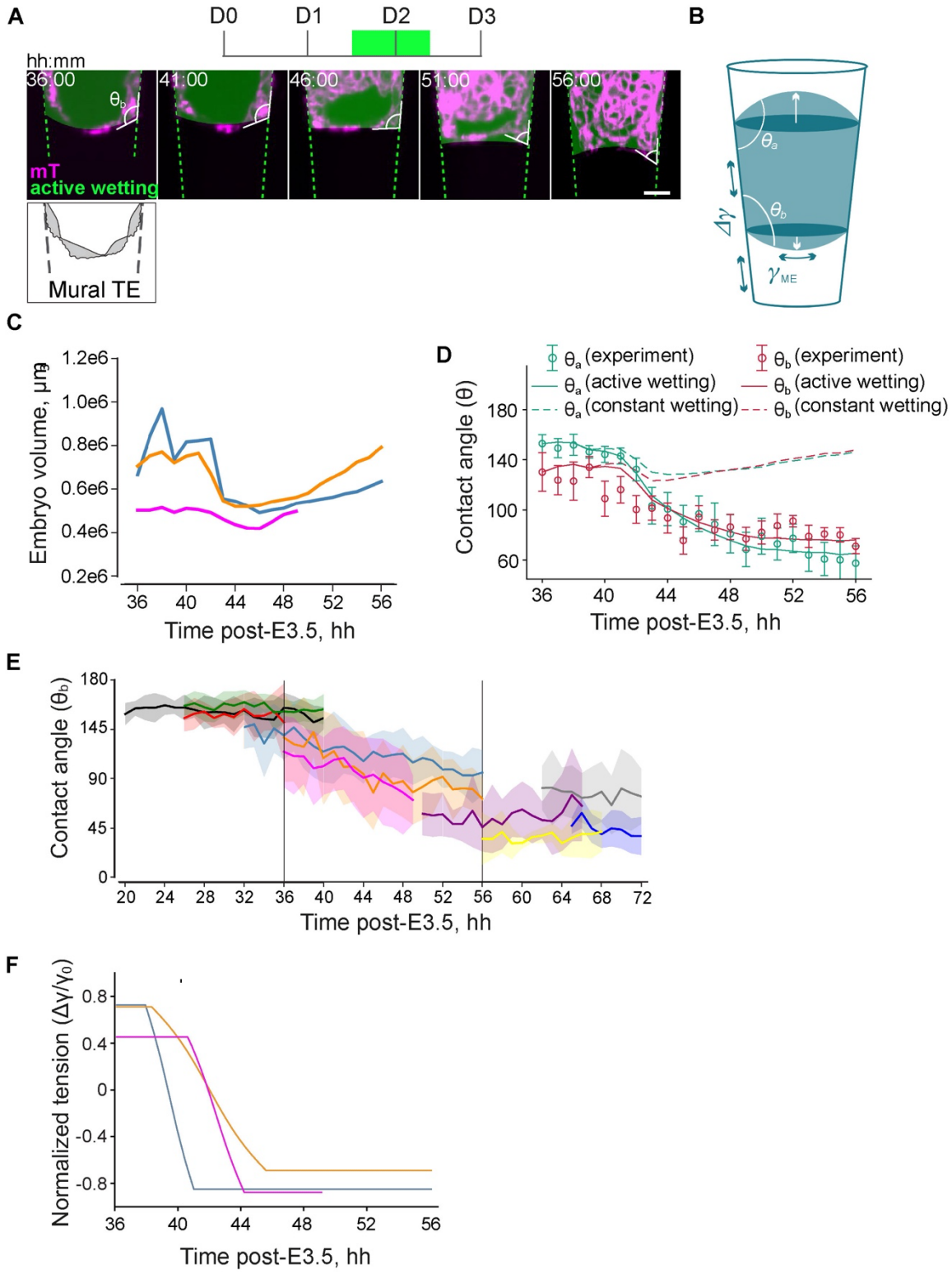
A
D0
D1
D2
D3
hh:mm
36:00
41:00
46:00
51:00
56:00
θb
mT
active wetting
Mural TE
B
θa
θb
Δγ
γME
C
Embryo volume, μm3
1.2e6
1.0e6
0.8e6
0.6e6
0.4e6
0.2e6
36
40
44
48
52
56
Time post-E3.5, hh
D
θa (experiment)
θb (experiment)
θa (active wetting)
θb (active wetting)
θa (constant wetting)
θb (constant wetting)
Contact angle (θ)
180
140
100
60
36
40
44
48
52
56
Time post-E3.5, hh
E
Contact angle (θb)
180
145
90
45
0
20
24
28
32
36
40
44
48
52
56
60
64
68
72
Time post-E3.5, hh
F
Normalized tension (Δγ/γ0)
0.8
0.4
0
-0.4
-0.8
36
40
44
48
52
56
Time post-E3.5, hh

Figure 4.13. A, representative time-lapse images of the mural TE of the mTmG developing embryo; mTomato (magenta). Fitted droplet model (embryo) and the frustum shape (crypt) shown in green; contact angle (θ) between mural TE/culture medium and mural TE/crypt interfaces is shown. B, the schematic of the model of active droplet wetting in the frustum shape. Interfacial tension with the substrate γ_{Δ} and the medium γ_{ME} are show as green arrows, θ_a and θ_b indicate top and bottom contact angles, respectively; white arrows mark the top and bottom radii. C, volume dynamics in the developing embryos between 36 h and 56 h after E3.5. Colors correspond to different embryos. N = 3. D, prediction of contact angle dynamics for a constant Young tension (dashed line) and active wetting (solid line), and experimental validation (green and red data points for θ_a and θ_b, respectively) for the embryo developing between 36 h and 56 h from recovery at E3.5. E, contact angle (θ_b) dynamics in developing embryos. Colors correspond to different embryos imaged in time intervals between 20 h and 72 h after E3.5. N = 10. F, dynamics of the normalized embryo-substrate interfacial tension difference. Colors correspond to different embryos. N = 3. Panels A, B, D, F made by R. Belousov and A. Erzberger.

4.2.2 Trophoblast cells adhesion to the uterine matrix triggers their collective migration

To further quantitatively assess mTE/TB dynamics at the cellular level, I focused on the early stages of development, when the embryo-uterine reactions establish. To this end, I integrated 3E-uterus with the Inverted View Selective Plane Illumination Microscope (InVi-SPIM) (Figure 4.14A) (Strnad et al., 2016) and monitored multiple embryos simultaneously. Tracking mTE/TB nuclei labeled with H2B-GFP (Hadjantonakis & Papaioannou, 2004) revealed cell migration (Figure 4.14B). mTE/TB cell trajectories were aligned, suggesting that their migration is collective and directional (Figure 4.14C). Notably, an average nuclei division ratio of 0.134 divisions/initial nuclei number/24 hours suggests a minor contribution of cell divisions to the observed displacement of the TB.

To address the *in utero* relevance of the finding that the TB undergoes collective migration *ex vivo*, I systematically examined TB cells in their native uterine tissue context throughout implantation. To distinguish embryos in the pregnant uterus, I crossed lifeact-GFP (Riedl et al., 2010) transgenic males with F1 females. Starting from E4.75, actin-rich cell membrane protrusions into the uterine tissue formed at the abembryonic pole of the embryo (Figure 4.15A). The data suggest that TB migration

progressed along the M/AM axis by E5.0, and TB established lateral cell protrusions (Figure 15A). At E5.25, the TB protrusions formed, both along the M/AM axis (26.9±8.6 μm) and laterally into the decidua (17.9±5.9 μm) (Figure 15A, right). Altogether, these results indicate that integrin-mediated adhesion leads to collective TB migration.

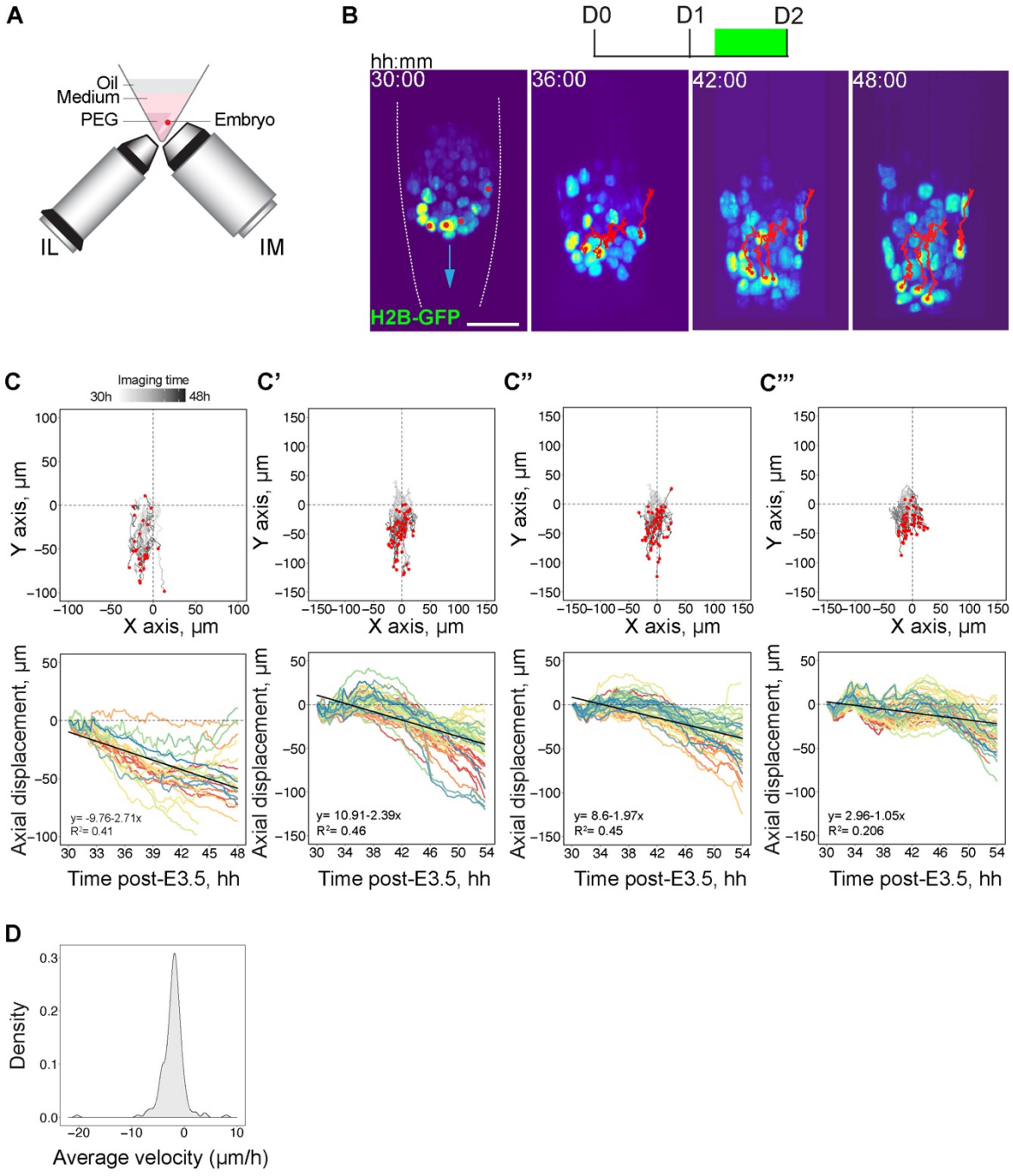

Figure 4.14. A, schematic for the inverted light-sheet microscopy, with illumination objective (IL) and imaging objective (IM). B, representative 3D projections of time-lapse images of the H2B-GFP embryo developing in the crypts made of PEG with RGD. n = 4, N = 3. Trajectories of individual mural TE cells are marked with red lines. The crypt surface is outlined. t =00:00, hours: minutes after recovery at E3.5. C, top, mural TE cell trajectories for four different embryos; coordinates in XY plane are normalized to the starting coordinates. End coordinates are marked with red dots. Bottom, displacement of mural TE cells along the Y-axis vs imaging time post-E3.5. From left to the right, n of cells = 29, 61, 58, 51, respectively. The linear regression fit is shown as a black line. D, Distribution density of the average TB velocities (μm/h). 255 cells in total, n = 6, N = 4.

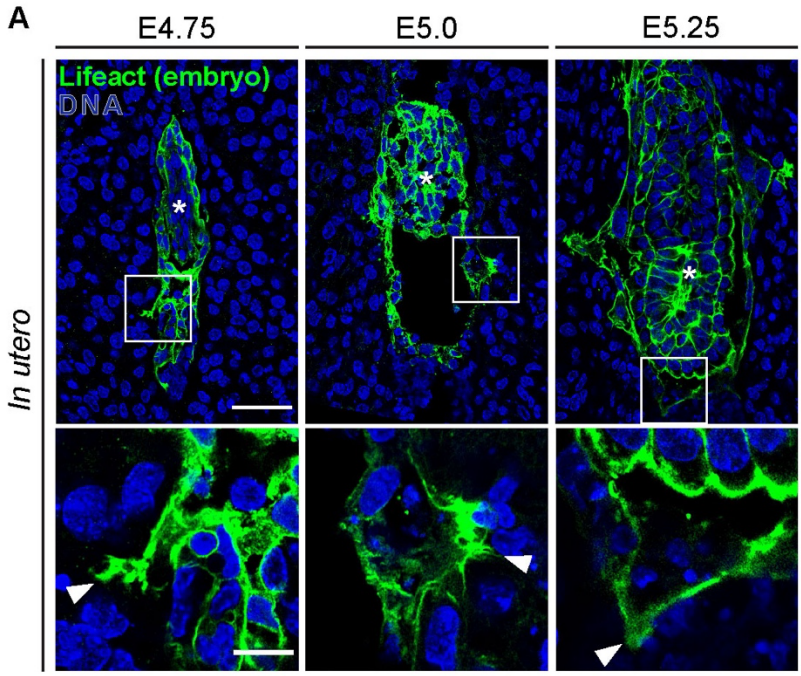

Figure 4.15. Left to right, representative immunofluorescence images of the E4.75, E5.0, and E5.25 uterus cross-sections from F1 females mated with Lifeact-GFP males; simultaneous staining for GFP (green) and nuclei (DNA, blue). n = 3, N = 1 (E4.75); n = 7, N = 3 (E5.0); n = 6, N = 3 (E5.25). Bottom, 4x zoom. Scale bars, 50 μm, 12.5 μm (4x zoom). White arrowheads point at the membrane protrusions. White asterisks mark epiblast of the implanted embryos.

4.2.3 Trophoblast cells undergo epithelial-mesenchymal transition

I further characterized mTE/TB dynamics at the sub-cellular level. I examined how the apical side of mTE cells, which initially lacks integrin beta 1 (Figure 4.8D), could mediate migration in the uterine ECM. Immunofluorescence staining of 3E-uterus embryos at D2 showed basolateral localization of the apical polarity marker, pERM, and apical localization of the basal marker, integrin beta 1, in contrast to the *in utero* E4.5 embryos (Figure 4.16A-D, Kim et al., 2022). Localization of the tight-junction marker, ZO-1, is also rearranged and becomes disorganized during 3E-uterus culture (Figure 4.17A-C). These data, supported by the loss of E-cadherin (Damjanov et al., 1986), suggest that mTE cells undergo epithelial-mesenchymal transition (EMT; Campbell & Casanova, 2016; Larue & Bellacosa, 2005) during their differentiation into TB.

Upon adhesion to the uterine matrix, EMT leads to mesenchymal migration of the TB. In line with this, light-sheet microscopy of lifeact-GFP;mTmG and Myh9-GFP;mTmG (Zhang et al., 2012) embryos (Figure 4.18A-D) showed apical actomyosin enrichment at the adhesion side of mTE, followed by dynamic lamellipodia and filopodia formation in the TB migration front along the crypt axis and laterally (Figure 4.18A-B).

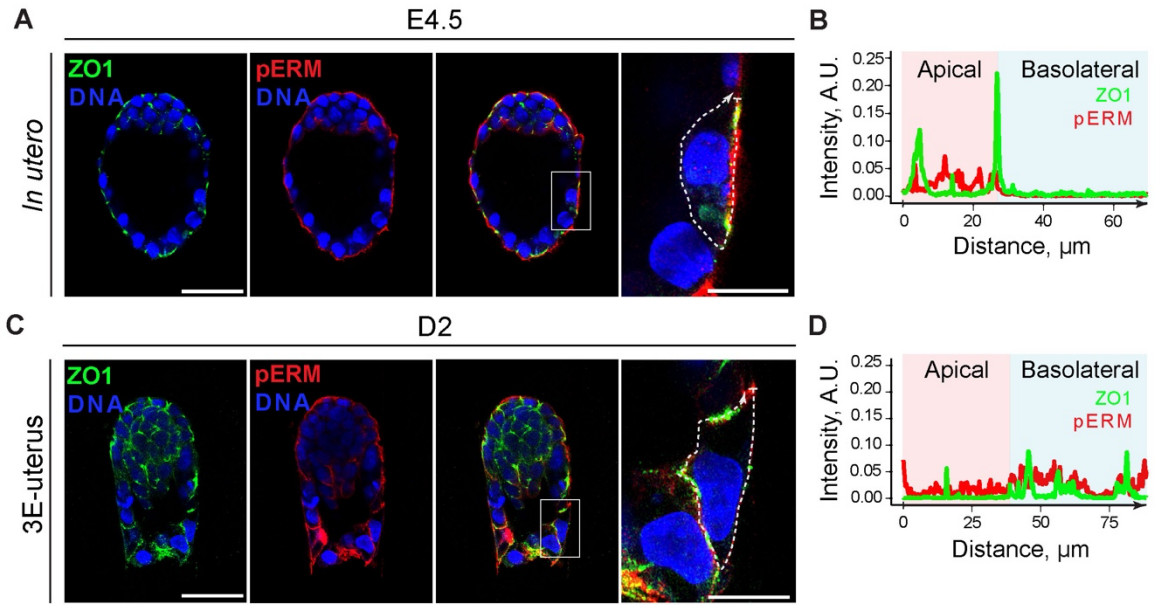

Figure 4.16. A, representative immunofluorescence image of the E4.5 embryo developed *in utero*, simultaneously stained for ZO-1 (green), phospho-Ezrin/Radixin/Moesin (pERM, red), and nuclei (DNA, blue). From left to right, ZO1, pERM, composite image channels. n = 5. Right, 4x zoom into a mTE cell. B, intensity profile for ZO1 and pERM signals along the cell surface outlined in A (right), including apical and basolateral regions. C, representative immunofluorescence image of the 3E-uterus embryo from day 2, simultaneously stained for ZO-1 (green), phospho-Ezrin/Radixin/Moesin (pERM, red), and nuclei (DNA, blue). From left to right, ZO1, pERM, composite image channels. n = 5. Right, 4x zoom into a TB cell. D, intensity profile of ZO1 and pERM signals along the cell surface outlined in C (right), including apical and basolateral regions. Scale bars, 50 µm, 15 µm (A, C, right).

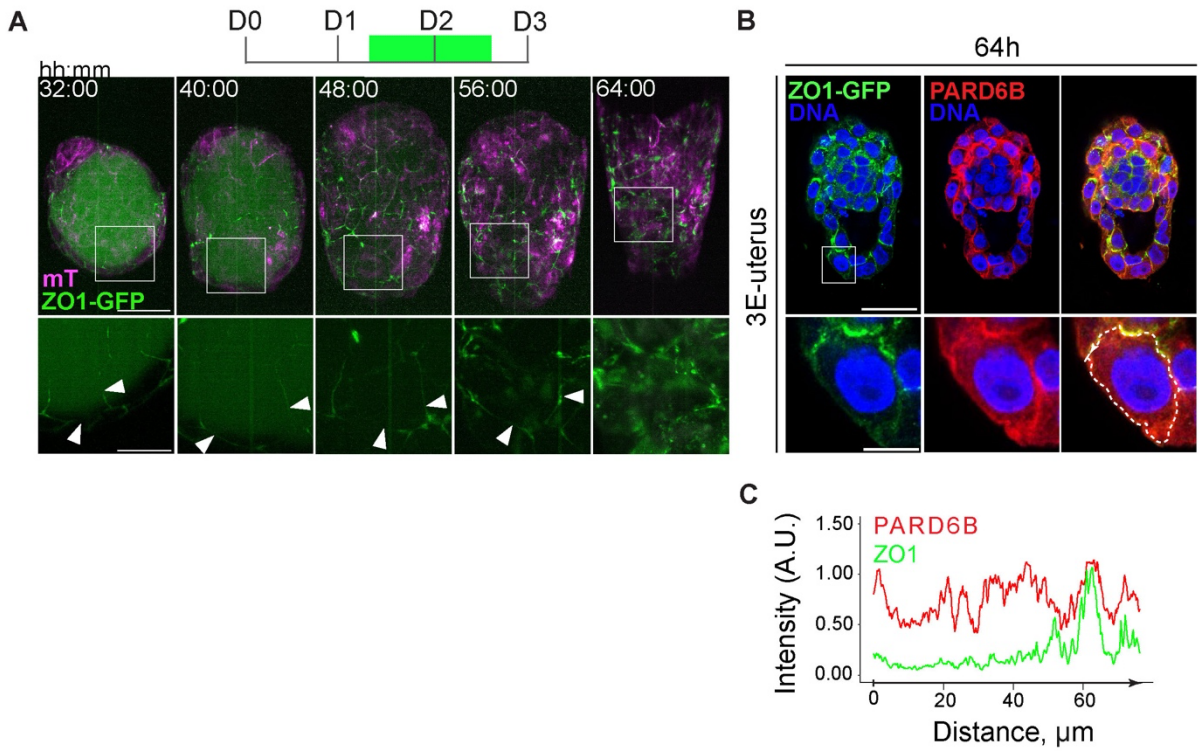

Figure 4.17 A, representative 3D projections of time-lapse images of ZO1-GFP;mTmG developing embryo; ZO1-GFP (green), mTomato (magenta). Bottom, 2.5x zoom into a TE cell; white arrowheads mark cell-cell interface. n = 7. B, representative immunofluorescence images of the 3E-uterus embryo after live imaging, simultaneously stained for ZO1-GFP (green) PARD6B (red), and nuclei (DNA, blue). From left to right, ZO1-GFP, PARD6B, composite image channels. n = 7. Bottom, 4x zoom of the TB cell. C, intensity profile of ZO1 and PARD6B signals along the cell surface outlined in B (bottom), including apical and basolateral regions. Scale bars, 50 µm, 20 µm (2.5x zoom, A), 12.5 µm (B, 4x zoom).

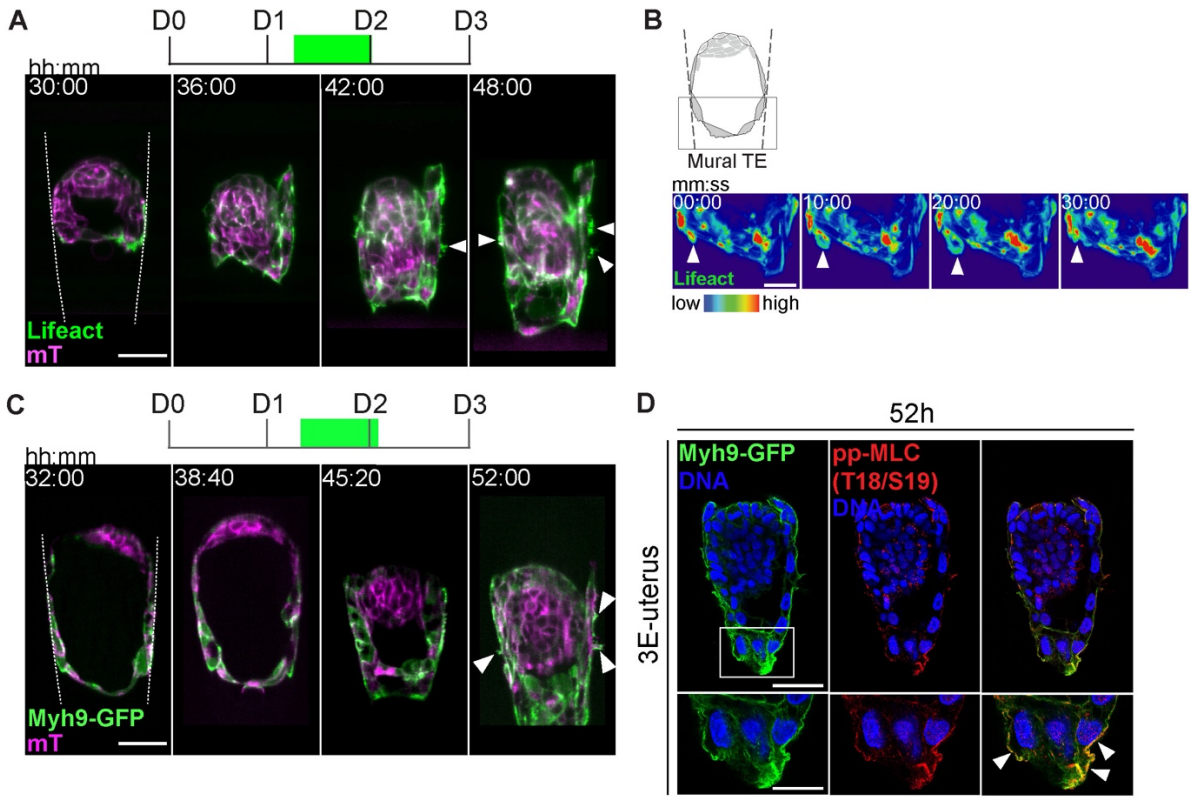

Figure 4.18. A, representative time-lapse images of the developing Lifeact-GFP;mTmG embryo; Lifeact-GFP (green), mTomato (magenta). n = 5, N = 3. The crypt surface is outlined. White arrowheads point at the trophoblast membrane protrusions. t=00:00, hours: minutes after recovery at E3.5. B, 3D projections of the time-lapse images of mural TE in the developing Lifeact-GFP embryo; Lifeact-GFP (spectral). White arrowheads point at lamellipodium. t=00:00, minutes: seconds during the arbitrary time interval of the embryo culture. C, representative single-plane time-lapse images of the Myh9-GFP;mTmG developing embryo; Myh9-GFP (green), mTomato (magenta). n = 9. The crypt surface is outlined. t=00:00, hours: minutes after recovery at E3.5. D, representative immunofluorescence images of the 3E-uterus embryo after live imaging, simultaneously stained for Myh9-GFP (green) phospho-MLC (T18/S19) (red), and nuclei (DNA, blue). From left to right, Myh9-GFP, phospho-MLC (T18/S19), composite image channels. n = 9. Bottom, 2x zoom. White arrowheads point at the apical TB cell surface. Scale bars, 50 µm, 25 µm (B; D 2x zoom).

4.2.4 Collective trophoblast migration delineates uterine space for embryo morphogenesis

These findings indicate that adhesion of the embryo to the uterine matrix induces a wetting process at the tissue level, enabling TE tension release, EMT, and collective migration of TB cells at the cellular and tissue levels. However, it remains missing how the observed growth of the egg cylinder (Figure 4.9, 4.10) is accommodated. I hypothesized that the functional relevance of collective TB migration could be to provide space extension via displacement of the Reichert's membrane, thus enabling egg cylinder formation within. An advantage of the 3E-uterus *ex vivo* system is that it allows perturbation with spatio-temporal control. Provided with this unique experimental flexibility, I perturbed the key parameters for testing this hypothesis, the TB migration velocity, and the geometry of the uterus.

I first asked whether TB migration is dependent on Rac1 (Rac Family Small GTPase 1), a mediator of cytoskeletal reorganization, essential for collective cell migration during mouse AP-axis specification (Migeotte et al., 2010) and gastrulation (Migeotte et al., 2011; Saykali et al., 2019). Pharmacological inhibition of Rac1 by NSC23766 revealed retention of the TB migration front relative to the control embryos from the same litter imaged side-by-side (Figure 4.19A, B). The effect was reversible as wash-out after 48h restored the migration, although delayed to the control embryo (Figure 4.19A). I then analyzed the development of the Rac1 mutant embryos (Walmsley et al., 2003). It was shown that $Rac1^{-/-}$ embryos undergo growth retardation starting from E5.75 and arrest during gastrulation (Sugihara et al., 1998; Migeotte et al., 2010), but not before implantation. To discern the contribution of TB migration as one of the earliest migration processes in the blastocyst, I cultured E3.5 embryos during the peri-implantation time window in 3E-uterus until the third day (Figure 4.19C). Interestingly, the embryo length, reflecting the extent of TB migration, was significantly lower in $Rac1^{-/-}$ embryos (Figure 4.19D). Moreover, $Rac1^{-/-}$ embryos had fewer EPI cells, suggesting delayed growth (Figure 4.19E). Collectively, my results indicate that TB migration is dependent on Rac1 and possibly feedbacks to the embryo growth during peri-implantation mouse development.

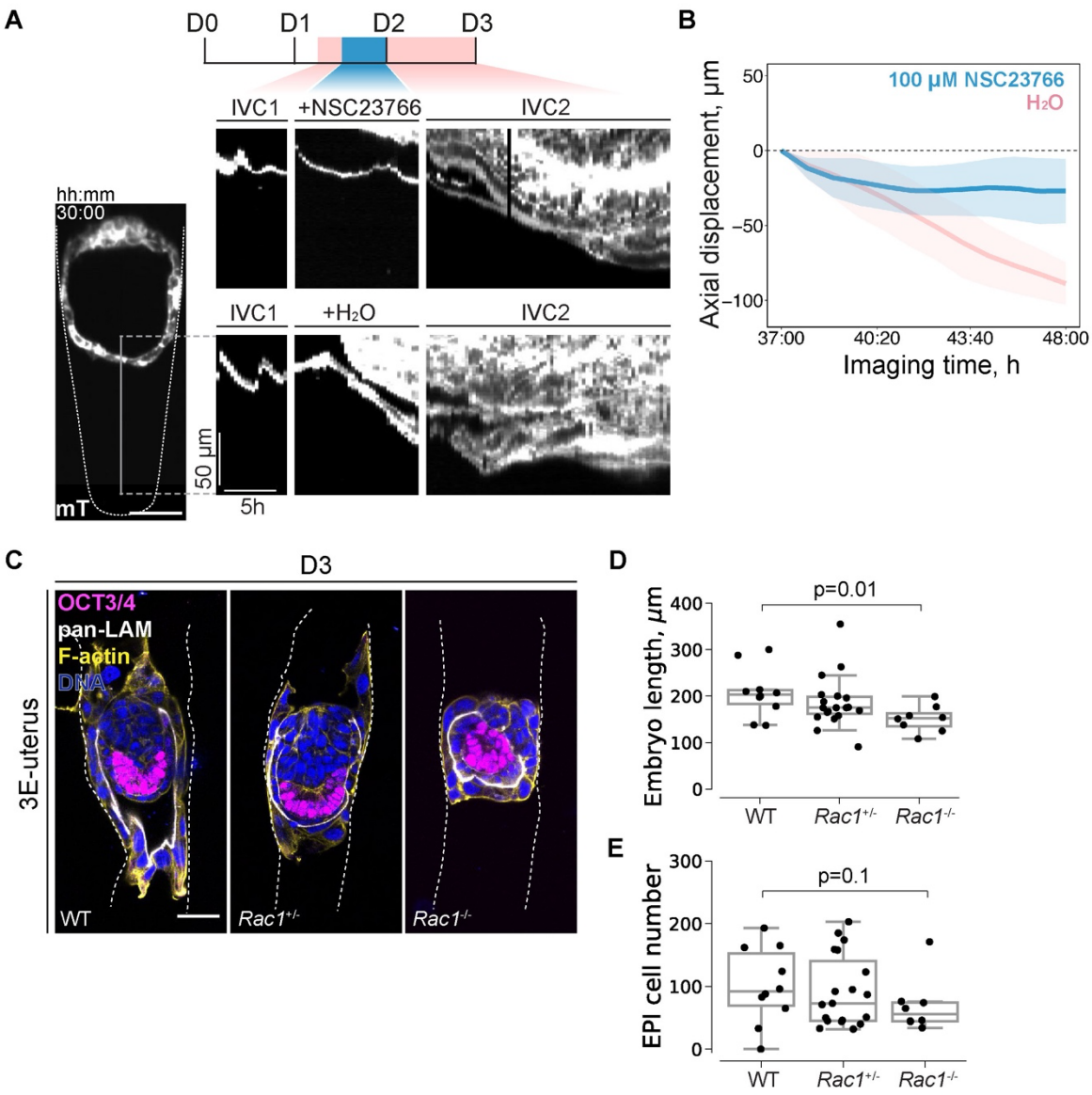
A
D0
D1
D2
D3
IVC1
+NSC23766
IVC2
hh:mm
30:00
IVC1
+H₂O
IVC2
50 µm
5h
mT
B
100 µM NSC23766
H₂O
Axial displacement, µm
50
0
−50
−100
37:00
40:20
43:40
48:00
Imaging time, h
C
D3
3E-uterus
OCT3/4
pan-LAM
F-actin
DNA
WT
Rac1+/-
Rac1-/-
D
p=0.01
Embryo length, µm
400
300
200
100
0
WT
Rac1+/-
Rac1-/-
E
p=0.1
EPI cell number
300
200
100
0
WT
Rac1+/-
Rac1-/-

Figure 4.19. A, kymographs showing mural TE leading-edge displacement along the Y-axis, indicated with the solid line on the left-most panel. Embryos from the same litter were incubated with 100 μM NSC23766 (top) and water (bottom) in IVC1 between 37 h and 48 h after recovery at E3.5; mTomato (grey). C, mural TE leading-edge displacement along the Y-axis in embryos, incubated with 100 μM NSC23766 (blue) and water (pink) in IVC1 between 37 h and 48 h. n = 4, 4, respectively. Average values (solid lines) and standard deviations (shaded area) are shown. C, left to right, representative immunofluorescence images of WT, Rac1+/-, and Rac1-/- embryos, cultured up to day 3 (D3) with 3E-uterus. Simultaneous staining for OCT3/4 (magenta), pan-Laminin (pan-LAM, white), F-actin (yellow), and nuclei (DNA, blue). n = 10 (WT), 19 (Rac1+/-), 8 (Rac1-/-), N = 3. The crypt surface is outlined. D, boxplots showing embryo length in WT, Rac1+/-, and Rac1-/- embryos. n = 10 (WT), 19 (Rac1+/-), 8 (Rac1-/-), N = 3. Data points correspond to embryos, midline marks the median, boxes indicate interquartile range. P-values were calculated using Mann-Whitney U test. E, boxplots showing epiblast cell number between WT, Rac1+/-, and Rac1-/- embryos. n = 10 (WT), 19 (Rac1+/-), 8 (Rac1-/-), N = 3. Data points correspond to embryos, midline marks the median, boxes indicate interquartile range. P-values were calculated using Mann-Whitney U test. Scale bars, 50 μm.

The displacement velocity of Reichert's membrane depends on the geometry of the 3E-uterus, too. To test this, I interfered with embryo orientation within the crypt. When I placed the embryo upside-down with an abembryonic pole directed upward, it restricted available space for collective migration in identical crypts (Figure 4.20, C). Quantification of the embryonic pole and RM displacements revealed coordination of the egg cylinder elongation with the TB migration (Figure 4.20 B'). Strikingly, in the upward orientation, TB migration was blocked, and the egg cylinder could not elongate further (Figure 4.20C, C'), indicating that spatial coordination by geometry is disrupted in restricted migration space. In contrast, egg cylinder growth progressed in the downward orientation, although the rate of embryonic pole displacement slowed down by the end of the experiment (Figure 4.20B). These data indicate that the spatial coordination is disrupted by a change in the 3E-uterus geometry, leading to the impairment of the EPI morphogenesis.

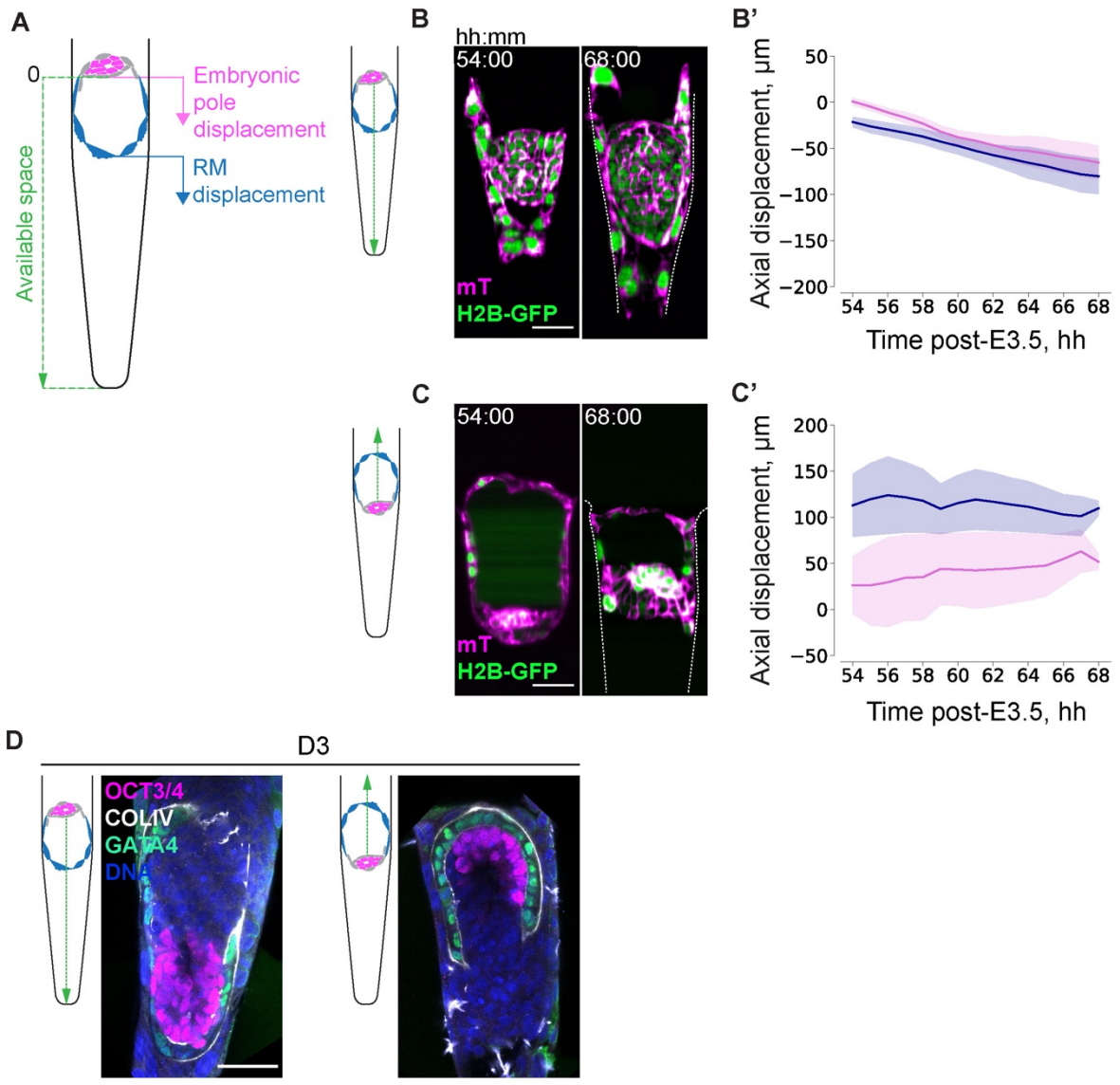

Figure 4.20. A, schematic of the quantified parameters, embryonic pole displacement (pink), RM displacement (blue) along the crypt axis (green). Coordinates are scaled to the starting coordinate of the embryonic pole. B, representative time-lapse images of H2B-GFP;mTmG developing embryo in a downward orientation; GFP (green), mTomato (magenta). N = 2. B', average displacement of the embryonic pole (pink line) and RM (blue line) along the crypt axis in the downward developing embryo. Shaded regions indicate standard deviation. C, representative time-lapse images of H2B-GFP;mTmG developing embryo in an upward orientation; GFP (green), mTomato (magenta). N = 2. C', average displacement of the embryonic pole (pink line) and RM (blue line) along the crypt axis in the upward developing embryo. Shaded regions indicate standard deviation. D, representative immunofluorescence images of 3E-uterus embryos from day 3 in the downward (left) and upward (right) orientations, simultaneously stained for OCT3/4 (magenta), GATA4 (green), and nuclei (DAPI, blue). n = 10 and n = 8, respectively. Scale bars, 50 µm.

4.2.5 Coordination model of embryo morphogenesis during implantation

My findings can be summarized into a new peri-implantation mouse embryo development model based on tissue-tissue interaction and interdependent tissue coordination (Figure 4.21). Integrin-mediated adhesion between the mTE and the uterus provides TE tension release and enables collective Rac1-dependent TB migration. TE tension release and TB migration promote egg cylinder formation and growth by ExE/EPI patterning and space extension, respectively. The coordination of the dynamics of the embryonic and extraembryonic tissues strictly relies on uterine adhesiveness and geometry, and abrogation of these properties disrupts tissue coordination. The spatiotemporal coordination by the uterine tissue therefore provides an essential mechanism for robust peri-implantation embryo development.

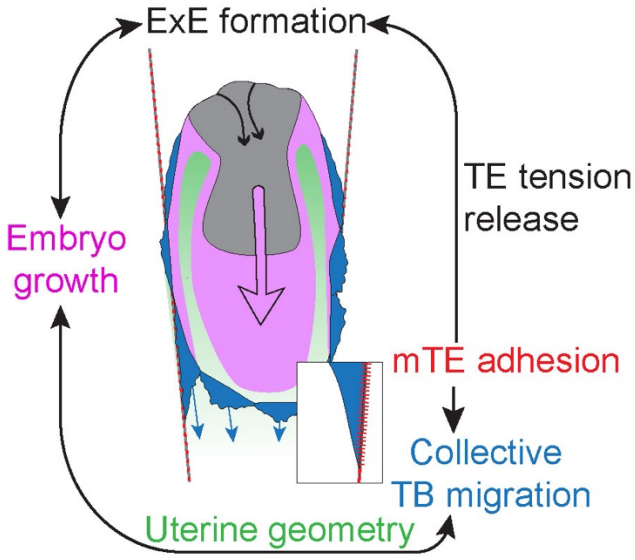

Figure 4.21. Schematic of the proposed model of peri-implantation mouse embryo morphogenesis. Mural TE (mTE) integrin-mediated adhesion to the uterine tissue triggers ExE formation via TE tension release and enables collective Rac1-dependent trophoblast (TB) migration which delineates uterine space for embryo morphogenesis and growth.

4.3 Spatiotemporal multicolor live cell labelling using Brainbow system

Multidimensional analysis of cell fate dynamics is invaluable for understanding complex intra- and intercellular processes such as morphogenesis. The established peri-implantation embryo culture and live imaging allow asking how the intercellular communication and signaling are spatiotemporally controlled in the developing embryo. However, although transcriptome sequencing provides comprehensive profiling of the cellular transcription and inference of signaling activities, cell identities, and developmental trajectories, it does not provide direct dynamic and spatial information.

To combine the spatial cell fate resolution and lineage dynamics in one assay, I developed fluorescent imaging through the genetic system, initially applied in neuroscience, 'Brainbow' (Loulier et al., 2014). This Cre-lox-based fluorescent cell labeling technique allows rapid, inducible, and heritable cell labeling by multiplexing fluorophores (Loulier et al., 2014). I increased the multiplexity of the Brainbow labels and established a targeted integration into the mouse genome. I then performed live imaging to confirm the expression of the fluorescent markers. In collaboration with M. Blottenburg at A. von Oudenaarden's group, I tested the possibility of using single-cell RNA sequencing to identify fluorescent labels and reconstruct clonal identities together with molecular cell states (Figure 4.22).

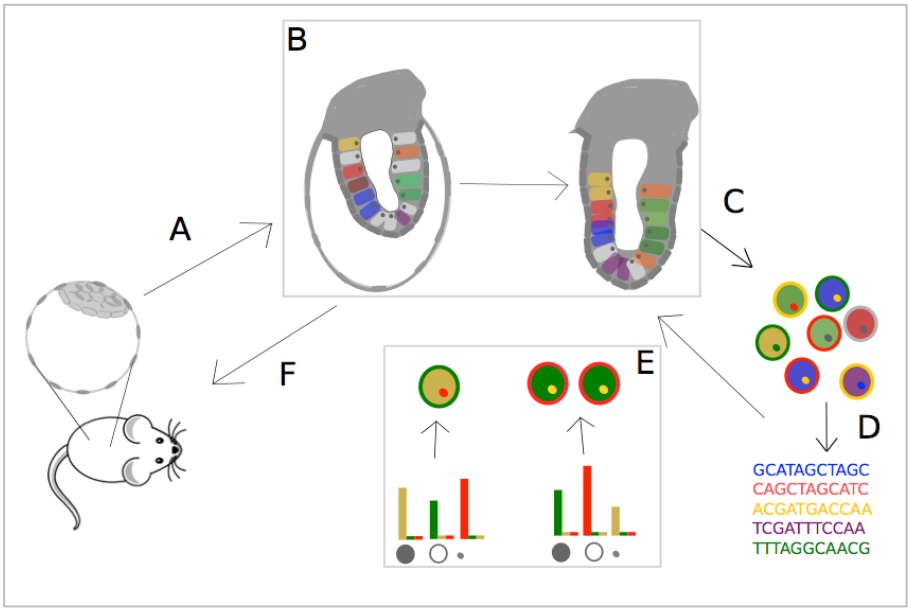

Figure 4.22. Summary of the experimental strategy. A, embryo isolation at the blastocyst stage and induction of cell labelling. B, live imaging. C, dissociation into single cells. D, singe cell sequencing. E, reconstruction of the spatial information. F, intrauterine embryo delivery.

4.3.1 Characterization of the system in ESC

The results of ddPCR confirmed a single full-length insertion of the transgenic pBBAC construct in the ESC. In the second round of transgenesis, I inserted ERT2-Cre under the ROSA26 promoter. To test whether Cre activity could result in a change of fluorescence in live cells, I exposed double-transgenic ESC to 1 µM Tamoxifen for 6 hours and, in 24 hours, observed fluorescence under a confocal microscope. As expected, the non-treated negative control ESC expressed only nuclear iRFP (Figure 4.23 A). However, recombination induction with TAM led to mosaic labeling with a diversity of cell labels, corresponding to the single full-length insertion (Figure 4.23 B). The nuclear signal was abundant for all colors (Cerulean, YFP, mCherry). Plasma membrane-bound signal was the most frequent for YFP and mCherry; mitochondrial labeling was observed for YFP and mCherry. To further explore whether the expression of the fluorescent label could be maintained long-term for studying clonal dynamics, I performed time-lapse imaging of the induced ESC colonies. Live imaging

demonstrates maintenance of the fluorescence during clonal expansion (Figure 4.23 C), providing proof-of-principle evidence that the system could be used *in vivo*.

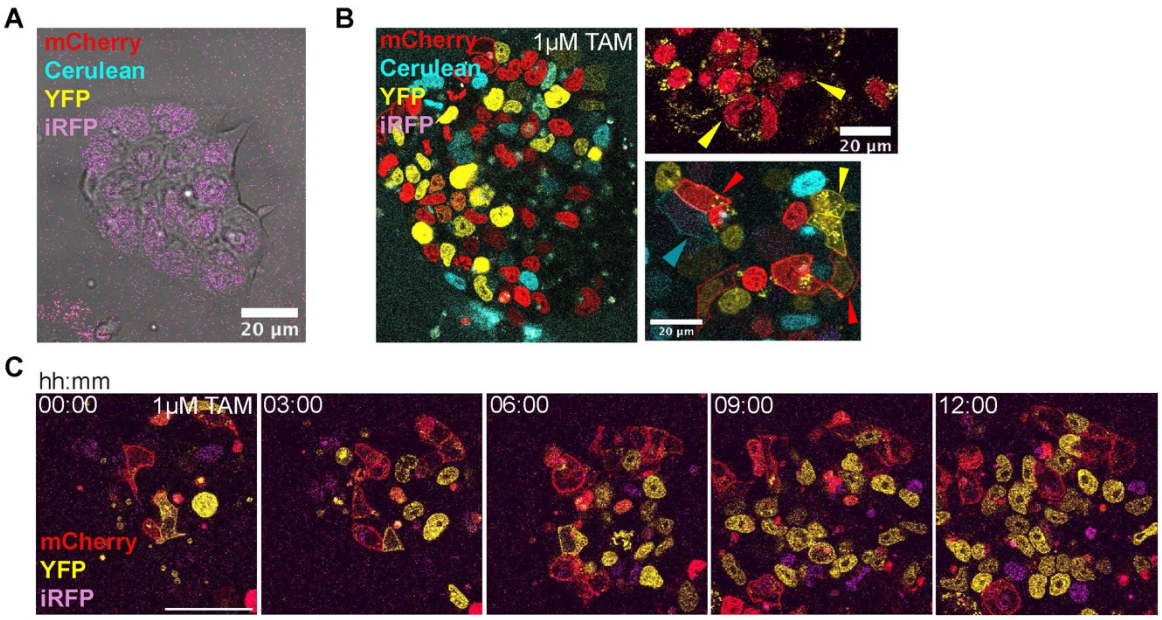

Figure 4.23. Characterization of the new brainbow system in ESC. A, fluorescence of the ESC colony without induction of Cre activity (control). ESC labels in 24 hours after induction with 1 µM Tamoxifen (TAM). Arrows point to the different color labels. C, representative time-lapse images of the ESC colony proliferating for 12 hours after induction with 1 µM TAM.

4.3.2 Testing in the mouse embryos

The injection of ESC into blastocysts produced chimeric animals, which were bred to establish the mouse line, heterozygous for the pBBAC (Brainbow) insertion. The established mouse like was called 'Embryobow'. The transgenic embryos were dissected and analyzed for fluorescence at E5.5 and E6.0 using InVi-SPIM. Live imaging of non-induced embryos showed that iRFP fluorescence is unexpectedly restricted to EPI and is heterogeneous within the tissue (Figure 4.24 A, left; B, left). Based on this expression pattern, I then asked whether the change of fluorescence can be induced in EPI.

To provide Cre expression in EPI, Embryobow animals were mated with a Sox2Cre line (Cre under Sox2 promoter; Hayashi et al., 2002). After live imaging, embryos were genotyped for Cre to confirm its presence. Notably, cells expressed all fluorophores in plasma membrane and nucleus in EPI cells of the embryos where Cre was present (Figure 4.24A, B). Heterogeneity of the nuclear and plasma membrane labels within and between embryos was evident, but the low fluorescence intensity obstructed further quantitative characterization of the clonal diversity.

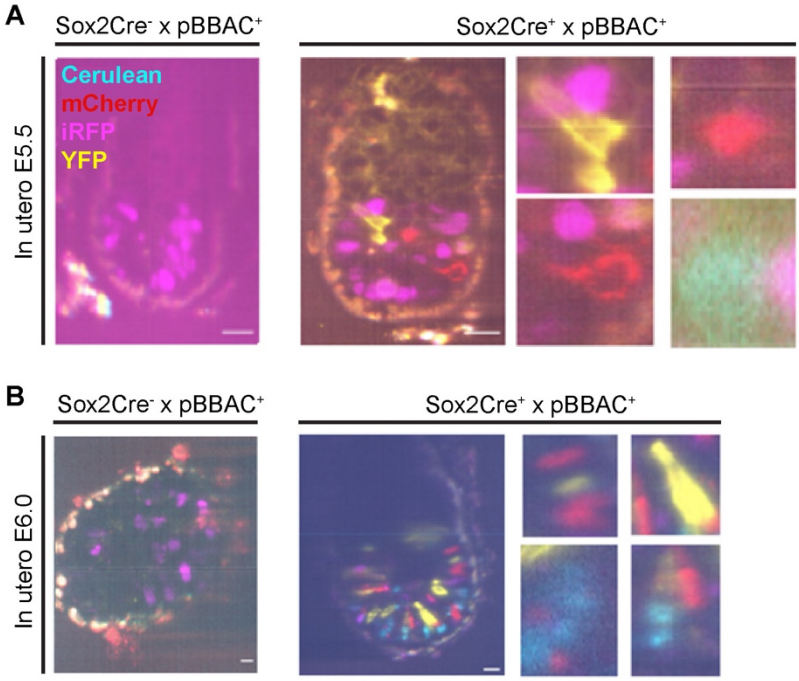

Figure 4.24. Testing the transgenic brainbow system in the developing mouse embryos. A, Fluorescence of the pBBAC ("Embryobow") embryos without Cre (left) and with Cre (right) developed *in utero* until E5.5. B, Fluorescence of the pBBAC embryos without Cre (left) and with Cre (right) developed *in utero* until E6.0.

5 DISCUSSION

5.1 *Ex vivo* engineering uterine environment

In this study, an engineered uterus, 3E-uterus, was developed, which allowed for the first time to recapitulate the development of the whole embryo, including embryonic and extraembryonic tissues *ex vivo* during peri-implantation time window. Using topographical hydrogel modification and chemically-defined materials, it reconstituted aspects of the embryo-uterus interaction and supported the differentiation of TB cells and the Reichert's membrane. Combined with light-sheet microscopy methods, this system makes it possible to live image the cellular dynamics and perturb cellular processes by genetic, pharmacological, and biophysical methods (Bondarenko et al., 2022). The main advantage is that it allows complete control of the experimental parameters, hence providing mechanistic insights.

A recent study from M. Lutolf's group found that extrinsically provided tissue geometry guides patterning and morphogenesis of intestinal organoids via robust spatial gradients of the cell density and signaling (Gjorevski & Nikolaev et al., 2022). In the mouse embryo system, external confinement was suggested to facilitate robust Anterior-Posterior (A-P) axis patterning (Hiramatsu et al., 2013). However, how the uterine tissue geometry affects the cell behavior of the extraembryonic tissues and the establishment of the peri-implantation morphology remained unknown. Here, a new mechanism was revealed, where mammalian blastocyst morphogenesis and growth upon implantation rely on spatial coordination of the collective TB migration by the uterine tissue geometry.

In mice, uterine tissue geometry has a crypt shape upon implantation at E4.75, and the uterine tissue comprises the luminal epithelium, the ECM, and the underlying stroma (Figure 4.3). The epithelium is shed off during implantation, and by E5.0-E5.25, the embryo contacts the ECM and the stroma (Figure 4.3; Li et al., 2015). Interestingly, dead epithelial cells accumulate at the bottom of the crypt, suggesting that they might be physically pushed down by the migratory TB (Figure 4.3). The dynamic removal of the epithelial interface suggests that uterine epithelium might not be required for morphological change of the embryo once the embryo-uterine interaction is established. Indeed, despite the absence of uterine cells in the current culture method, embryos formed egg cylinder morphology.

The controlled synthetic hydrogel-based engineered system allowed evaluation of how the tissue parameters, such as geometry, stiffness, and adhesion,

independently affect embryo development. The results of stiffness modulation indicate that embryonic growth requires a low-stiffness environment (Figure 4.5; Govindasamy et al., 2021). This could be due to the disrupted collective migration in a non-optimal stiffness range or because our system has to provide both soft (corresponding to epithelial cells) and stiff (ECM) properties and thus, the embryos develop best in the optimum range. It remains unclear how exactly the ECM stiffness relates to the collective TB movement of the TB. This can be addressed with live imaging and measurement of the migration speed and directionality in different stiffness conditions.

5.2 Current limitations and perspectives of *ex vivo* peri-implantation embryo culture

With new advancements, my study also introduces new challenges. 3E-uterus embryos reached the E4.5 stage in approximately two days instead of one day of *in utero* development. The early developmental delay was also observed in the previous *ex vivo* studies (Bedzhov et al., 2014; Govindasamy et al., 2021) and is typical even for the pre-implantation embryo culture, suggesting that additional cues might be required to enable timely adaptation of the trophectoderm to the *ex vivo* environment. Uterine endometrium provides a complex composition of adhesive molecules and secreted growth factors before the embryo reaches the underlying ECM (Dey et al., 2004). Therefore, although after the establishment of the embryo-uterine interaction, epithelium might not be required, it might be required for a timely establishment of the embryo-uterine reaction. Most likely, several (yet unknown) regulatory feedback mechanisms enable robust temporal coordination of the embryo-uterine interaction. Incorporating cellular components (epithelium and stroma) into our platform will facilitate understanding the role of cell-cell interactions and signaling between the embryo and the uterus. 3E-uterus provides an excellent experimental platform for such mechanistic studies. In perspective, it can help understand the functional cross-talk between the uterine tissue dynamics, embryo morphology, and size.

To accommodate late-stage embryo development, the uterus can be engineered further. More bio-degradable and dynamic hydrogels may help accommodate embryo development through advanced stages (Brassard & Lutolf, 2019; Chrisnandy et al., 2022; Qazi et al., 2022). The long-term challenges are

uncovering the uterine tissue's mechanochemical response to the embryo growth, the mechanisms of placental formation, and dynamic nutritional exchange. Addressing those problems will require understanding the fundamental mechanisms of the feto-maternal dynamics, further advancement in technology (microfluidics, cell, and tissue engineering), and adaptive live imaging for the mesoscopic multicellular and multi-tissue samples.

5.3 Trophoblast cell adhesion and dynamics

Trophoblast outgrowth was noticed long ago when the mouse embryos were first cultured on the dish surface (Gwatkin et al., 1966). Anne Sutherland and colleagues further substantiated an understanding of the role of integrins in trophoblast cell motility (reviewed by Sutherland, 2003). Using Rcho-1 cells and the ectoplacental cone explants with secondary giant trophoblast, her group showed that although TB cells are motile initially, their speed decreased during maturation into giant trophoblast (Parast et al., 2001). Of note is that mTE-derived primary giant trophoblast cells are not the same as the ones used in the (Parast et al., 2001) study. However, although live imaging until day 3 of *ex vivo* culture indicates TB motility, it is possible that the TB actively migrates only during early implantation, and after TB maturation during later stages, its migration decreases.

In utero, the space for embryo growth could also be provided by the phagocytosis and degradation of the uterine matrix and cells. In line with this, the extracellular vesicles of embryonic origin are frequently seen during my live imaging and *in utero*. Moreover, while the TB cells differentiate, they exit the cell cycle and undergo endoreduplication; their nuclear size and cell volume also increase (Barlow & Sherman, 1972; Ilgren, 1983). Therefore, along with migration, an expansion of TB tissue volume can also contribute to space availability for embryo growth, for example, during later stages.

Using glutaraldehyde fixation with tannic acid, Salamat and colleagues found that the mural trophoblast cells first deposit a primary membrane, which becomes maturated into a multilayer Reichert's membrane by PE and the TB (Salamat et al., 1995). The dynamics of RM elongation by synthesis have not been addressed in this study. It would be interesting to consider an experimental perturbation of the RM by

inhibition of its synthesis or mechanical integrity (e.g., ablation) or to monitor the live dynamics of the laminin synthesis. Hypothetically, the RM synthesis by PE could provide a positive feedback loop between TB migration and the egg cylinder growth.

5.4 The role of embryo-uterine interaction in embryo orientation and shape

Live imaging in 3E-uterus demonstrates that the mouse embryos do not self-correct their ICM orientation within the static crypt environment (Chen et al., 2013). This further suggests that the stereotypic orientation of the conceptus along the mesometrial/anti-mesometrial (M/A-M) axis *in utero* is extrinsically regulated by the dynamic environment. However, engineered crypt diameter had an impact on embryo orientation and morphology (Figure 4.4B). The funnel-shaped crypts with a diameter gradient enabled better control of embryo orientation than cylindrical crypts by increasing the chance of lateral mTE attachment, resulting in higher efficiency of 3E-uterus (Figure 4.5). However, whether a gradient of lateral (or circular) compression along the M/A-M exists *in utero* needs to be addressed experimentally.

Although uterine geometry plays a key role in peri-implantation development, it remains to be understood how the uterine tissue geometry is dynamically established. Addressing such a complex problem would require theoretical models and further advancements in the *ex vivo* engineering techniques and *in utero* monitoring (Huang et al., 2020).

5.5 Spatiotemporal lineage recording of the mouse embryo

The developed method of spatiotemporal lineage labeling can be applied to embryonic cells. The exact reason for low iRFP fluorescence in extraembryonic cells remains unclear. This could be, for example, due to tissue-specific activity of CAG promoter or lack of co-factor, biliverdin, required for iRFP fluorescence (Shemetov et al., 2017), in extraembryonic tissues, such as ExE and TB. Interestingly, when cell-permeable Cre was administered externally to the TE at E3.5, diverse fluorophores

were expressed in TE. Overall, the system's applicability for differentiated tissues remains to be further characterized.

High efficiency and fluorescence in ESC open the possibility of using this method for ESC-derived systems, such as gastruloids (van den Brink, 2014). Endogenous double transgenesis provides tamoxifen-inducible Cre expression alongside the fluorophores, making it tractable for temporal control of cell lineage labeling.

The low occurrence of mCherry and Cerulean in mitochondria decreases observed clonal diversity. Co-expression of differentially located fluorophores was also rarely seen, potentially indicating that the duration of Cre activity might need to be modulated further.

5.6 Ensuing questions and perspectives

How is the mechanochemical coupling between the mother and the embryo achieved across different scales? The coordination in time and space requires effective communication. From the information theory viewpoint, *how does embryo-uterine communication emerge and evolve? What are its constituents and minimal rules?* On the evolutionary time scale, the implantation strategies are remarkably plastic. However, within one species (e.g., mouse), it looks like embryos strictly rely on uterine geometry for successful implantation at a particular time. *How does evolutionary plasticity lead to developmental robustness? What is the nature of constraints shaping the phenotypic landscape of mammalian implantation? What is the role of mechanical properties? To which extend does the genetics determine mechanical inputs, or the mechanical inputs determine genetics?* Embryo implantation raises many more interesting questions. Besides being fascinating on its own, I am certain it can also teach us a lot about the general principles of biological systems organization, origin, behavior, and evolution.

With a better *in vivo* understanding and theoretical concepts explaining complex systems behavior, the synthetic approach of environmental and genetic engineering will be complementary for studying general principles of interactive and evolvable processes in (real) time.

REFERENCES

Alliston C W, Pardee N R. Variability of embryonic development in the rabbit at 19 to 168 hours after mating (1973). Lab Anim Sci. 23(5): 665-70.

Atkinson B A, King G J, and Amoroso E C. Development of the caruncular and intercaruncular regions in the bovine endometrium (1984). Biol. Reprod. 30, 763–774.

Bailles, A, Collinet C, Philippe, J M, Lenne P F, Munro E, and Lecuit T. Genetic induction and mechanochemical propagation of a morphogenetic wave (2019). Nature 572, 467–473.

Beard C, Hochedlinger K, Plath K, Wutz A, Jaenisch R. Efficient method to generate single-copy transgenic mice by site-specific integration in embryonic stem cells (2006). Genesis. (1): 23-8.

Barlow P W, Sherman M I. The biochemistry of differentiation of mouse trophoblast: studies on polyploidy (1972). J Embryol Exp Morphol. 27: 447–465.

Bedzhov I, Leung C Y, Bialecka M, and Zernicka-Goetz M. In vitro culture of mouse blastocysts beyond the implantation stages (2014). Nature Protocols 9, 2732–2739.

Behringer R, Gertsenstein M, Nagy K, and Nagy A. Manipulating the Mouse Embryo: A Laboratory Manual (2014). Cold Spring Harbor (New York): Cold Spring Harbor Laboratory Press.

Beier T, Pape C, Rahaman N, Prange T, Berg S, Bock D D, Cardona A, Knott G W, Plaza S M, Scheffer L K, et al. Multicut brings automated neurite segmentation closer to human performance (2017). Nature Methods 14, 101–102.

Berg S, Kutra D, Kroeger T, Straehle C N, Kausler B X, Haubold C, Schiegg M, Ales J, Beier T, Rudy M, et al. ilastik: interactive machine learning for (bio)image analysis (2019). Nature Methods 16, 1226–1232.

Blackburn D G. Evolution of vertebrate viviparity and specializations for fetal nutrition: A quantitative and qualitative analysis (2015). J Morphol. 276(8): 961-90.

Bondarenko V, Nikolaev M, Kromm D, Belousov R, et al. Coordination between embryo growth and trophoblast migration upon implantation delineates mouse embryogenesis (2022). BioRxiv. https://doi.org/10.1101/2022.06.13.495767.

Boretto M, Cox B, Noben M, Hendriks N, Fassbender A, Roose H, Amant F, Timmerman D, Tomassetti C, Vanhie A, et al. Development of organoids from mouse and human endometrium showing

endometrial epithelium physiology and long-term expandability (2017). Development (Cambridge) 144, 1775–1786.

Brassard J A, and Lutolf M P. Engineering Stem Cell Self-organization to Build Better Organoids (2019). Cell Stem Cell 24, 860–876.

Brennan J, Lu C C, Norris D P, Rodriguez T A, Beddington R S P, and Robertson E J. Nodal signalling in the epiblast patterns the early mouse embryo (2001). Nature 411, 965–969.

Brody J R, and Cunha G R. Histologic, morphometric, and immunocytochemical analysis of myometrial development in rats and mice: I. Normal development (1989). Am. J. Anat. 186, 1–20.

Brunet T, Bouclet A, Ahmadi P., et al. Evolutionary conservation of early mesoderm specification by mechanotransduction in Bilateria (2013). Nat Commun. 4, 2821.

Burckhard, G. (1901). Die Implantation des Eies der Maus in die Uterusschleimhaut und die Umbildung derselben zur Decidua. Archiv f. mikrosk. Anat. *57*, 528–569.

Caliari S R and Burdick J A. A practical guide to hydrogels for cell culture (2016). Nature Methods 13, 405–414.

Caligioni C S. Assessing reproductive status/stages in mice (2009). Curr Protoc Neurosci. Appendix 4: Appendix 4I.

Campbell K and Casanova J. A common framework for EMT and collective cell migration (2016). Development (Cambridge). 143, 4291–4300.

Carson D D, Tang J P, Julian J. Heparan sulfate proteoglycan (perlecan) expression by mouse embryos during acquisition of attachment competence (1993). Dev Biol. 155(1): 97-106.

Cha J, Sun X, Dey S K. Mechanisms of implantation: strategies for successful pregnancy (2012). Nat Med. 18(12): 1754-67.

Chen Q, Zhang Y, Elad D, Jaffa AJ, Cao Y, Ye X, Duan E. Navigating the site for embryo implantation: biomechanical and molecular regulation of intrauterine embryo distribution (2013). Mol Aspects Med. 34(5): 1024-42.

Chen S, Krinsky, B H & Long M. New genes as drivers of phenotypic evolution (2013). Nat. Rev. Genet. 14: 645–660.

Chrisnandy A, Blondel D, Rezakhani S, Broguiere N, and Lutolf M P. Synthetic dynamic hydrogels promote degradation-independent in vitro organogenesis (2022). Nature Materials 21, 479–487.

Christodoulou N, Kyprianou C, Weberling A, Wang R, Cui G, Peng G, Jing N., and Zernicka-Goetz M (2018). Sequential formation and resolution of multiple rosettes drive embryo remodelling after implantation. Nature Cell Biology 20, 1278–1289.

Christodoulou N, Weberling A, Strathdee D, Anderson K I, Timpson P, and Zernicka- Goetz M. Morphogenesis of extra-embryonic tissues directs the remodelling of the mouse embryo at implantation (2019). Nat. Commun. 10, 3557.

Coy P, García-Vázquez F A, Visconti P E, Avilés M. Roles of the oviduct in mammalian fertilization (2012). Reproduction. 144(6): 649-660.

Çiçek Ö, Abdulkadir A, Lienkamp S S, Brox T, and Ronneberger O. 3D U-Net: Learning Dense Volumetric Segmentation from Sparse Annotation (2016). arXiv:1606.06650

Damjanov I, Damjanov A, Damsky C H. Developmentally regulated expression of the cell-cell adhesion glycoprotein cell-CAM 120/80 in peri-implantation mouse embryos and extraembryonic membranes (1986). Dev Biol. 116(1): 194-202.

Dey S K, Lim H, Das S K, Reese J, Paria B C, Daikoku T, and Wang H. Molecular cues to implantation (2004). Endocrine Reviews 25, 341–373.

Driever W, Nüsslein-Volhard C. The bicoid protein determines position in the Drosophila embryo in a concentration-dependent manner (1988). Cell. 54(1): 95-104.

Dupont S, Morsut L, Aragona M., et al. Role of YAP/TAZ in mechanotransduction (2011). Nature. 474, 179–183.

Edelman G M, and Gally J A. Degeneracy and complexity in biological systems (2001). Proc. Natl. Acad. Sci. USA. 98: 13763–13768.

Edwards J S, and Palsson B O. Robustness analysis of the Escherichia coli metabolic network (2000). Biotechnol. Prog. 16, 927–939.

Enders A C, Schlafke S, and Welsh A. Trophoblastic and Uterine Lurninal Epithelial Surfaces at the Time of Blastocyst Adhesion in the Rat (1980). Am J Anat. 159(1): 59-72.

Fairbairn J, Shine R, Moritz C, Frommer M. Phylogenetic relationships between oviparous and viviparous populations of an Australian lizard (Lerista bougainvillii, scincidae) (1998). Mol Phylogenet Evol. 10(1): 95-103.

Farrar, J.D., and Carson, D.D. (1992). Differential Temporal and Spatial Expression of mRNA Encoding Extracellular Matrix Components in Decidua during the Pen-Implantation Period. Biol Reprod. *46*, 1095–108.

Félix M A, Wagner A. Robustness and evolution: concepts, insights and challenges from a developmental model system (2008). Heredity (Edinb); 100(2): 132-40.

Flores D, Madhavan M, Wright S, Arora R. Mechanical and signaling mechanisms that guide pre-implantation embryo movement (2020). Development. 147(24): dev193490.

Foote H P, Sumigray K D, and Lechler T. FRAP analysis reveals stabilization of adhesion structures in the epidermis compared to cultured keratinocytes (2013). PLoS One 8 (8): e71491.

Frankenberg S R, de Barros F R, Rossant J, Renfree M B. The mammalian blastocyst (2016). Wiley Interdiscip Rev Dev Biol. 5(2): 210-32.

Fu J, Keurentjes JJB, Bouwmeester H, America T, Verstappen FWA, Ward JL, Beale MH, de Vos RCH, Dijkstra M, Scheltema RA, et al. System-wide molecular evidence for phenotypic buffering in Arabidopsis (2009). Nat Genet 41: 166–167

Fukuda M N, Sato T, Nakayama J, Klier G, Mikami M, Aoki D, Nozawa S. Trophinin and tastin, a novel cell adhesion molecule complex with potential involvement in embryo implantation (1995). Genes Dev. 9(10): 1199-210.

Furukawa S, Kuroda Y, Sugiyama A. A comparison of the histological structure of the placenta in experimental animals (2014). J Toxicol Pathol. 27(1): 11-8.

Funke J, Tschopp F, Grisaitis W, Sheridan A, Singh C, Saalfeld S, and Turaga S C. Large Scale Image Segmentation with Structured Loss Based Deep Learning for Connectome Reconstruction (2019). IEEE Transactions on Pattern Analysis and Machine Intelligence 41, 1669–1680.

Geisert R D, Brookbank J W, Roberts R M, Bazer F W. Establishment of pregnancy in the pig: II. Cellular remodeling of the porcine blastocyst during elongation on day 12 of pregnancy (1982). Biol Reprod, 27: 941–955.

Gershon E, Hadas R, Elbaz M, Booker E, Muchnik M, Kleinjan-Elazary A, Karasenti S, Genin O, Cinnamon Y, Gray P C. Identification of Trophectoderm-Derived Cripto as an Essential Mediator of Embryo Implantation (2018). Endocrinology. 159(4): 1793-1807.

Gjorevski N, Sachs N, Manfrin A, Giger S, Bragina M E, Ordóñez-Morán P, Clevers, H and Lutolf M P. Designer matrices for intestinal stem cell and organoid culture (2016). Nature 539, 560–564.

Gjorevski N, Nikolaev M, Brown T E, Mitrofanova O, Brandenberg N, DelRio F W, Yavitt F M, Liberali P, Anseth K S, and Lutolf M P. Tissue geometry drives deterministic organoid patterning (2022). Science 375 (6576): eaaw9021.

Govindasamy N, Long H, Jeong H W, Raman R, Özcifci B, Probst S, Arnold S J, Riehemann K, Ranga A, Adams R H, et al. 3D biomimetic platform reveals the first interactions of the embryo and the maternal blood vessels (2021). Developmental Cell 56, 3276-3287.e8.

Gwatkin R B. Amino acid requirements for attachment and outgrowth of the mouse blastocyst *in vitro* (1966). Ann N. Y. Acad. Sci. 139: 70 – 90.

Hadjantonakis A K and Papaioannou V E. Dynamic in vivo imaging and cell tracking using a histone fluorescent protein fusion in mice (2004). BMC Biotechnology 4, 33.

Hannezo E, Heisenberg C P. Mechanochemical Feedback Loops in Development and Disease (2019). Cell. 178(1): 12-25.

Hayashi S, Lewis P, Pevny L, McMahon AP. Efficient gene modulation in mouse epiblast using a Sox2Cre transgenic mouse strain (2002). Mech Dev. 119 Suppl 1: S97-S101.

Hiramatsu R, Matsuoka T, Kimura-Yoshida C, Han S W, Mochida K, Adachi T, Takayama S, and Matsuo I. External mechanical cues trigger the establishment of the anterior-posterior axis in early mouse embryos (2013). Developmental Cell 27, 131–144.

Huang, Q., Cohen, M.A., Alsina, F.C., Devlin, G., Garrett, A., McKey, J., Havlik, P., Rakhilin, N., Wang, E., Xiang, K., et al. (2020). Intravital imaging of mouse embryos. Science 368, 181–186.

Hubrecht AAW. Studies in mammalian embryology. I. The placentation of *Erinaceus europaeus*, with remarks on the phylogeny of the placenta (1889). Q J Microsc Sci; 30:283e404.

Hubrecht AAW. Early ontogenetic phenomena in mammals and their bearing on our interpretation of the phylogeny of the vertebrates (1908). Q J Microsc Sci; 53:1e181.

Ichikawa T, Zhang H T, Panavaite L, Erzberger A, Fabrèges D, Snajder R, Wolny A, Korotkevich E, Tsuchida-Straeten N, Hufnagel L, et al. An ex vivo system to study cellular dynamics underlying mouse peri-implantation development (2022). Developmental Cell 57, 373-386.e9.

Ilgren E B. Control of trophoblastic growth (1983). Placenta. 4(3): 307-328.

Iwasaki H, Eguchi S, Ueno H, Marumo F, Hirata Y. Mechanical stretch stimulates growth of vascular smooth muscle cells via epidermal growth factor receptor (2000). Am J Physiol Heart Circ Physiol. 278(2): H521-9.

Jaquemar, D., Kupriyanov, S., Wankell, M., Avis, J., Benirschke, K., Baribault, H., Oshima, R. (2003). Keratin 8 protection of placental barrier function. The Journal of cell biology. 161. 749-56.

Johnson G A, Burghardt R C, Bazer F W, Spencer T E. Osteopontin: roles in implantation and placentation (2003). Biol Reprod. 69(5): 1458-71.

Jung H S, Francis-West P H, Widelitz R B, Jiang T X, Ting-Berreth S, Tickle C, Wolpert L, Chuong C M. Local inhibitory action of BMPs and their relationships with activators in feather formation: implications for periodic patterning (1998). Dev Biol. 196(1): 11-23.

Kang M, Garg V, Hadjantonakis A K. Lineage Establishment and Progression within the Inner Cell Mass of the Mouse Blastocyst Requires FGFR1 and FGFR2 (2017). Dev Cell. 41(5): 496-510.e5.

Kim E J Y, Sorokin L, and Hiiragi T. ECM-integrin signalling instructs cellular position sensing to pattern the early mouse embryo (2022). Development (Cambridge) 149 (1): dev200140.

Kingma D P, and Ba J. Adam: A Method for Stochastic Optimization (2014). arXiv:1412.6980.

Kirschner M W. The meaning of systems biology (2005). Cell 121: 503–504.

Kirschner M, Gerhart J. Evolvability (1998). Proc Natl Acad Sci USA; 95(15): 8420-7.

Klaffky E J, Gonzáles I M, Sutherland A E. Trophoblast cells exhibit differential responses to laminin isoforms (2006). Dev Biol. 292(2): 277-289.

Klaffky E, Williams R, Yao C C, Ziober B, Kramer R, Sutherland A. Trophoblast-specific expression and function of the integrin alpha 7 subunit in the peri-implantation mouse embryo (2001). Dev Biol. 239(1): 161-75.

Kondo S, Miura T. Reaction-diffusion model as a framework for understanding biological pattern formation (2010). Science. 329(5999): 1616-20.

Lenne P-F et al. Roadmap for the multiscale coupling of biochemical and mechanical signals during development (2021). Phys. Biol. 18, 041501.

Kromm D, Thumberger T, Wittbrodt J. An eye on light-sheet microscopy (2016). Methods Cell Biol. 133:105-23.

Krzic U, Gunther S, Saunders T E, Streichan S J, and Hufnagel L. Multiview light-sheet microscope for rapid in toto imaging (2012). Nature Methods 9, 730–733.

Kurowski A, Molotkov A, Soriano P. FGFR1 regulates trophectoderm development and facilitates blastocyst implantation (2019). Dev Biol. 446(1): 94-101.

Landge A N, Jordan B M, Diego X and Müller P. Pattern formation mechanisms of self-organizing reaction-diffusion systems (2020). Dev. Biol. 460(1): 2-11.

Larue L and Bellacosa A. Epithelial-mesenchymal transition in development and cancer: Role of phosphatidylinositol 3′ kinase/AKT pathways (2005). Oncogene 24, 7443–7454.

Latos, PA., Sienerth, AR., Murray, A., Senner, CE., Muto, M., Ikawa, M., Oxley, D., Burge, S., Cox, BJ., Hemberger, M. (2015). Elf5-centered transcription factor hub controls trophoblast stem cell self-renewal and differentiation through stoichiometry-sensitive shifts in target gene networks. Genes Dev. 29(23): 2435-48.

Lecuit T and le Goff L. Orchestrating size and shape during morphogenesis (2007). Nature 450, 189–192.

Lee K Y, Jeong J W, Wang J, Ma L, Martin J F, Tsai S Y, Lydon J P, DeMayo F J. Bmp2 is critical for the murine uterine decidual response (2007). Mol Cell Biol. 27(15): 5468-78.

Lee K, Jeong J, Kwak I, Yu C T, Lanske B, Soegiarto D W, Toftgard R, Tsai M J, Tsai S, Lydon J P, DeMayo F J. Indian hedgehog is a major mediator of progesterone signaling in the mouse uterus (2006). Nat Genet. 38(10): 1204-9.

Lewandoski M, Montzka Wassarman K, and Martin G R. Zp3-cre, a transgenic mouse line for the activation or inactivation of loxP-flanked target genes specifically in the female germ line (1997). Current Biology 7, 148–151.

Li Y, Sun X, Dey SK. Entosis allows timely elimination of the luminal epithelial barrier for embryo implantation (2015). Cell Rep. 11(3): 358-65.

Luciano M, Xue SL, De Vos W H, et al. Cell monolayers sense curvature by exploiting active mechanics and nuclear mechanoadaptation (2021). Nat. Phys. 17: 1382–1390.

Loulier K., et al. Multiplex cell and lineage tracking with combinatorial labels (2014). Neuron. 81(3): 505-20.

Lynch V J et al. Ancient transposable elements transformed the uterine regulatory landscape and transcriptome during the evolution of mammalian pregnancy (2015). Cell Rep. 10: 551–561.

Lutolf M P and Hubbell J A. Synthetic biomaterials as instructive extracellular microenvironments for morphogenesis in tissue engineering (2005). Nature Biotechnology 23, 47–55.

Maddox-Hyttel P, Alexopoulos N I, Vajta G, Lewis I, Rogers P, Cann L, Callesen H, Tveden-Nyborg P, Trounson A. Immunohistochemical and ultrastructural characterization of the initial post-hatching development of bovine embryos (2003). Reproduction, 125:607–623.

Mcdole K and Zheng Y. Generation and live imaging of an endogenous Cdx2 reporter mouse line (2012). Genesis 50, 775–782.

McDole K, Guignard L, Amat F, Berger A, Malandain G, Royer L A, Turaga S C, Branson K, and Keller P J. In Toto Imaging and Reconstruction of Post-Implantation Mouse Development at the Single-Cell Level (2018). Cell 175, 859-876.e33.

Migeotte I, Omelchenko T, Hall A, and Anderson K. Rac1-dependent collective cell migration is required for specification of the anterior-posterior body axis of the mouse (2010). PLoS Biology 8, 37–38.

Migeotte I, Grego-Bessa J, and Anderson K. Rac1 mediates morphogenetic responses to intercellular signals in the gastrulating mouse embryo (2011). Development 138, 3011–3020.

Mossman, H. A. ‘‘Vertebrate Fetal Membranes.’’ (1987). Rutgers University Press, NewBrunswick, NJ.

Mossman H. Comparative Morphogenesis of the Fetal Membranes and Accessory Uterine Structures (1937). Carnegie Institution of Washington, vol. 26.

Mullins D. Symmetry breaking in biology (2009). Cold Spring Harb Perspect Biol 2: a003392.

Müller P, Rogers K W, Jordan B M, et al. Differential diffusivity of Nodal and Lefty underlies a reaction-diffusion patterning system (2012). Science. 336(6082): 721-724.

Münster S, Jain A, Mietke A, Pavlopoulos A, Grill S W, and Tomancak P. Attachment of the blastoderm to the vitelline envelope affects gastrulation of insects (2019). Nature 568, 395–399.

Muzumdar M D, Tasic B, Miyamichi K, Li N, and Luo L. A global double-fluorescent cre reporter mouse (2007). Genesis 45, 593–605.

Nagy A, Gertsenstein M, Vintersten K, and Behringer R. Manipulating the Mouse Embryo: A Laboratory Manual (2003). Cold Spring Harbor (New York): Cold Spring
Harbor Laboratory Press.

Nakamura T, Mine N, Nakaguchi E, Mochizuki A, Yamamoto M, Yashiro K, Meno C, Hamada H. Generation of robust left-right asymmetry in the mouse embryo requires a self-enhancement and lateral-inhibition system (2006). Dev Cell. 11(4): 495-504.

Nakamasu A, Takahashi G, Kanbe A, Kondo S. Interactions between zebrafish pigment cells responsible for the generation of Turing patterns (2009). Proc Natl Acad Sci USA. 106(21): 8429-34.

Niakan K K, Han J, Pedersen R A, Simon C, Pera R A. Human pre-implantation embryo development (2012). Development. 139(5): 829-41.

Nikolaev M, Mitrofanova O, Broguiere N, Geraldo S, Dutta D, Tabata Y, Elci B, Brandenberg N, Kolotuev I, Gjorevski N, et al. Homeostatic mini-intestines through scaffold-guided organoid morphogenesis (2020). Nature 585, 574–578.

Nishioka N, Inoue K, Adachi K, Kiyonari H, et al. The Hippo signaling pathway components Lats and Yap pattern Tead4 activity to distinguish mouse trophectoderm from inner cell mass (2009). Dev Cell. 16(3): 398-410.

Niwa H, Toyooka Y, Shimosato D, Strumpf D, Takahashi K, Yagi R, Rossant J. Interaction between Oct3/4 and Cdx2 determines trophectoderm differentiation (2005). Cell. 123(5): 917-29.

Nowotschin S, Setty M, Kuo Y Y, et al. The emergent landscape of the mouse gut endoderm at single-cell resolution (2019). Nature. 569(7756): 361-367.

Ohnishi Y, Huber W, Tsumura A, Kang M, Xenopoulos P, Kurimoto K, Oleś AK, Araúzo-Bravo M J, Saitou M, Hadjantonakis A K, Hiiragi T. Cell-to-cell expression variability followed by signal reinforcement progressively segregates early mouse lineages (2014). Nat Cell Biol. 16(1): 27-37.

Okada H, Tsuzuki T, Murata H. Decidualization of the human endometrium (2018). Reprod Med Biol. 17(3): 220-227.

O'Keefe F R, Chiappe L M. Viviparity and K-selected life history in a Mesozoic marine plesiosaur (Reptilia, Sauropterygia) (2011). Science. 333(6044): 870-3.

O'Rahilly R, Müller F. Developmental stages in human embryos: revised and new measurements (2010). Cells Tissues Organs; 192(2): 73-84

Palmquist K H, Tiemann S F, Ezzeddine F L, Yang S, Pfeifer C R, Erzberger A, Rodrigues A R, Shyer A E. Reciprocal cell-ECM dynamics generate supracellular fluidity underlying spontaneous follicle patterning (2022). Cell. 185(11): 1960-1973.e11.

Paszke A, Gross S, Massa F, Lerer A, Bradbury J, Chanan G, Killeen T, Lin Z, Gimelshein N, Antiga L, et al. PyTorch: An Imperative Style, High-Performance Deep Learning Library (2019). arXiv: 1912.01703.

Pineiro G, Ferigolob J, Meneghelc N, Laurin M. The oldest known amniotic embryos suggest viviparity in mesosaurs (2012). Hist Biol 2012: 1–11.

Poirier F, Timmons P M, Chan C T, Guénet J L, Rigby P W. Expression of the L14 lectin during mouse embryogenesis suggests multiple roles during pre- and post-implantation development (1992). Development. 115(1): 143-55.

Posfai E, Petropoulos S, de Barros F R O, Schell JP, Jurisica I, Sandberg R, Lanner F, Rossant J. Position- and Hippo signaling-dependent plasticity during lineage segregation in the early mouse embryo (2017). Elife. 6:e22906.

Power R M, Huisken J. A guide to light-sheet fluorescence microscopy for multiscale imaging (2017). Nat Methods; 14(4):3 60-373.

Przybyla L, Lakins J N, Weaver V M. Tissue Mechanics Orchestrate Wnt-Dependent Human Embryonic Stem Cell Differentiation (2016). Cell Stem Cell. 19(4): 462-475.

Qazi T H, Blatchley M R, Davidson M D, Yavitt F M, Cooke M E, Anseth K S, and Burdick J A. Programming hydrogels to probe spatiotemporal cell biology (2022). Cell Stem Cell. 2022; 29(5): 678-691.

Raab, G. et al. Mouse preimplantation blastocysts adhere to cells expressing the

transmembrane form of heparin-binding EGF-like growth factor (1996). Development 122, 637–645.

Rassoulzadegan M, Rosen B S, Gillot I, Cuzin F. Phagocytosis reveals a reversible differentiated state early in the development of the mouse embryo (2000). EMBO J. 19(13): 3295-3303.

Rezakhani S, Gjorevski N, and Lutolf M P. Low-Defect Thiol-Michael Addition Hydrogels as Matrigel Substitutes for Epithelial Organoid Derivation (2020). Advanced Functional Materials, 30.

Riedl J, Flynn K C, Raducanu A, Gärtner F, Beck G, Bösl M, Bradke F, Massberg S, Aszodi A, Sixt M, et al. Lifeact mice for studying F-actin dynamics (2010). Nature Methods 7, 168–169.

Rodriguez T A, Srinivas S, Clements M P, Smith J C, and Beddington R S P. Induction and migration of the anterior visceral endoderm is regulated by the extra-embryonic ectoderm (2005). Development 132, 2513–2520.

Rompolas P, Mesa K R, and Greco V. Spatial organization within a niche as a determinant of stem-cell fate (2013). Nature 502, 513–518.

Rossant J, Tam P P L. Early human embryonic development: Blastocyst formation to gastrulation (2022). Dev Cell. 57(2): 152-165.

Royal Collection Trust: https://www.rct.uk/collection/919102/the-fetus-in-the-womb-sketches-and-notes-on-reproduction

Salamat M, Miosge N, Herken R. Development of Reichert's membrane in the early mouse embryo (1995). Anat Embryol (Berl). 192(3): 275-81.

Saykali B, Mathiah N, Nahaboo W, Racu M-L, Hammou L, Defrance M, and Migeotte I. Distinct mesoderm migration phenotypes in extra-embryonic and embryonic regions of the early mouse embryo (2019). Elife. 8: e42434.

Schindelin J, Arganda-Carreras I, Frise E, Kaynig V, Longair M, Pietzsch T, Preibisch S, Rueden C, Saalfeld S, Schmid B, et al. Fiji: An open-source platform for biological-image analysis (2012). Nature Methods 9, 676–682.

Seliktar D. Designing cell-compatible hydrogels for biomedical applications (2012). Science 336 (6085): 1124-8.

Selwood L. Mechanisms underlying the development of pattern in marsupial embryos (1992). Curr Top Dev Biol. 27:175–233.

Shemetov AA, Oliinyk OS, Verkhusha VV. How to Increase Brightness of Near-Infrared Fluorescent Proteins in Mammalian Cells (2017). Cell Chem Biol. 24: 758-766.e3.

Shinar G, and Feinberg M. Structural sources of robustness in biochemical reaction networks (2010). Science 327: 1389.

Shyer A E, Huycke T R, Lee C, Mahadevan L and Tabin C J. Bending gradients: how the intestinal stem cell gets its home (2015). Cell. 161 569–80.

Sick S, Reinker S, Timmer J, Schlake T. WNT and DKK determine hair follicle spacing through a reaction-diffusion mechanism (2006). Science. 314(5804): 1447-50.

Song H, Lim H, Das S K, Paria B C, Dey S K. Dysregulation of EGF family of growth factors and COX-2 in the uterus during the preattachment and attachment reactions of the blastocyst with the luminal epithelium correlates with implantation failure in LIF-deficient mice (2000). Mol Endocrinol. 14(8): 1147-61.

Spencer T E, Hayashi K, Hu J, Carpenter K D. Comparative developmental biology of the mammalian uterus (2005). Curr Top Dev Biol. 68: 85-122.

Stassen OMJA, Ristori T, Sahlgren C M. Notch in mechanotransduction - from molecular mechanosensitivity to tissue mechanostasis (2020). J Cell Sci. 133(24): jcs250738.

Stern C. Gastrulation: From Cells to Embryo (2004). Cold Spring Harbor Laboratory Press.

Stewart C L, Kaspar P, Brunet L J, Bhatt H, Gadi I, Köntgen F, Abbondanzo S J. Blastocyst implantation depends on maternal expression of leukaemia inhibitory factor (1992). Nature. 359(6390): 76-9.

Strnad P, Gunther S, Reichmann J, Krzic U, Balazs B, de Medeiros G, Norlin N, Hiiragi T, Hufnagel L, and Ellenberg J (2016). Inverted light-sheet microscope for imaging mouse pre-implantation development. Nature Methods 13, 139–142.

Strumpf D, Mao C A, Yamanaka Y, Ralston A, Chawengsaksophak K, Beck F, Rossant J. Cdx2 is required for correct cell fate specification and differentiation of trophectoderm in the mouse blastocyst (2005). Development. 132(9): 2093-102.

Sugihara K, Nakatsuji N, Nakamura K, Nakao K, Hashimoto R, Otani H, Sakagami H, Kondo H, Nozawa S, Aiba A, et al. Rac1 is required for the formation of three germ layers during gastrulation (1998). Oncogene. 17(26): 3427-33.

Sutherland A E, Calarco P G, Damsky C H. Developmental regulation of integrin expression at the time of implantation in the mouse embryo (1993). Development 119, 1175–1186.

Sutherland A. Mechanisms of implantation in the mouse: Differentiation and functional importance of trophoblast giant cell behavior (2003). Developmental Biology 258, 241–251.

Suzuki D, Okura K, Nagakura S, Ogawa H. CDX2 downregulation in mouse mural trophectoderm during peri-implantation is heteronomous, dependent on the YAP-TEAD pathway and controlled by estrogen-induced factors (2022). Reprod Med Biol. 21(1): e12446.

Tischer C, Ravindran A, Reither S, Chiaruttini N, Pepperkok R, and Norlin N. BigDataProcessor2: a free and open-source Fiji plugin for inspection and processing of TB sized image data (2021). Bioinformatics 37, 3079–3081.

Turco M Y, Gardner L, Hughes J, Cindrova-Davies T, Gomez M J, Farrell L, Hollinshead M, Marsh S G E, Brosens J J, Critchley H O, et al. Long-term, hormone-responsive organoid cultures of human endometrium in a chemically defined medium (2017). Nature Cell Biology 19, 568–577.

Turner W. Lectures on the comparative anatomy of the placenta. Edinburgh: Adam and Charles Black; 1876.

van den Brink S C, Baillie-Johnson P, Balayo T, Hadjantonakis AK, Nowotschin S, Turner DA, Martinez Arias A. Symmetry breaking, germ layer specification and axial organisation in aggregates of mouse embryonic stem cells (2014). Development. 141(22): 4231-42.

Vianello S and Lutolf M P. Understanding the Mechanobiology of Early Mammalian Development through Bioengineered Models (2019). Developmental Cell 48, 751–763.

Vladar E K, Antic D, Axelrod J D. Planar cell polarity signaling: the developing cell's compass (2009). *Cold Spring Harb Perspect Biol*. 1(3): a002964.

Wagner G P, Kin K, Muglia L, Pavlicev M. Evolution of mammalian pregnancy and the origin of the decidual stromal cell (2014). Int J Dev Biol. 58(2-4): 117-26.

Warner S M, Conlon F V, Kane M T. Inositol transport in preimplantation rabbit embryos: effects of embryo stage, sodium, osmolality and metabolic inhibitors (2003). Reproduction. 125(4): 479-93.

Walmsley M J, Ooi S K, Reynolds L F, Smith S H, Ruf S, Mathiot A, Vanes L, Williams D A, Cancro M P, Tybulewicz V L. Critical roles for Rac1 and Rac2 GTPases in B cell development and signaling (2003). Science, 302(5644): 459-62

Wang Y and Riechmann V. The Role of the Actomyosin Cytoskeleton in Coordination of Tissue Growth during Drosophila Oogenesis (2007). Current Biology 17, 1349–1355.

Wewer U M, Damjanov A, Weiss J, Liotta L A, and Damjanov I. Mouse endometrial stromal cells produce basement-membrane components (1986). Differentiation 32, 49–58.

Whitten M K. Effect of Exteroceptive Factors on the Œstrous Cycle of Mice (1957). Nature 180, 1436.

Whitacre J M, Bender A. Networked buffering: a basic mechanism for distributed robustness in complex adaptive systems (2010). Theor Biol Med Model. 7:20.

Wolf S, Bailoni A, Pape C, Rahaman N, Kreshuk A, Köthe U, and Hamprecht F A. The Mutex Watershed and its Objective: Efficient, Parameter-Free Graph Partitioning (2019). arXiv: 1904.12654v2.

Wolny A, Cerrone L, Vijayan A, Tofanelli R, Barro A V, Louveaux M, Wenzl C, Strauss S, Wilson-Sánchez D, Lymbouridou R, et al. Accurate and versatile 3D segmentation of plant tissues at cellular resolution (2020). Elife 9, 1–34.

Wu J, Lewis AH, Grandl J. Touch, Tension, and Transduction - The Function and Regulation of Piezo Ion Channels (2017). Trends Biochem Sci. 42(1): 57-71.

Yanagida A, Corujo-Simon E, Revell C K, et al. Cell surface fluctuations regulate early embryonic lineage sorting (2022). Cell. 185(5): 777-793.e20.

Ye J, Coulouris G, Zaretskaya I, et al. Primer-BLAST: A tool to design target-specific primers for polymerase chain reaction (2012). BMC Bioinformatics 13, 134.

Ying Y and Zhao G Q. Detection of multiple bone morphogenetic protein messenger ribonucleic acids and their signal transducer, Smad1, during mouse decidualization (2000). Biol. Reprod. 63: 1781–1786.

Yuan J, Cha J, Deng W, Bartos A, Sun X, Ho H Y H, Borg J P, Yamaguchi T P, Yang Y, Dey S K, et al. Planar cell polarity signaling in the uterus directs appropriate positioning of the Crypt for Embryo implantation (2016). Proc Natl Acad Sci USA 113, E8079–E8088.

Zhang Y, Conti M A, Malide D, Dong F, Wang A, Shmist Y A, Liu C, Zerfas P, Daniels M P, Chan C-C, et al. Mouse models of MYH9-related disease: mutations in nonmuscle myosin II-A (2012). 119(1): 238-50.

ACKNOWLEDGEMENTS

First of all, I am thankful to all my previous mentors, colleagues, and a bit of luck for being able to work at EMBL during these four years alongside some of the most outstanding scientists. These were four years of intense research, challenges, lessons, enlightening ideas, discussions, new connections, and fun. I want to thank everyone I've met on this journey for sharing passions with me and making wonderful colleagues and friends. This study was made possible by many excellent and dedicated professionals with whom I had much fun interacting.

I want to thank Takashi Hiiragi for giving me the scientific freedom and independence to follow Laura's work and pursue my passion for embryo implantation and for his supervision and mentorship. To Lidia Perez, Stefanie Friese, and Ramona Bloehs for all their help with cloning and the mouse work. My special thanks to Steffi for her encouragement at the start of my Ph. D and believing in the Embryobow project. To Ramona for all her experiments with ESC and Wibke Schwarzer for starting the Embryobow and guiding me on the way through cloning and mouse transgenesis. To Yvonne Petersen for a great effort in making the Embryobow mouse line possible. To the rest of the group for all the scientific discussions we had and the inputs on my research: Prachiti Moghe, Dimitri Fabregas, Hui Ting Zhang, Ritsuya Niwayama, Joe Chan, Esther Kim, Takafumi Ichikawa, Allyson Ryan, Erica van der Maas.

To our fantastic interns and students who helped create a friendly atmosphere and worked on their projects with an incredible passion: Maria Costanzo, Alison Kickuth, Vera Janssen, and Adele Micouin. I want to thank my students, Falk Farkas and Nisha Veits, for their feedback on my mentorship. I feel like I learned more from them than they ever learned from me. My special thanks to L. Panavaite for supervision during the first months and for helping prepare me for a Ph.D. To Dimitri Kromm for being not only a great collaborator but also a friend and a great companion through this journey. I will forever remember that 'aha' moment when we acquired the implanting embryo time-lapse for the first time! To Mike Nikolaev for making the entire micro-crypt idea possible. My thanks to Anna Erzberger and Roman Belousov for joining this project and enriching it with biophysical modeling, which brought us a lot of new insights. To Adrian Wolny and Johannes Hugger for developing image analysis tools for this project. To Christian Tisher and Marko Lampe for their help with image processing. To the rest of the ALMF team who assisted me with the microscopes: Alex,

Sabine, Stefan, and others. I want to thank Tim Hettinger at the EMBL mechanical workshop and Christian Kieser at the electronic workshop for manufacturing pieces for our microscope. And of course, none of the experiments would have been possible without the fantastic work of mouse animal caretakers: Alessandro, George, David, Ernesto, Isabel, and many others.

I want to thank Alexander Aulehla, Detlev Arendt, Anne Ephrussi, Aissam Ikmi, Nicoletta Petridou, Steffen Lemke, and Jochen Wittbrodt for their input and advice on my research and career. My thanks to all members of the DB unit for being great colleagues and creating a stimulating and collaborative environment.

Lastly, I want to thank most to my mother, Tetiana, and my aunt, Olena, for everything that they did for me and for their endless love and support.

APPENDIX

Mouse Line	Primer ID	Primer Sequence	PCR Product Size, bp
mTmG and mG	oIMR7318	CTCTGCTGCCTCCTGGCTTCT	WT allele, 330; Knock- in allele, 250
	oIMR7319	CGAGGCGGATCACAAGCAATA	
	oIMR7320	TCAATGGGCGGGGGTCGTT	
H2B-GFP	CAG-Fw	GGCTTCTGGCGTGTGACCGGC	Tg allele, 900
	EXFP-Rv	GTCTTGTAGTTGCCGTCGTC	
Myh9-GFP	GFP-Myh9_1	CTGTCACATGGCTCATGTTC	WT allele, 400; Knock- in allele, 200
	GFP-Myh9_2	GCCGGACACGCTGAACTTGT	
	GFP-Myh9_3	GCCCTGAGTAGTATCGCTCC	
Cdx2-GFP	Cdx2-Fw	ATGGTTCCGTTCCCTGGTTC	WT allele, 1400; Knock- in allele, 750
	GFP-Rv	GCGGACTTGAAGAAGTCGTGC TGCTT	
	Cdx2-EX3	AGGCTTGTTTGGCTCGTTACAC	
Rac1-flox/del	Rac1_1	ATTTTGTGCCAAGGACAGTGAC AAGCT	WT allele, 300; Flox, 330; del 130
	Rac1_2	GAAGGAGAAGAAGCTGACTCC CATC	
	Rac1_3	CAGCCACAGGCAATGACAGAT GTTC	
Lifeact-GFP	LifeAct for 2	TCAAGAAATTCGAAAGCATCTC AAAGG	Tg allele, 725
	VenCeru-geno rev	GACCATGTGATCGCGCTTCTC GTT	
ZO1-GFP	ZO1-GFP-for	GCTTTCAGATGATTGTAGCC	Tg allele, 400
	ZO1-GFP-rev	GAACTTGTGGCCGTTTACGTCG	
	ZO1-WT-for	CTTTCAGATGATTGTAGCCAGC	WT allele, 420
	ZO1-WT-rev	CCTTCATCAGTTCCAACAAATG C	

Appendix 1. The primers used for genotyping.

Probe ID	Probe Sequence	Primer ID	Primer Sequence	PCR Product Size, bp
ddPCR	5'6FAM-ggatccgtcgccaggcagcct-BHQ1'3	ddPCR_F	gcaacgtgctggttAttgtg	239
		ddPCR_R	gatatggatcggctcatcgt	
Palmbow	5'6FAM-cgccgcaccaagcccgtgga-BHQ1'3	ddPCR_bow_F	gggaggattgggaagacaat	247
		ddPCR_Palmbow_R	aagcgcatgaactccttgat	
Mitbow	5'FAM-cccgtcgccaccggatccgc-BHQ1'3	ddPCR_Mitbow_F	gccaagatccattcgttgag	104
		ddPCR_Palmbow_R	aagcgcatgaactccttgat	
Nucbow	5'FAM-ccgccaccatgccagaaccagca-BHQ1'3	ddPCR_bow_F	gggaggattgggaagacaat	158
		ddPCR_Nucbow_R	tcttctgggctttggtaacg	
Rpp30_1	5'HEX-cggtccagcttcctcctctgcacgc-3'BHQ1	Rpp30_ddPCR_F	gtgacgaaaggagagggcaa	142
		Rpp30_ddPCR_R	aggggaatcacacaggcatg	
Rpp30_2	5'HEX-cctcccgctcctccggccct-3'BHQ1	Rpp30_ddPCR_2F	tagccatggccgtcattgtt	197
		Rpp30_ddPCR_2R	gctcacctggtccgaagaaa	
Col1a1	5'HEX-tggagaacccgctgcacaccct-3'BHQ1	Col1a1_ddPCR_F	agtgcacgtctcagtcagtg	142
		Col1a1_ddPCR_R	gtttctttgtctggccagcg	

Appendix 2. The probes and primers used for ddPCR.

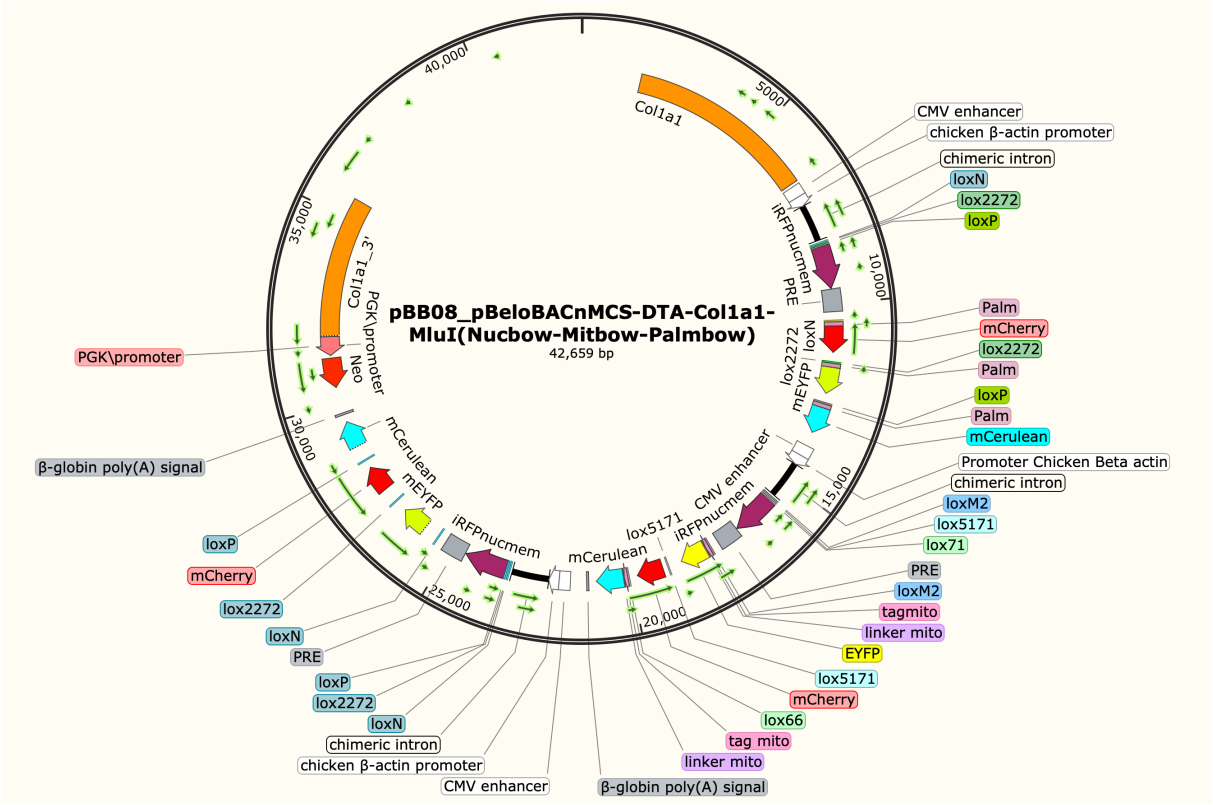

Appendix 3. The schematic of the pBB08_pBeloBACnMCS-DTA-Col1a1-MluI(Nucbow-Mitbow-Palmbow construct. Col1a1 marks homology arms, flanking the array of fluorophores (mYEFP, mCherry, mCerulean, IRFPnucmem), driven by CMV enhancer and chicken beta-actin promoter in the following order: Palmbow (Palm), Mitbow (tag mito/linker mito), Nucbow. Neomycin (Neo) is driven by the PGK promoter.

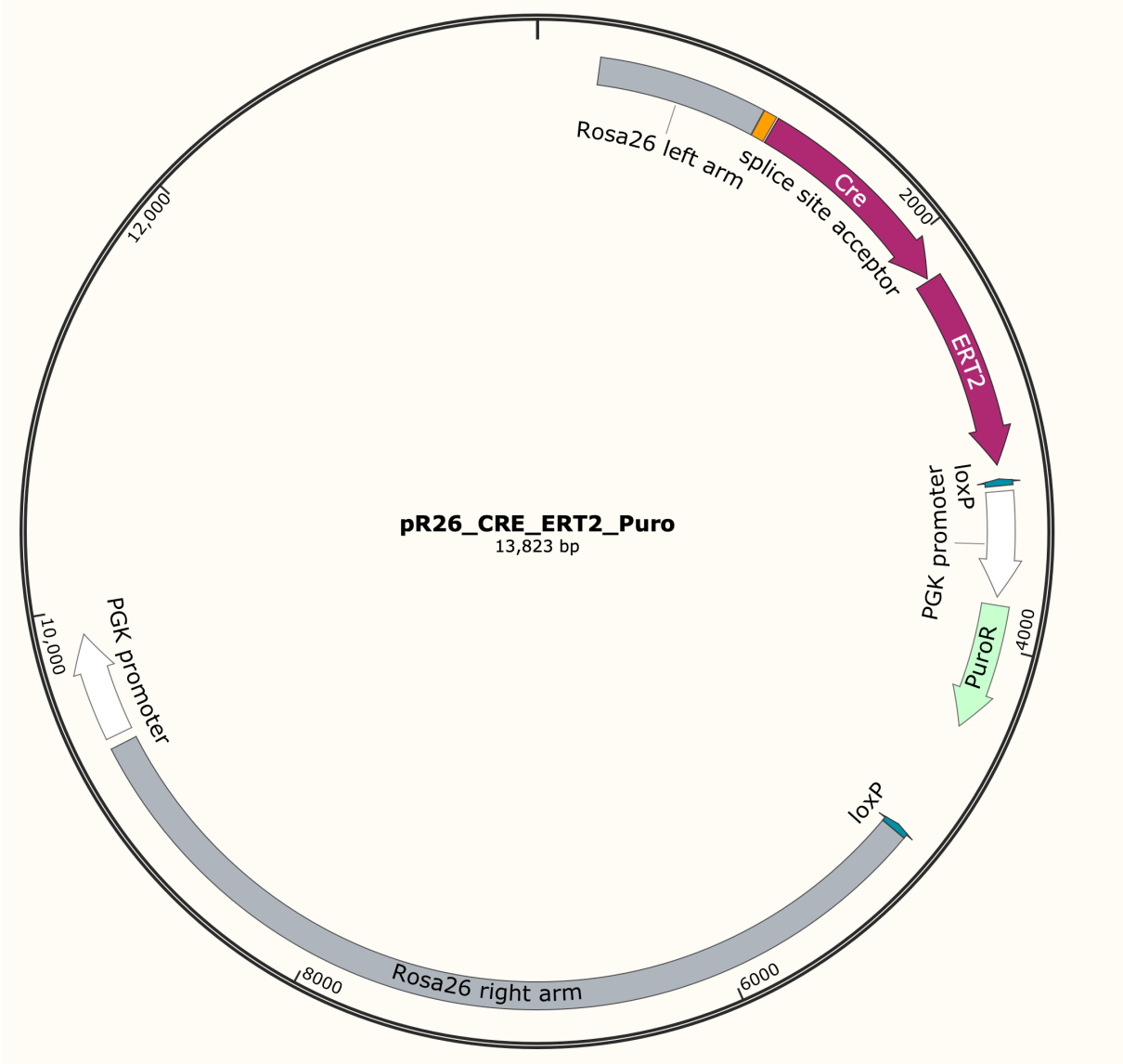

Appendix 4. The schematic of the pR26_CRE_ERT2_Puro construct. Puromycin (PuroR) expression is driven by the PGK promoter.